5-2018

Synthesis and Characterization of Model Acrylic-Based Polymer Gels

Travis Lawrence Thornell
Purdue University

SYNTHESIS AND CHARACTERIZATION OF MODEL ACRYLIC-BASED POLYMER GELS

by

Travis Lawrence Thornell

A Dissertation

Submitted to the Faculty of Purdue University

In Partial Fulfillment of the Requirements for the degree of

Doctor of Philosophy

School of Materials Engineering

West Lafayette, Indiana

May 2018

THE PURDUE UNIVERSITY GRADUATE SCHOOL
STATEMENT OF COMMITTEE APPROVAL

Dr. Kendra A. Erk, Chair
School of Materials Engineering
Dr. John A. Howarter
School of Materials Engineering
Dr. Jeffrey P. Youngblood
School of Materials Engineering
Dr. Bryan W. Boudouris
Davidson School of Chemical Engineering

Approved by:

Dr. David F. Bahr
Head of the Graduate Program

To Mom and Dad

ACKNOWLEDGMENTS

I would like to thank my advisor, Prof. Kendra Erk, for her great support and guidance throughout my graduate career. Thank you for your patience in allowing me to investigate and attempt a wide variety of projects. I would also like to acknowledge my committee of Prof. John Howarter, Prof. Jeffrey Youngblood, and Prof Bryan Boudouris for their suggestions and discussions of polymer science. This work was supported by a National Science Foundation Graduate Research Fellowship (DGE-1333468) and the Purdue University Ross Graduate Assistantship.

Thank you to my fellow group members in the Soft Material Mechanics group: Dr. Matt Krafcik, Dr. Lisa Murray, Anna Walter, Jerome Nash, Eduard Caicedo-Casso, Baishakhi Bose, and Cole Davis. I cannot imagine working with a better group while in graduate school. In the collaborative environment of the MSE department, I was surrounded by great colleagues working in soft materials. Thank you to Dr. Logan Kearney, Dr. Kai Gao, Dr. Gamini Mendis, Dr. Shane Peng, Michael Toomey, and Jessica Sargent for being great researchers and people to work alongside.

My journey to Purdue would likely not have been possible without the mentorship of Dr. Katherine Frank while at Southern Miss as I worked as an undergraduate researcher. That experience served as a blueprint for mentoring undergraduates during my graduate career. Thank you to Benjamin Helfrecht, Krithika Subramaniam, and Mayank Jain for your hard work and assistance.

I would also like to thank the friends that I have made while at Purdue: Dr. Andrew Kustas, Dr. Logan Kroneman, Derek Schwanz, Dan Klenosky, John Holaday, Kara Luitjohan, Prof. Rod Trice and all those that participated in the summer softball team. I

want to also acknowledge the many relationships that I have made while being involved at St. Thomas Aquinas Catholic Center on campus.

Lastly, I would like to thank my family and friends for their love and support. Thank you to Mom, Dad, Billy, Mandy, and Raegan for always being there no matter how far away I was.

TABLE OF CONTENTS

LIST OF TABLES

LIST OF FIGURES

ABSTRACT

Author: Thornell, Travis, L. PhD
Institution: Purdue University
Degree Received: May 2018
Title:Synthesis and Characterization of Model Acrylic-Based Polymer Gels.
Committee Chair: Kendra Erk

Materials made from polymer gel networks are important to many everyday applications in health care to building materials. These gel materials can be easily synthesized in various ways, but characterizing the overall material mechanics and properties are challenging due to the soft nature of their respective bulk structures. Model acrylic-based copolymer gels were investigated to understand the fundamental characteristics and mechanical properties from different crosslinking and gelation processes.

First, model hydrogels with fracture-healing characteristics similar to materials needed for injectable drug delivery systems were studied using shear rheology to determine timescales of fully healed networks. The industrially available gel was a thermoreversible triblock copolymer composed of poly(methyl methacrylate)-poly(n-butyl acrylate)-poly(methyl methacrylate) in 2-ethyl hexanol to form a physical gel from polymer-solvent interactions. A methodology of quantifying healing was developed from an applied constant shear rate and monitoring the shear stress response of the samples. The maximum shear stress responses observed during fracture and re-fracture after allowing the sample to rest indicated gel healing. Given sufficient time, gel healing was determined to be dependent on testing temperature and polymer volume fraction. The time for fully healed networks was achieved on the order of minutes for the lowest volume fraction of 5 vol. %

at temperatures of 28 and 25°C to several hours for the highest volume fraction of 6 vol. % at lower temperatures of 23 and 20°C.

Lastly, spherical superabsorbent polymer (SAP) gels with silica nanoparticles (SiO_2) were synthesized from inverse suspension polymerization to form chemically crosslinked composite hydrogels of polyacrylamide and poly(acrylic acid). The hydrogels were studied for understanding the interaction of SiO_2 nanoparticles within polyelectrolyte networks for use as a chemical admixture for internal curing of high performance concrete. The composite SAP hydrogels were produced with bare or silane-functionalized SiO_2 particles to investigate the effects on swelling performance, shape, and cement paste microstructure.

CHAPTER 1. INTRODUCTION

1.1 Polymer Gels

Polymer gels are a wide ranging classification of polymer materials. The gel term refers to crosslinked polymer networks swelling in a solvent.[1] Different names are given to various solvents used to swell the gels, such as hydrogels for water and organogels for organic solvents.[2] The versatility and breadth of gels have allowed them to be suitable for many different applications based on polymer and solvent combinations. Gels have become increasingly important for use as injectable drug delivery systems,[3] enhanced oil recovery,[4] personal hygiene,[5] and agricultural applications.[6]

A common monomer type used in polymer gels are acrylate-based monomers, which are able to undergo addition polymerizations easily. The carbon-carbon double bond on the monomers allow for facile reaction with a propagating species. Figure 1-1 illustrates the acrylic-based monomers that constitute the various polymer gels studied. The first polymer gel system is composed of a commercially available A-B-A triblock copolymer of methyl methacrylate endblocks connected by n-butyl acrylate. This copolymer can be produced via anionic polymerization[7,8] and atom-transfer radical polymerization.[9] The second gel system investigated was synthesized from acrylamide (AM) and copolymerization with acrylic acid (AA) with silica nanoparticles to form composite hydrogels. Copolymerization and gelation of AM and AA can be achieved through inverse suspension polymerization[10,11] and free radical polymerization.[12]

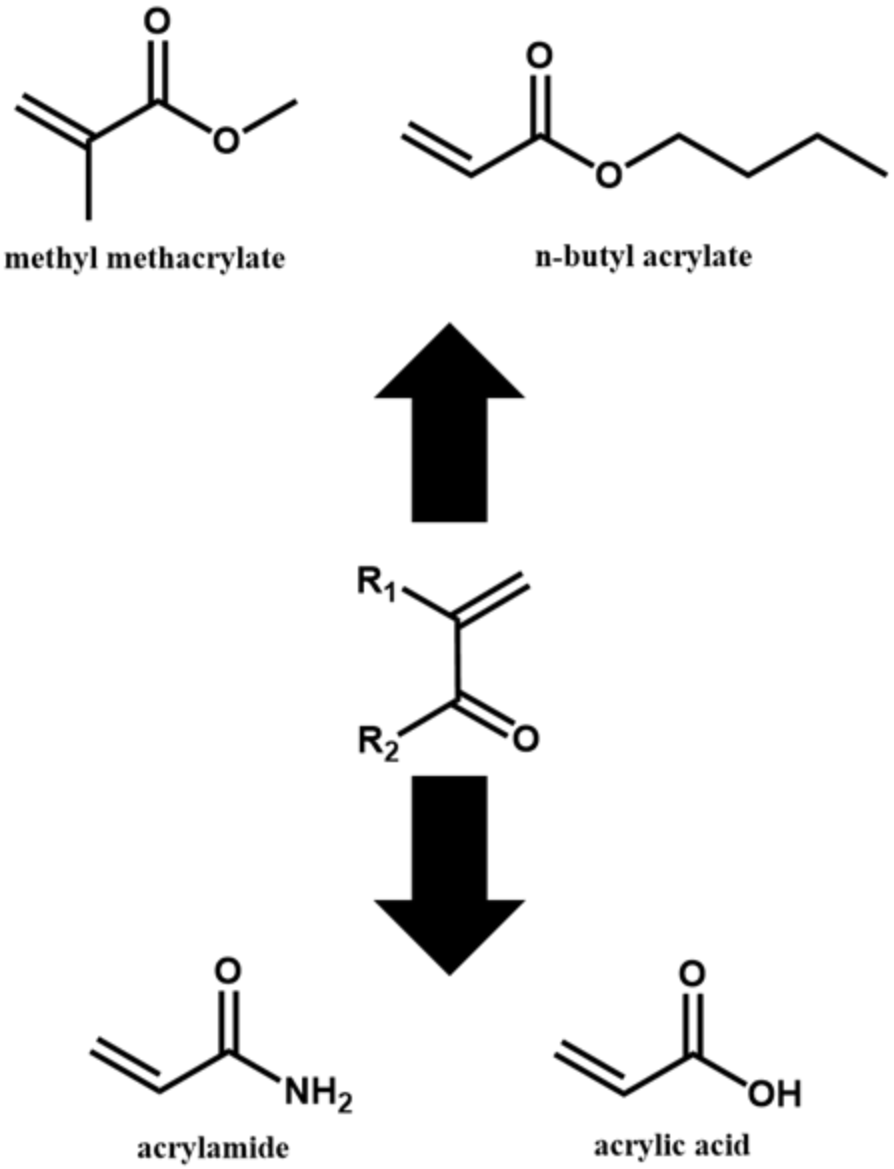

Figure 1-1 Acrylic-based monomers used in this work.

1.2 Types of Gels

There are many ways in which polymer network crosslinks form to create gels. These methods are categorized by the nature of the crosslinking which can be physical or chemical. Physical crosslinks are those from which an external stimuli or interaction that drives gelling. Conversely, chemical crosslinks are covalent crosslinks that permanently

bind the network. These different gel network methodologies allow for various properties to be obtained.

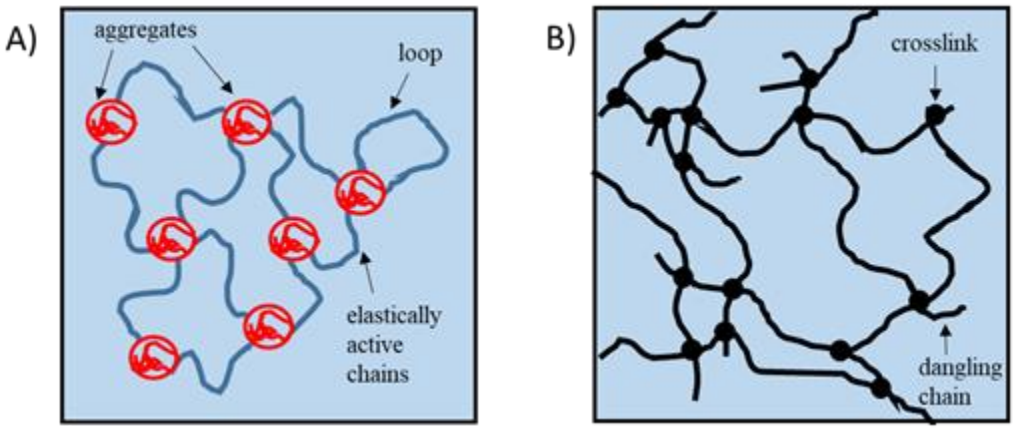

Figure 1-2 Schematic of different polymer gel networks of A) physical gelation and B) chemical gelation

1.2.1 Physical Gelation

Physical polymer gels can be created by external stimuli or interactions between polymer chains to form a network from noncovalent bonding. Hydrogen bonding, van der Waals forces, and ionic associations produce the generally weak physical bonding.[1] The resulting bonds and network interactions can be reversible and dynamic since the bonding can be easily broken and reformed. The response to applied stimuli, polymer type, and solvent amount dictate the strength of the network. Temperature, pH, and electrostatic interactions are common stimuli that produce physical gels and hydrogels.

For thermoreversible gels, such as block copolymers studied in this work, heating above a critical temperature causes the physical bonding to dissolve and become a polymer solution. The thermoreversible character is derived from the polymer-solvent interactions that arise from each block having different solubility conditions for the solvent. The blocks that have unfavorable mixing will self-assemble into aggregates that serve as the physical

crosslinking junctions. Blocks that are soluble connect each of the aggregates to produce a connected gel network.

As illustrated in Figure 1-2A, physically associating gels networks consist of chain aggregates that are connected by elastically active chains. These chains bridge connecting aggregates and allow for applied stress or deformation to be transmitted across the network.[13] Loops can form where a chain strand has both endblocks enter into the same aggregate.[14] Dangling chains can also be present where only one end of a polymer chain or stand is connected to a network aggregate and the other end is free, or dangling. These defects are not able to give any strength or carry any stress in the network.

1.2.2 Chemical Gelation

Chemical gels are synthesized from covalent crosslinking of polymer chains. Since the crosslinks are chemically attached to the chains, the resulting gels are stronger and the networks are irreversible and permanent.[1] Gelation of polymers can be achieved in many ways through condensation or addition polymerization. For condensation polymerization, one of the monomers will need a higher level of functionality to form crosslinks. For example, bifunctional monomer of A-A reacting with monomer functionality of B-B will yield a linear polymer, but substituting a monomer with more functionality, such as B_3, will create branching points and chemical crosslinks to form a network.[15]

For addition polymerization, the use of monomers or crosslinking agents with multiple double bonds will facilitate gelation. A common crosslinking agents is N,N-methylenebisacrylamide (MBAM). MBAM is an acrylic-based molecule that has a similar structure to acrylamide and readily polymerizes with acrylamide and acrylic acid to form hydrogel networks. [10–12]

A random crosslinked chemical gel is shown in Figure 1-2B. Crosslinked sites are present throughout the networks and are randomly distributed. Dangling chain ends will also be created from unreacted functional groups and incomplete propagation.[16] The dangling chain ends will lower the crosslinking density and change the rate of polymerization of the resulting gel.[17]

1.3 Polymer Gel Mechanical Properties and Challenges

The mechanical properties of polymer gels are dependent on the crosslinking type with physical gels producing weak gels and chemical crosslinked gels yielding stronger gels.[1] Standard mechanical testing, such as tensile and compression testing, can be used to study modulus and network structure. The application of the statistical theory of rubbery elasticity[18] allows for the relationship between shear modulus and the molecular weights between crosslinks to be calculated as seen in Equation 1.1,

$$G=kT\frac{\upsilon_e}{V}=\frac{\rho RT}{M_x}, \tag{1.1}$$

Where G is the shear modulus, k is Boltzmann constant, T is temperature, υ_e is the total number of elastically effective stands, V is the total volume, ρ is the network density, R is the gas constant, and M_x is the molecular weight between the crosslinks.

For weak gels, the challenges of measuring gel properties can be attributed to the soft nature and the non-uniformity of crosslinking points. The large amount of solvent trapped in hydrogels ($\geq$ 90 % volume is water) make samples not easily self-supporting and difficult to load into equipment. Given the difficulty in measuring weak gels with this method, alternative methods are needed.

1.3.1 Use of Rheometry to Study Gel Properties

To overcome the challenges of measuring mechanical properties of weak gels, shear rheometry can be utilized to investigate gel deformation and mechanical properties. The various geometries available, such as concentric cylinders (Couette geometry), allow for the gels to be loaded into the rheometer without issues of stabilizing the sample in the grips or casting into a mold. With the gel residing in a cup in contact with the instrument's fixture, a shear can be applied and the resulting stress response can be measured as a function of strain. Some gels exhibit a shear thinning behavior of fracture after deformation, but are capable of fully recovering their mechanical properties in a process known as self-healing.

The area of self-healing injectable hydrogels has been gaining popularity in research for use in controlled drug delivery,[3,19] cell therapy,[20,21] and tissue engineering.[22] These gels shear-thin or fracture after deformation, but can fully heal and allow for the delivery of the contents of the gel without any issues or loss efficacy. The shear applied from the rheometer is able to simulate the environment of the deformation the gel experiences when injected through a syringe. The mechanical properties of the gel are characterized to determine its ability to survive deformation without harming its ability to deliver therapeutic agents.

The viscoelasticity and shear stress response of gels can be characterized using rheology, but the timescales and kinetics of network healing are difficult to measure. Approaches to determining the healing of gel networks have centered around monitoring the recovery of the storage modulus (G') over time. The values of G' describe the sample's solid-like character, while G'', the loss modulus, indicates the liquid-like response of the gel. In these experiments, a small oscillation is applied and G' is measured as a function of

time until it reaches the original value before deformation. This approach is able to capture the recovery of shear-thinning materials as the time scales are near those of the initial gelling kinetics. For gels that exhibit fracture-like behavior from a shear stress overshoot, a methodology focused on monitoring the shear stress response should be implemented since that would give more direct insights on network strength.

1.3.1.1 Flow Visualization in Polymer Gels

To understand the gel deformation completely, rheology data alone is not sufficient to determine fracture events from other flow instabilities. By correlating rheophysical flow visualization techniques to rheology data, the evidence of flow instabilities can be obtained. Various techniques, such as magnetic resonance,[23] ultrasound speckle velocimetry,[24] and particle image velocimetry/particle tracking velocimetry (PIV/PTV),[25] have been coupled with rheometry to determine flow characteristics.

Figure 1-3 illustrates common flow instabilities and the resulting velocity profiles for polymer solutions and gels. The velocity profiles are collected from a relative velocity across the experimental gap calculated from the velocity of the flow (V) to the applied velocity of the fixture (V_{fix}). For uniform ideal shear, a single velocity gradient from the moving wall to the stationary wall is present. The velocity profile for uniform shear or Newtonian flow has a velocity of zero at the stationary wall and increases to the moving wall. The slope of this velocity profile signifies the applied shear rate. A phenomena known as shear banding occurs when the flow appears to have multiple shear rates through the system across the experimental gap in the velocity profile. When the velocity at the stationary wall has a non-zero origin, wall slip is disrupting the ability to capture the material's deformation behavior. Fracture behavior can be determined by the clear regions

of the material moving with the applied velocity of the fixture and corresponding regions having no velocity. The area between the two regions is called the fracture plane.

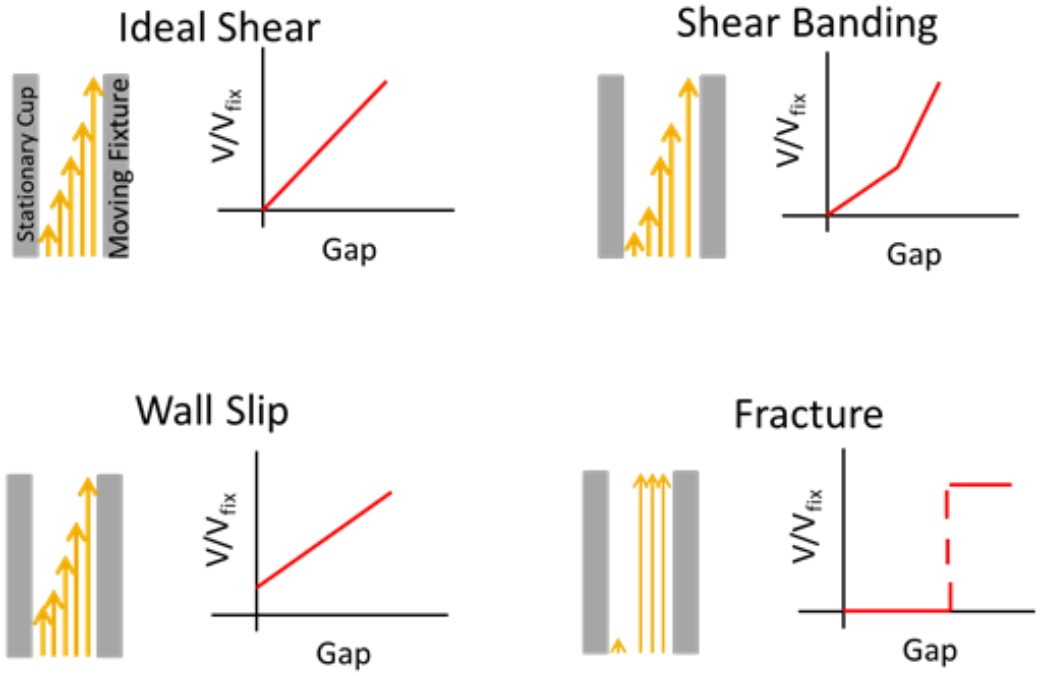

Figure 1-3 Velocity profiles of common flow and flow instabilities

Rheometry coupled with particle image velocimetry (Rheo-PIV) allows for the visualization of the flow behavior of polymers by image processing of particles embedded in a sample. PIV has been used to study flow of particles in wind tunnels[26] to complex flows in microfluidics.[27] For Rheo-PIV, particles are added to the gel to be illuminated by a laser or visible light for tracking of the flow. The matching of particles to the solvent needs to be considered to avoid settling or buoyancy issues and that the addition of the particles does not alter the flow behavior.[28] A single, directed light sheet is used to probe a single plane across the gap, so particles that sediment or float can introduce large errors from moving in and out of that specific plane. Images are obtained simultaneously during rheology and then processed through cross-correlation algorithms. Images are processed in

pairs and regions of interests are interrogated by comparing the illuminated particles positions in pixels between each image. By setting the boundary conditions of the moving and stationary walls, the particle positions and velocities can be accurately determined and are easily related back to the rheology of the system to confirm flow instabilities.

1.3.2 Swelling Behavior of Polymer Gels

For many applications such as diapers, contact lenses, and biological tissue replacement, the hydrogels affinity to swell is a key characteristic. The three dimensional crosslinked network can swell many times the original size. The swelling response is a balance between the osmotic pressure differences between the gel and the solvent. The hydrophilic polymer chains are anchored to one another by chemical crosslinks that can vary in strength and crosslink density.

The swelling behavior can be studied by relating the mass of a dry gel sample to a swollen sample. Equation 1.2 can be used to quantify the swelling ratio (Q) of hydrogels

$$Q = \frac{m_{swollen} - m_{dry}}{m_{dry}} \tag{1.2}$$

where $m_{swollen}$ is the mass of the swollen sample and m_{dry} is the mass of the initial dry sample. Many different techniques are available to measure swelling. For gels that are able to be casted into molds, the molds can be submerged in aqueous solutions and then measured on a scale.[29,30] For gels that are dried powders, a gravimetric approach using tea-bags is more appropriate to accurately measure the gels.[31,32] Measurement intervals of swelling are able to give insights into swelling kinetics and time needed to reach equilibrium swelling.

For polyelectrolyte networks, the swelling capacity can be increased to large quantities by the amount of ionic side chains in the gel. These ionic side chains exhibit an electrostatic response that results in repulsion of the side chain groups. For example, poly (acrylic acid) side chains of carboxylic acid (-COOH) can deprotonate at low pH values to become $-COO^-$.[30,33] The negative side chains will now repel one another and increase the swelling response due to the higher osmotic pressure present within the gel.

The presence of monovalent (1:1) and divalent (2:1) salts can change the response of polyelectrolyte network swelling. As studied by Horkay and co-workers using theory, swelling experiments, and scattering methods,[12,34,35] the addition of 1:1 salts (i.e., NaCl) and 2:1 salts ($CaCl_2$) were able to decrease the swelling response of hydrogels from the behavior seen in deionized water. Monovalent salts were able to reduce swelling by decreasing osmotic pressure, but divalent salts have a more pronounced effect on swelling by charge screening and decreasing the electrostatic repulsion of neighboring chains.

1.4 Polymer Chemical Admixtures for Internal Curing of Concrete

Alongside biological and personal hygiene applications, super absorbent polymer (SAP) hydrogels have been used in structural material applications, such as high-performance concrete (HPC). HPC differs from conventional concrete with respect to the amount of water added to Portland cement during mixing. This is known as the water-to-cement ratio (w/c). For conventional ordinary concrete, the w/c needed is ≥ 0.42 to allow for enough water to hydrate the Portland cement for curing.[36] For HPC materials, the w/c ratio is reduced to ~0.35 to create a denser microstructure and increase durability.[37] The decreased amount of water available for the curing reaction of Portland cement to produce calcium hydroxide ($Ca(OH)_2$ "CH") and calcium silicate hydrate ($CaOSiO_2 \cdot H_2O$ "CSH

gel") can cause autogenous shrinkage and self-desiccation resulting in cracking and poor mechanical properties. Autogenous shrinkage refers to the macroscopic volume reduction of the material from the shortage of water available.[38] This shrinkage then causes self-desiccation, the decrease in relative humidity within the material.[39] Conventional external curing methods after setting and placement, such as supplying more water or using a covering to avoid evaporation on the surface, are not able to reach the bulk of the concrete. This isdue to the limited diffusion and permeability as the exposed surface solidifies first.[40]

To solve these issues, the use of internal curing admixtures was developed to reduce autogenous shrinkage. Industrial by-products and low cost alternatives such as rice husk,[41] fly ash,[40] and light weight aggregate[39,42] have been implemented as materials to distribute more water in the curing process to avoid drying out. These porous materials absorb water and as the free water is consumed, the trapped water is removed and made available for curing to proceed. These approaches do decrease the autogenous shrinkage, but require large quantities and long presoaking times of up to 24 hours to saturate.[39]

SAP hydrogels do not require any pre-soaking and only 0.2 wt.% by mass of cement is needed for positive effects in the concrete to be observed.[38] SAPs have a large swelling capacity and can be fine-tuned based on composition.[43] SAPs are ideal materials for internal curing as they can absorb water and then de-swell providing the needed water for hydrating of cement to continue. The compositions of SAP are primarily composed of water soluble monomers of acrylic acid (AA) and acrylamide (AM) crosslinked into a chemical gel. The side chain forms of AA (COOH or $COO^{-}Na^{+}$) are able to complex with the various ions present in Portland cement. Commercially available SAPs have been used throughout literature for internal curing and self-sealing concretes but the proportions of

AA to AM are not known.[44–46] Previous research in the Erk group has investigated effects varying the ratio of AA-AM and the shape of SAP particles.[43,47–49]

In addition to internal curing admixtures being used to decrease autogenous shrinkage, they can be added to help create more hydrated product. These materials are called pozzolans and are able to react with $Ca(OH)_2$ to form silicate compounds, such as CSH. These reactions are beneficial in the curing reaction since they produce more quantities of hydrated product that would be not be possible otherwise and create a more durable concrete. The most common pozzolanic material is silica fume with large amounts of silica (SiO_2) content produced from industrial metallurgy processes.[50] The size of silica fume particles in use are usually below 1μm as specified by supplier[51] but large levels of agglomeration is typically present (100's μm).[52]

It is hypothesized that a model system could be synthesized using SAP incorporated with SiO_2 nanoparticles to serve the dual purposes of internal curing as well as impart pozzolanic properties. Polymer-silica gels have been readily studied in literature for a variety of applications from additives for paper making processes[53] to heavy metal ion removal from wastewater,[54] but have not been readily applied to concrete and structural applications.

1.5 Project Scope

This dissertation aims to study different types of polymer gels produced from acrylic-based monomers and the challenges of characterizing and synthesizing of those gels. The different gelation mechanisms of physical and chemical crosslinking were utilized to form polymer gels with properties and characteristics to serve as model systems for self-healing materials and as internal curing admixtures for concrete applications.

The first polymer gel studied in this work is a commercial triblock copolymer of poly(methyl methacrylate)-poly(n-butyl acrylate)-poly(methyl methacrylate) used as a thermoreversible physical gel through solvent interactions. These gels were implemented as model systems to develop a methodology for using shear rheometry to determine healing timescales and kinetics for fracture-healing materials. The extent of fracture was further studied to see effects on the time required for a fully healed network. The use of rheo-physical flow visualization with particle image velocimetry was implemented to verify and quantify fracture in the gel.

A chemically-crosslinked gel composed of polyacrylamide and silica nanoparticles was then synthesized as a composite hydrogel for use in concrete internal curing. A synthesis route to produce spherical polymer gel particles with varying loadings of silica nanoparticles from inverse suspension polymerization methods was presented. Gels were studied using optical microscopy, scanning electron microscopy, thermogravimetric analysis, and swelling tests.

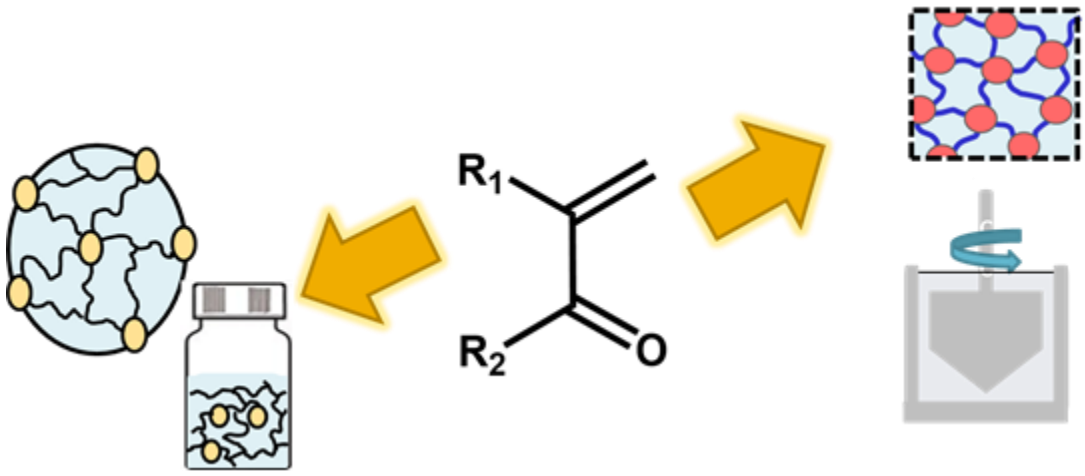

Figure 1-4 Illustration of acrylic-based monomer applications in the various projects

1.6 References

(1) Rubinstein, M.; Colby, R. H. *Oxford Univ. Press New York* **2003**.

(2) Naik, S. S.; Savin, D. A. *Macromolecules* **2009**, *42* (18), 7114–7121.

(3) Appel, E. A.; Tibbitt, M. W.; Webber, M. J.; Mattix, B. A.; Veiseh, O.; Langer, R. *Nat. Commun.* **2015**, *6*, 6295.

(4) Yao, C.; Lei, G.; Hou, J.; Xu, X.; Wang, D.; Steenhuis, T. S. *Ind. Eng. Chem. Res.* **2015**, *54* (43), 10925–10934.

(5) Abd Alla, S. G.; Sen, M.; El-Naggar, A. W. M. *Carbohydr. Polym.* **2012**, *89* (2), 478–485.

(6) Buczkowski, G.; Roper, E.; Chin, D.; Mothapo, N.; Wossler, T. *Entomol. Exp. Appl.* **2014**, *153* (3), 183–190.

(7) Mowery, C. L.; Crosby, A. J.; Ahn, D.; Shull, K. R. *Langmuir* **1997**, *13* (23), 6101–6107.

(8) Tong, J; Jerôme, R. *Polymer* **2000**, *41* (7), 2499–2510.

(9) Moineau, C.; Minet, M.; Teyssié, P.; Jérôme, R. *Macromolecules* **1999**, *32* (25), 8277–8282.

(10) Kiatkamjornwong, S.; Phunchareon, P. *J. Appl. Polym. Sci.* **1999**, *72* (10), 1349–1366.

(11) Mayoux, C.; Dandurand, J.; Ricard, A.; Lacabanne, C. *J. Appl. Polym. Sci.* **2000**, *77* (12), 2621–2630.

(12) Horkay, F.; Horkay, F.; Tasaki, I.; Tasaki, I.; Basser, P. J.; Basser, P. J. *Biomacromolecules* **2000**, *1* (3), 84–90.

(13) Tanaka, F.; Edwards, S. F. *Macromolecules* **1992**, *25* (5), 1516–1523.

(14) Tanaka, F. *Polymer Physics*; 2011.

(15) Odian, G. *Principles of Polymerization*; John Wiley & Sons, Inc.: Hoboken, NJ, USA, 2004.

(16) Radi, B.; Wellard, R. M.; George, G. A. *Soft Matter* **2013**, *9* (12), 3262.

(17) Ward, J. H.; Furman, K.; Peppas, N. A. *J. Appl. Polym. Sci.* **2003**, *89* (13), 3506–3519.

(18) Hiemenz, P. C.; Lodge, T. P. *Polymer Chemistry, Second Edition*; Taylor & Francis, 2007.

(19) Yesilyurt, V.; Webber, M. J.; Appel, E. A.; Godwin, C.; Langer, R.; Anderson, D. G. *Adv. Mater.* **2016**, *28* (1), 86–91.

(20) Yang, B.; Zhang, Y.; Zhang, X.; Tao, L.; Li, S.; Wei, Y. *Polym. Chem.* **2012**, *3* (12), 3235.

(21) Dong, R.; Zhao, X.; Guo, B.; Ma, P. X. *ACS Appl. Mater. Interfaces* **2016**, *8* (27), 17138–17150.

(22) Tan, R.; She, Z.; Wang, M.; Fang, Z.; Liu, Y.; Feng, Q. *Carbohydr. Polym.* **2012**, *87* (2), 1515–1521.

(23) Coussot, P.; Tocquer, L.; Lanos, C.; Ovarlez, G. *J. Nonnewton. Fluid Mech.* **2009**, *158* (1–3), 85–90.

(24) Divoux, T.; Barentin, C.; Manneville, S. *Soft Matter* **2011**, *7* (19), 9335.

(25) Hu, Y. T.; Lips, A. *J. Rheol.* **2005**, *49* (5), 1001.

(26) Tescione, G.; Ragni, D.; He, C.; Simão Ferreira, C. J.; van Bussel, G. J. W. *Renew. Energy* **2014**, *70*, 47–61.

(27) Santiago, J. G.; Wereley, S. T.; Meinhart, C. D.; Beebe, D. J.; Adrian, R. J. *Exp. Fluids* **1998**, *25* (4), 316–319.

(28) Raffel, M.; Willert, C.; Kompenhans, J. *Particle Image Velocimetry: A Practical Guide*; 2007.

(29) Cipriano, B. H.; Banik, S. J.; Sharma, R.; Rumore, D.; Hwang, W.; Briber, R. M.; Raghavan, S. R. *Macromolecules* **2014**, *47* (13), 4445–4452.

(30) Yarimkaya, S.; Basan, H. *J. Macromol. Sci. Part A Pure Appl. Chem.* **2007**, *44* (7), 699–706.

(31) Roy, S. G.; De, P. *Polymer* **2014**, *55* (21), 5425–5434.

(32) Mechtcherine, V.; Snoeck, D.; Schröfl, C.; De Belie, N.; Klemm, A. J.; Ichimiya, K.; Moon, J.; Wyrzykowski, M.; Lura, P.; Toropovs, N.; Assmann, A.; Igarashi, S.; De La Varga, I.; Almeida, F. C. R.; Erk, K.; Ribeiro, A. B.; Custódio, J.; Reinhardt, H. W.; Falikman, V. *Mater. Struct.* **2018**, *51* (1), 28.

(33) Gudeman, L. F.; Peppas, N. A. *J. Appl. Polym. Sci.* **1995**, *55* (6), 919–928.

(34) Horkay, F.; Tasaki, I.; Basser, P. J. *Biomacromolecules* **2001**, *2* (1), 195–199.

(35) Horkay, F.; Basser, P. J.; Hecht, A. M.; Geissler, E. *Proc. Inst. Mech. Eng. Part H J. Eng. Med.* **2015**, *229* (12), 895–904.

(36) Jensen, O.; Hansen, P. *Cem. Concr. Res.* **2001**, *31*, 647–654.

(37) Aïtcin, P. C. *Cem. Concr. Compos.* **2003**, *25* (4–5 SPEC), 409–420.

(38) Schröfl, C.; Mechtcherine, V.; Gorges, M. *Cem. Concr. Res.* **2012**, *42* (6), 865–873.

(39) Henkensiefken, R.; Bentz, D.; Nantung, T.; Weiss, J. *Cem. Concr. Compos.* **2009**, *31* (7), 427–437.

(40) De La Varga, I.; Castro, J.; Bentz, D.; Weiss, J. *Cem. Concr. Compos.* **2012**, *34* (9), 1001–1008.

(41) Van, V. T. A.; Rößler, C.; Bui, D. D.; Ludwig, H. M. *Cem. Concr. Compos.* **2014**, *53*, 270–278.

(42) Cusson, D.; Hoogeveen, T. *Cem. Concr. Res.* **2008**, *38* (6), 757–765.

(43) Zhu, Q.; Barney, C. W.; Erk, K. A. *Mater. Struct.* **2015**, *48* (7), 2261–2276.

(44) Mechtcherine, V.; Gorges, M.; Schroefl, C.; Assmann, A.; Brameshuber, W.; Ribeiro, A. B.; Cusson, D.; Custódio, J.; Da Silva, E. F.; Ichimiya, K.; Igarashi, S. I.; Klemm, A.; Kovler, K.; De Mendonça Lopes, A. N.; Lura, P.; Nguyen, V. T.; Reinhardt, H. W.; Filho, R. D. T.; Weiss, J.; Wyrzykowski, M.; Ye, G.; Zhutovsky, S. *Mater. Struct. Constr.* **2014**, *47* (3), 541–562.

(45) Jensen, O. M.; Hansen, P. F. *Cem. Concr. Res.* **2002**, *32* (6), 973–978.

(46) Lee, H.; Wong, H. S.; Buenfeld, N. R. . *Adv. Appl. Ceram.* **2010**, *109* (5).

(47) Krafcik, M. J.; Erk, K. A. *Mater. Struct. Constr.* **2016**, *49* (11), 4765–4778.

(48) Krafcik, M. J.; Macke, N. D.; Erk, K. A. *Gels* **2017**, *3* (4), 46.

(49) Davis, C. R.; Kelly, S. L.; Erk, K. A. *J. Appl. Polym. Sci.* **2018**, *135* (14), 1–10.

(50) Mo, K. H.; Ling, T. C.; Alengaram, U. J.; Yap, S. P.; Yuen, C. W. *Constr. Build. Mater.* **2017**, *139*, 403–418.

(51) Pedro, D.; de Brito, J.; Evangelista, L. *Constr. Build. Mater.* **2017**, *147*, 803–814.

(52) Diamond, S.; Sahu, S. *Mater. Struct. Constr.* **2006**, *39* (293), 849–859.

(53) Yoon, D. H.; Jang, J. W.; Cheong, I. W. *Colloids Surfaces A Physicochem. Eng. Asp.* **2012**, *411*, 18–23.

(54) Zhang, K.; Wang, Q.; Meng, H.; Wang, M.; Wu, W.; Chen, J. *Particuology* **2014**, *14*, 12–18.

CHAPTER 2. FRACTURE-HEALING KINETICS OF THERMOREVERSIBLE PHYSICAL GELS QUANTIFIED BY SHEAR RHEOPHYSICAL EXPERIMENTS

Portions of the following chapter contain text or figures adapted with permissions from **T.L. Thornell**, B.A. Helfrecht, S.A. Mullen, A. Bawiskar, and K.A. Erk, "Fracture-Healing Kinetics of Thermoreversible Physical Gels Quantified by Shear Rheophysical Experiments," ACS Macro Lett., 3 [10] 1069–1073 (2014). Copyright 2014 American Chemical Society. DOI: 10.1021/mz500524d

2.1 Introduction

Soft materials with well-defined mechanical properties are important in a variety of industrial and biomedical applications, including high toughness elastomers for seals and dampers[1] and hydrogels for synthetic cartilage[2] hemostatic materials for wound dressing,[3] injectable materials for regenerative medicine[4,5] and superabsorbent polymer hydrogels for applications as diverse as drug delivery to cement internal curing agents.[6] To exhibit optimum performance in these applications, the material's mechanical response to large applied deformations and their ability to heal following damage must be well understood. However, these nonlinear mechanical properties are difficult to characterize for soft materials using traditional experimental techniques. Standard tension and compression mechanical tests require self-supported samples and are thus not appropriate for materials that have fast relaxation times or contain large amounts of solvent.

Recent work has shown shear rheometry to be an effective technique for characterizing the nonlinear deformation and fracture of soft materials.[7–10] To correlate the measured rheological response with the sample's macroscale behavior (e.g., formation of a fracture plane), rheophysical experiments are performed to simultaneously measure the

local velocity profile during shear by employing a variety of techniques, including optical particle tracking[11], ultrasonic velocimetry,[12] and NMR.[13]

In this study, we describe a rheophysical methodology for quantifying the fracture and self-healing behavior of a soft material. A temperature-dependent, physically associating polymer gel will be utilized as a model soft material. Shear rheometry coupled with an optical particle tracking system was used to directly observe the shear-induced formation and subsequent healing of the fracture plane within the material. Compared to the characteristic stress relaxation behavior, fracture-healing occurred over much greater timescales but with similar temperature dependence. Activation energy for healing was found to be greater than for relaxation, most likely due to the entropic barrier required for a chain to re-associate with a network junction.

2.2 Materials and Methods

2.2.1 Materials

The triblock of poly(methyl methacrylate)(PMMA; 8,900 g/mol) end blocks and poly(*n*-butyl acrylate)(PnBA 53,000 g/mol) midblock was from Kuraray, Co. (Japan) and used as received. The 2-ethyl hexanol was purchased from Sigma-Aldrich and was used as received. Gels were stirred overnight at 60 °C to make the polymer solutions. At temperature (T) > 34°C, the copolymer self-assembles into a three-dimensional network of flexible midblock segments, or 'bridges', interconnected by spherical endblock aggregates (details described elsewhere[14]). Previous studies have investigated the mechanical behavior of this material until the point of failure[7,8,11,14] but have not yet addressed the post-fracture healing response.

2.2.2 Shear Rheometry

For Couette cell (Anton Paar, Model CC27) testing, gels were loaded at 50°C and were then subsequently cooled to testing temperatures (20-28 °C) at 2 °C/min using the Peltier temperature control of the rheometer (Anton Paar MCR 302). At testing temperatures, the samples were allowed to sit for 10-20 minutes before testing. The gels are then sheared at a constant shear rate ($\dot{\gamma}$) of 1 s^{-1} to measure the stress response resulting from shear-induced failure, referred to here as 'primary fracture'. The fractured gel is allowed to sit undisturbed at specific resting times (5 min to 14 hr) and is then deformed at the same shear rate to obtain the 'recovery fracture' stress response. The extent of strength recovery in the gel was determined from the ratio of the maximum shear stress for the recovery and primary fracture events.

2.2.3 Flow Visualization Methodology

All fracture events were confirmed by measuring the local velocity of the gel across the width of the rheometer fixture gap (1.5 mm) utilizing a custom-built particle tracking flow visualization system coupled to the rheometer. To achieve this, the gel (which is transparent) was seeded with ppm concentration of inert particles. For rheophysical experiments, which utilize a transparent Couette cell (Anton Paar, CC32), cooling and heating was dependent on water circulation and 30 minutes was allocated for cooling to testing temperatures.

The assembly of the rheophysical instrument was as follows. A plano-concave lens (effective focal length of -12.7 mm) and plano-convex lens (effective focal length of 150 mm) were placed in the path of a laser beam. The laser used was 'OBIS 405LX' from Coherent (Santa Clara, California, USA), with a wavelength of 405 nm and an output of

100mW. The CCD camera used was a ‘dicam pro’ from pcoTech (Romulus, Michigan, USA) with a spatial resolution of 1280 x 1024 pixels and temporal resolution of 8 frames per second (fps). For the shear rate used in this study, a frame rate of 5 fps was found to be optimum. To achieve the required magnification, a ‘Zoom 70XL’ lens from Qioptik (Rochester, New York, USA) was used along with a basic bottom function module and a TV tube of 1.0X. A function generator was used to externally trigger the camera at the required rate to capture images. The function generator itself was triggered by the rheometer to start at the exact moment that shear strain was applied. Inert silver-coated hollow glass microspheres of 10-20 μm diameter and a density of 0.49 g/cc from Cospheric (Santa Barbara, California, USA) were used. A particle concentration of 100 ppm was found to give the best results in terms of images acquired for satisfactory image processing. Captured images were analyzed using PTVlab, a MATlab plug in, first created by Antoine Patalono of the Universidad Nacional de Córdoba in Argentina and Brevis Wernher of the University of Sheffield in the U.K. Editing and revisions to the software code were performed to adapt to the custom-built rheophysical apparatus.

2.3 Results and Discussion

2.3.1 Flow Visualization of Fractured Gels

Figure 2-1 indicates the stress responses and corresponding velocity profiles of the primary and recovery fracture events. Focusing first on the primary fracture response (closed symbols in Figure 2-1A), the gel’s behavior can be investigated as a function of strain. A linear velocity profile was observed in Figure 2-1B that indicated an elastic response of the network at a strain of 3. Prior work has shown that the observed stress response maximum and sharp decrease is a direct results of the shear-induced strain

localization in the form of cohesive fracture of the gel.[11] The stress reduction is due to pull-out of elastically active chains within the polymer network[15,16] and formation of a region of dangling chains.[11] This fracture event was verified here: after the stress maximum, mid-gap fracture and elastic recoil are directly observed from the flow visualization data at a strain of 6 as seen in Figure 2-1C. The fracture plane appears to exist at $x = 0.6$, separating the section of the gel that is attached to the moving wall which maintains a fast positive velocity from the section of the gel attached to the stationary wall that transitions from near-zero relative velocity to displaying clear elastic recoil at the fracture plane (i.e., $v(x) < 0$). Figure 2-1D displays the post-fracture velocity profile of the gel at a strain of 9.

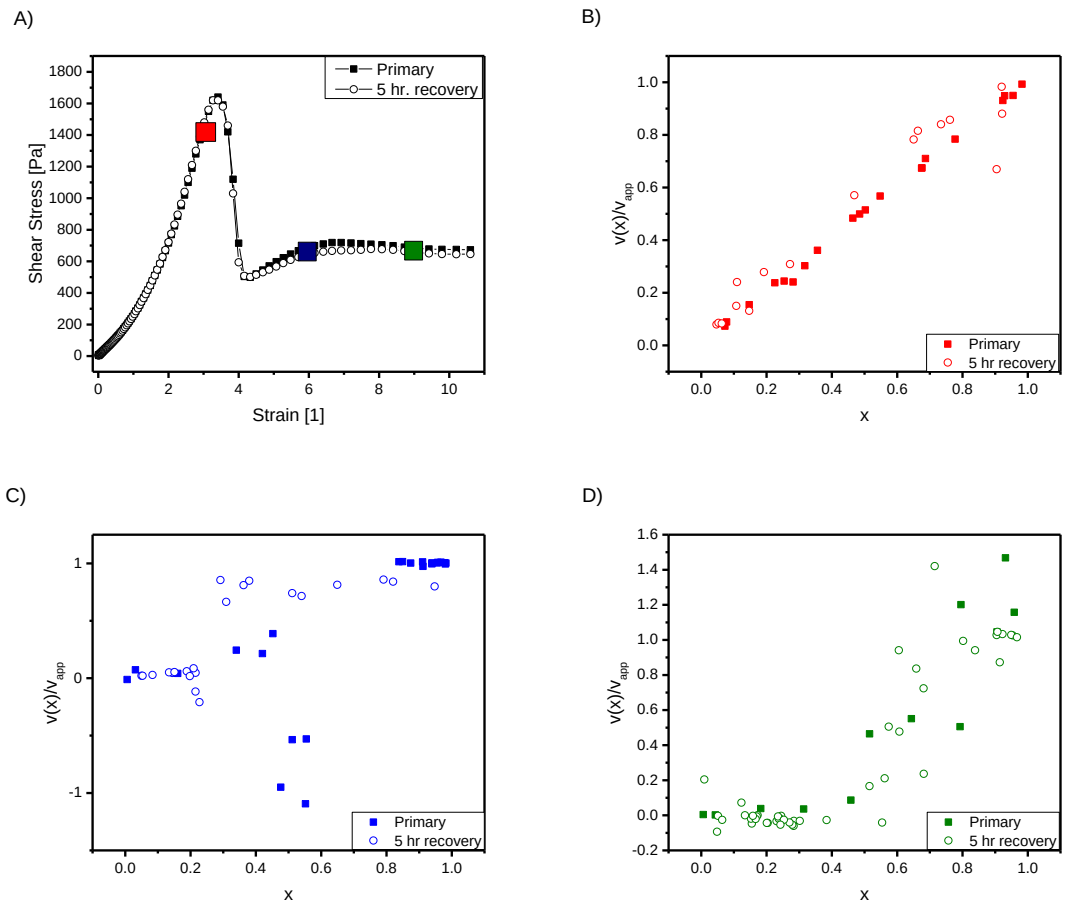

Figure 2-1 (A) Primary and 5 hr. recovery of a 5.5 vol % gel at 25 °C. Velocity profiles for three different strains during the primary and recovery events: (B) 3, (C) 6, and (D) 9 strain units. For B-D, the vertical axes report the local velocity, v(x), normalized by the applied velocity, v_{app} (1.41 mm/s), and the horizontal axes reports the location, x, within the normalized gap width (gap = 1.5 mm), where x = 0 is the location of the stationary wall of the fixture and x = 1 is the location of the moving wall.

The rheophysical results presented in Figure 2-1A are an example of the gel's ability to fully recover its strength during the 5-hr resting time between the primary and recovery fracture events. After 5 hrs, the gel was able to reform the elastically active midblock bridges that allow for the recovered stress maximum response. The calculated velocity profiles for this fracture showed similar characteristics. Most notably observed

was a change in the fracture plane as seen in Figure 2-1C; the fracture site within the observation window shifted to about x = 0.3.

2.3.2 Healing Timescales of Fractured Gels

For shorter resting times, the extent of network recovery was a strong function of time. Figure 2-2A presents the stress-strain curves for primary fracture and subsequent recovery fracture events after resting times of 5-45 min for a 25 °C 5.5 vol % gel. At a rest time of 5 minutes, the percent recovery is at 45 %. Increasing the rest time to 10, 30, and 45 minutes, the percent recovery increased to 59, 67 and 79 %, respectively. The fracture plane of a partially healed gel occurred at the same location as the primary fracture as incomplete healing resulted in visible voids within the gel which acted as stress concentration sites and subsequently decreased the observed maximum stress response.

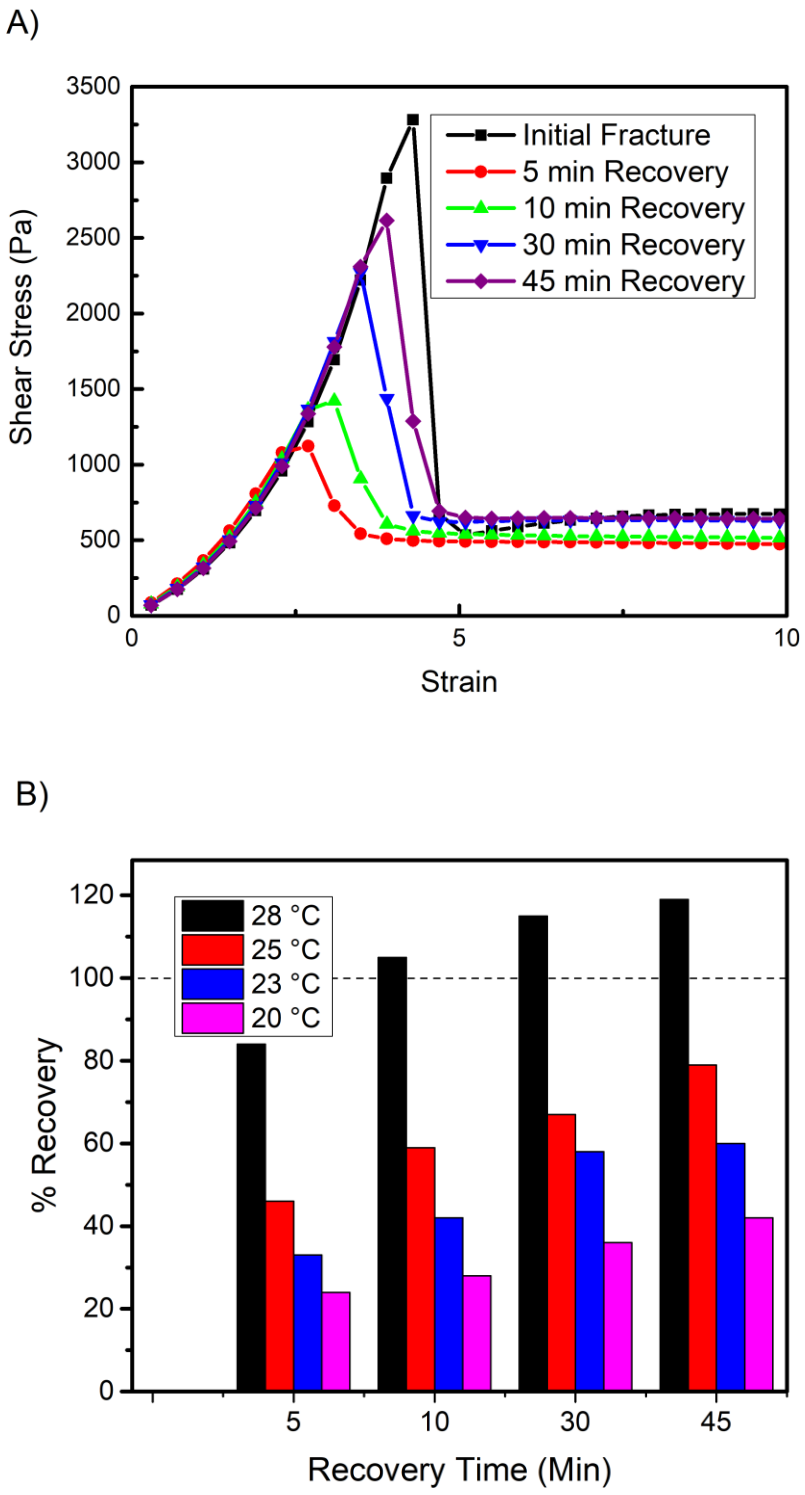

Figure 2-2 (A) Stress-strain curves of 25 °C 5.5 vol. % gel with primary and resting times of 5-45 mins. (B) % recovery versus resting times of 5-45 mins for temperatures ranging from 28 °C to 20 °C for a 5.5 vol. % gel.

Given sufficient resting time, the network can regain its original strength, and the primary and recovery stress responses almost perfectly overlap (see Figure 2-1A). Strength recovery was found to be accelerated by increasing temperature of the system. This is shown in Figure 2-2B. Gels at the higher temperatures of 28 and 25 °C were able to recover at a faster rate than gels at the lower temperatures of 23 and 20 °C.

The time for 100% strength recovery, referred to here as the 'full recovery time', was determined from a power law fit to the experimental data (see Figure 2-3). Compared to direct experimental observation of full recovery, this was a preferred method to determine the full recovery time because at these much longer timescales (>250 min), solvent evaporation may begin to influence the data.

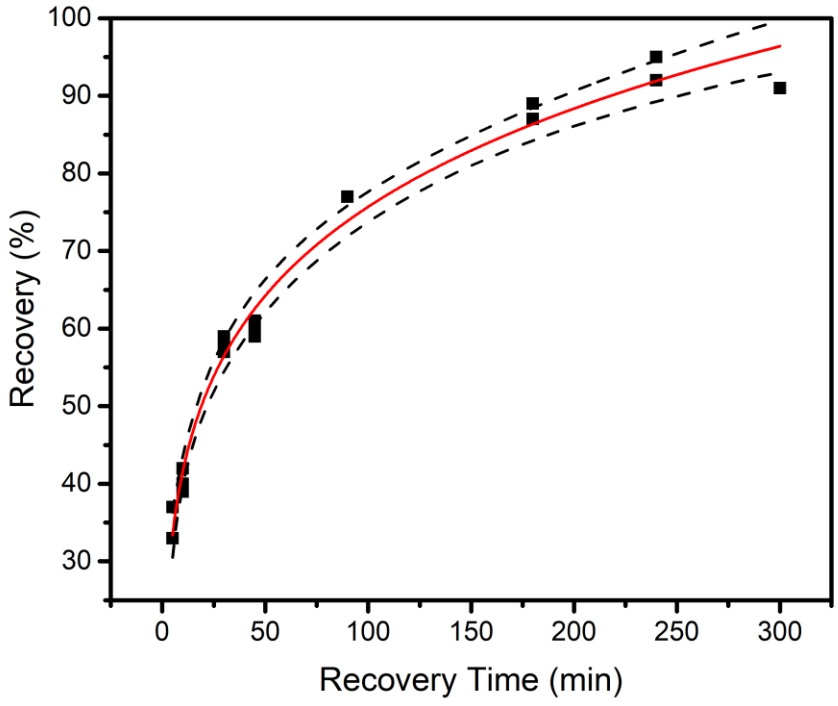

Figure 2-3 Recovery response of 23 °C, 5.5 vol. % gel with 95 % confidence intervals, described by $y = a + bx^n$, where y is percent recovery, x is recovery time, and a = -45, b = 62, and n = 0.14 are fitting parameters.

Degree of recovery was also found to be a strong function of gel concentration. Table 2-1 summarizes the full recovery times of 5, 5.5, and 6 vol % gels. For 5 vol % gels, the recovery times ranged from 3-670 min. As concentration is increased, the time ranges grow to 11-1100 min for 5.5 vol % and 25-1600 min for 6 vol %.

Table 2-1 Full recovery times and relaxation times at various temperatures and concentrations

Concentration (vol %)	**Temperature (°C)**	**Full Recovery Time (min)**	**Relaxation Time (sec)**
5.0	28	3	2.4
	25	40	10
	23	150	50
	20	670	120
5.5	28	11	2.5
	25	50	20
	23	360	40
	20	1100	130
6.0	28	25	3
	25	210	20
	23	400	30
	20	1600	120

2.3.3 Determination of Characteristic Gel Relaxation Times

Following previous methods, characteristic relaxation times for each gel concentration and temperature were determined from stretched exponential curve fits to step strain experimental data, in which a strain of 5% is applied to the gel and stress relaxation is measured as a function of time. The stretched exponential fitting equation is shown in Equation 2.1,

$$G(t,\gamma_0) = G(0,\gamma_0)\exp[-(\frac{t}{\tau})^{\beta}], \quad (2.1)$$

where $G(0,\gamma_0)$ is the zero-time storage modulus (determined by G' value at γ = 5% and ω = 100 rad s^{-1}), τ is the characteristic relaxation time of the gels, and the exponential term β = 1/3 is related to the relaxation time for this physically associating system as described in Ref. 8.

Figure 2-4 illustrates the stress relaxation behaviors for the various temperatures and concentrations with the fit line of equation 1 on each data set. These values of τ are reported in Table 2-1 and the zero-time storage moduli are summarized in Table 2-2. As the gel concentration was increased from 5 to 6 vol %, the larger storage modulus values indicated stiffer polymer networks. Even though G(0) values were dependent on both concentration and temperature, the values for the characteristic relaxation times were more dependent on temperature. For higher temperatures, the relaxation times were 2.4-3 seconds for 28°C and 10-20 seconds for 25°C. The relaxation times were longer for the lower temperatures ranging from 30-50 seconds for 23°C and 120-130 seconds for 20°C.

Table 2-2 Small strain storage modulus at various temperatures and concentrations

Concentration (vol. %)	**Temperature (°C)**	**G(0) (Pa)**
5	28	90
	25	140
	23	180
	20	250
5.5	28	180
	25	260
	23	310
	20	400
6	28	300
	25	410
	23	470
	20	540

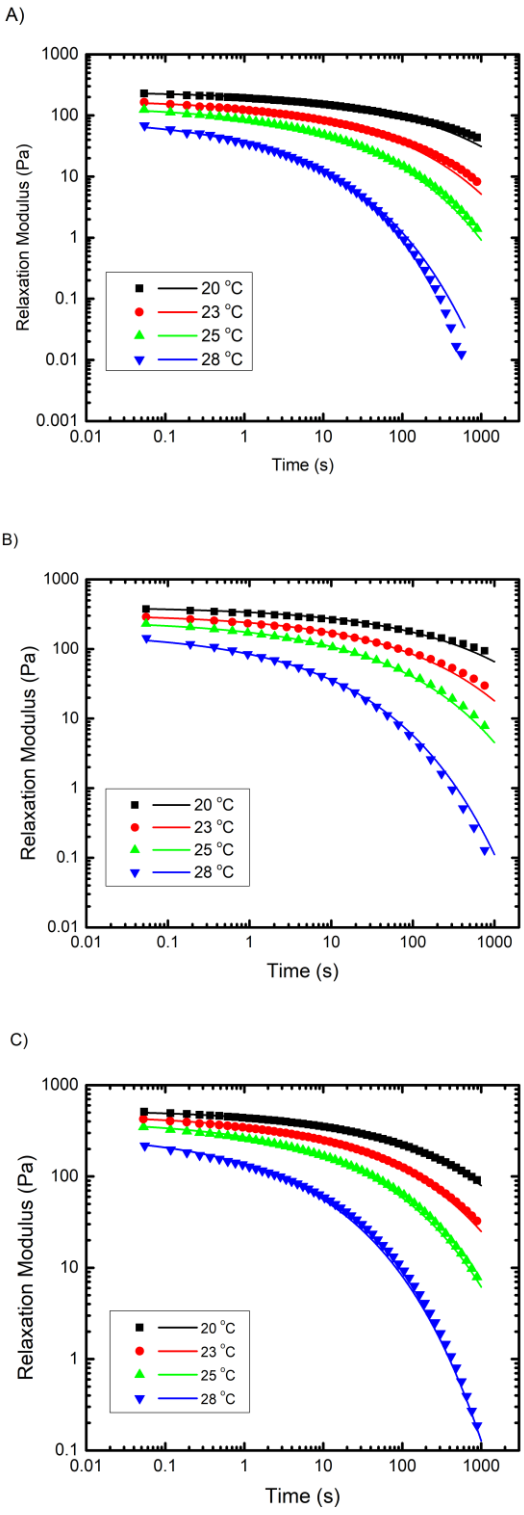

Figure 2-4: Relaxation moduli for temperatures 28-20 °C fitted to Equation 2.11 for (a) 5 vol %, (b) 5.5 vol %, and (c) 6 vol % at various temperatures

2.3.4 Kinetics of Fully Healed Networks

Arrhenius-type relationships of ln(1/recovery time) and inverse temperatures of 20-28 °C , as shown in Figure 2-5, allowed for the calculation of activation energies related to the recovery or 'healing' behavior ($E_{a,rec}$). Recovery activation energies were observed to decrease with increasing concentration: $E_{a,\,rec}$ = 500 kJ/mol for 5 vol % gel; 440 kJ/mol for 5.5 vol%; 370 kJ/mol for 6 vol%.

Interestingly, previously reported characteristic stress relaxation times (τ) for these gels displayed a similar Arrhenius dependence on temperature.[8] From this data, activation energies related to the relaxation behavior ($E_{a,relax}$) were found to weakly dependent on gel concentration, with $E_{a,relax}$ = 370, 360, and 330 kJ/mol for 5, 5.5, and 6 vol % gels, respectively. In past work with higher concentration gels,[14] the activation energies determined from the Arrhenius dependence of relaxation times were believed to be related to the energy required for chain pull-out of a stressed, elastically active bridge from its network junction (i.e., endblock aggregate).

One striking observation was that the relaxation times were over an order of magnitude smaller than the recovery times. This is most likely because the small strain nature of the step-strain experiments that probe the relaxation behavior do not deform the network as greatly as the non-linear, large strain fracture experiments which often resulted in macroscopic voids within the gel sample. For stress relaxation, the region of disorder caused by chain pull-out is on the order of 10 nm but is increased to on the order of μm-mm for shear-induced fracture. The initial gelation kinetics are a closer match to the time scales of recovery as both are comparable at the magnitude of minutes.

The relaxation and recovery behaviors display similar dependences on temperature, with increasing temperature resulting in faster relaxation or recovery behavior of the gel.

This is consistent with the thermoreversible nature of the physically associating triblock copolymer network and specifically the enthalpically driven self-assembly process to form the network. Both the relaxation and recovery behaviors also display similar dependence on gel concentration, with higher concentration gels having reduced activation energies.

For all gel systems investigated here, we observed that $E_{a,rec}$ was larger than $E_{a,relax}$. This implies that the energy required to insert a dangling endblock into a network junction is greater than the energy required to remove an elastically active endblock. Considering the thermodynamics of the system, there is an inherent entropic barrier for healing to occur, as healing requires a freely dangling chain to insert into an endblock aggregate (or form a new aggregate). By comparison, it is entropically favorable to remove a chain from confinement within an aggregate. To better understand this behavior, including the enthalpic contribution to the behaviors, future studies will need to investigate the dependence of activation energy on endblock molecular weight and solvent quality. Additionally, recent simulation results suggest that the relative aggregate size may change as a result of the shear-induced fracture and healing process.[17]

The gels were able to surpass their original strengths (> 100% recovery) at 28 °C for all tested concentrations. The self-healing and eventual strengthening of gels at 28 °C cannot be attributed to a singular cause. The network structure at this relatively high temperature does exhibit solid-like gel characteristics but very fast relaxation ($\tau < 3$). Thus, these higher temperature systems may have some variability in the network structure compared to the lower temperature systems. For example, midblocks may form elastically inactive loops instead of bridges in the initial gel structure, which would ultimately decrease the maximum stress response of the sheared gel (observed here and reported

elsewhere[14]). Following shear-induced fracture, if any of the loops formed bridges upon healing, this would cause a corresponding increase in the maximum stress response and result in > 100% recovery.

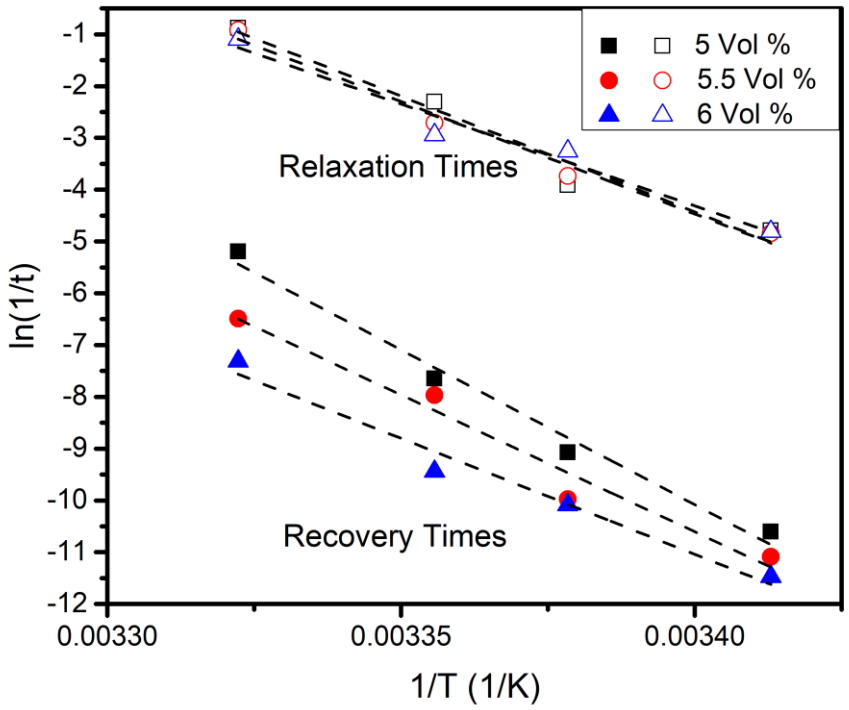

Figure 2-5 Arrhenius relationships where t (sec.) represents recovery times or characteristic relaxation times (τ) for the various concentrations.

Additional experiments were performed to determine if the strengthening effect was due to aging of the system or solvent evaporation. Prior to the primary fracture experiment, gels were held for 5-90 min at a fixed temperature (28 and 25 °C). At relatively large aging times (> 30 min), significant reductions in the maximum stress were observed and attributed to syneresis-type behavior[18–20], where recovery was significantly decreased as solvent could be expelled from the network. Aging time of > 30 min displayed behavior similar to what is reported here, including > 100% recovery. It is expected that solvent

evaporation would cause an increase in the primary fracture stress maximum. However, at the resting times investigated here, solvent evaporation was not believed to be significant as the stress maximum of the primary fracture event of same temperature did not vary between repeated experiments with the same gel sample.

2.4 Conclusions

The fracture-healing kinetics of thermoreversible triblock copolymer gels were studied to understand the timescales and energetics of full network healing. Rheophysical Flow visualization experiments using particle image velocimetry were able to confirm fracture events occurred as opposed to other flow instabilities. Fully healed networks were also shown not to fracture in the same area indicating that no residual or weak areas remained in the network to propagate the original fracture. Timescales of fully healed networks ranged from minutes for warmer temperature of 28 and 25 °C to several hours for 23 and 20°C. These measured times were an order of magnitude greater than the characteristic relaxation times of the system. The activation energies for both stress relaxation and healing were compared using Arrhenius relationships with the energy barrier for fully healed networks to be larger for all gel concentrations studied due to the re-insertion of dangling chains into network junctions during healing.

2.5 References

(1) Ducrot, E.; Chen, Y.; Bulters, M.; Sijbesma, R. P.; Creton, C. *Science* **2014**, *344* (6180), 186–189.

(2) Sun, T. L.; Kurokawa, T.; Kuroda, S.; Ihsan, A. Bin; Akasaki, T.; Sato, K.; Haque, M. A.; Nakajima, T.; Gong, J. P. *Nat. Mater.* **2013**, *12* (10), 932–937.

(3) Dowling, M. B.; Kumar, R.; Keibler, M. A.; Hess, J. R.; Bochicchio, G. V; Raghavan, S. R. *Biomaterials* **2011**, *32* (13), 3351–3357.

(4) Yan, C.; Mackay, M. E.; Czymmek, K.; Nagarkar, R. P.; Schneider, J. P.; Pochan, D. J. *Langmuir* **2012**, *28* (14), 6076–6087.

(5) Olsen, B. D.; Kornfield, J. A.; Tirrell, D. A. *Macromolecules* **2010**, *43* (21), 9094–9099.

(6) Zhu, Q.; Barney, C. W.; Erk, K. A. *Mater. Struct.* **2015**, *48* (7), 2261–2276.

(7) Erk, K. A.; Henderson, K. J.; Shull, K. R. *Biomacromolecules* **2010**, *11* (5), 1358–1363.

(8) Erk, K. A.; Shull, K. R. *Macromolecules* **2011**, *44* (4), 932–939.

(9) Skrzeszewska, P. J.; Sprakel, J.; de Wolf, F. A.; Fokkink, R.; Cohen Stuart, M. A.; van der Gucht, J. *Macromolecules* **2010**, *43* (7), 3542–3548.

(10) Rossow, T.; Habicht, A.; Seiffert, S. *Macromolecules* **2014**, *47* (18), 6473–6482.

(11) Erk, K. A.; Martin, J. D.; Hu, Y. T.; Shull, K. R. *Langmuir* **2012**, *28* (9), 4472–4478.

(12) Gallot, T.; Perge, C.; Grenard, V.; Fardin, M.-A.; Taberlet, N.; Manneville, S. *Rev. Sci. Instrum.* **2013**, *84* (4), 45107.

(13) Manneville, S. *Rheol. Acta* **2008**, *47* (3), 301–318.

(14) Seitz, M. E.; Burghardt, W. R.; Faber, K. T.; Shull, K. R. *Macromolecules* **2007**, *40* (4), 1218–1226.

(15) Baumberger, T.; Caroli, C.; Martina, D. *Nat. Mater.* **2006**, *5* (7), 552–555.

(16) Baumberger, T.; Caroli, C.; Martina, D. *Eur. Phys. J. E. Soft Matter* **2006**, *21* (1), 81–89.

(17) Billen, J. Simulated associating polymer networks, The Claremont Graduate University, 2012.

(18) Faers, M. A.; Choudhury, T. H.; Lau, B.; McAllister, K.; Luckham, P. F. *Colloids Surfaces A Physicochem. Eng. Asp.* **2006**, *288* (1–3), 170–179.

(19) Adams, D. J.; Mullen, L. M.; Berta, M.; Chen, L.; Frith, W. J. *Soft Matter* **2010**, *6* (9), 1971.

(20) Liu, Y.; Lloyd, A.; Guzman, G.; Cavicchi, K. A. *Macromolecules* **2011**, *44* (21), 8622–8630.

CHAPTER 3. THE IMPACT OF DAMAGE ACCUMULATION ON THE KINETICS OF NETWORK STRENGTH RECOVERY FOR A PHYSICAL POLYMER GEL SUBJECTED TO SHEAR DEFORMATION

The following was reprinted with permissions from **T.L. Thornell**, K. Subramaniam, and K.A. Erk, "The impact of damage accumulation on the kinetics of network strength recovery for a physical polymer gel subjected to shear deformation," J. Polym. Sci. Part B Polym. Phys., 54 [17] 1693–1701 (2016). DOI: 10.1002/polb.24071

3.1 Introduction

A growing number of studies in the biomedical community are focused on the successful delivery of therapeutic drugs and cells for regenerative medicine applications.[1–3] A common route of delivery to the patient is through syringe injection. The high shear stresses present during injection would likely damage cells and disrupt viability.[4] However, by using a self-healing material as a carrier, it is believed that the cells can be better protected from external forces. These materials work to protect the cargo during injection by dissipating the force of the applied shear from the syringe and self-heal at the injection site to continue the release of the cells. Self-healing materials have been used as biomedical bone cements[5] to dental fillings[6] as well as self-healing coatings[7] and carbon fiber matrix composites.[8]

Polymer gels exhibiting a self-healing response are a suitable material class to use for injection delivery. Specifically, physical polymer gels could be particularly useful materials. These gels are composed of three-dimensional transient networks that have crosslinks formed via bonding from electrostatic, enthalpic or hydrogen bonding in

response to environment (pH, temperature, etc.)[9] which differentiates them from chemical (covalent) crosslinked gels.[10] Gels that absorb water or biological fluids within the network are referred to as polymer hydrogels. Researchers have designed many different injectable hydrogels using pluronics[11], chitosan[12] and polymer-grafted nanoparticles.[13]

Many physical gels display self-healing behavior, but the kinetics and the governing timescales of network healing have not been fully investigated. Experiments quantifying the healing timescales of the networks are difficult to perform due to the viscoelastic nature of the gels. Viscoelastic gels are more difficult to characterize due to the relaxation of the viscous portion of their mechanical response. Conventional mechanical testing methods such as compression and tensile tests are more suitable for self-supporting and high-modulus "tough" gels such as double network hydrogels,[14,15] which do not relax significantly during the timescales of the measurement. These types of materials can be used for cartilage and tissue replacements.[16]

Several methods for characterizing the fracture-healing behavior of viscoelastic gels have been proposed in literature using shear rheological experiments.[13,17–20] These methods typically use oscillation based measurements to evaluate post-deformation strength recovery and are similar to the tests used to measure network gelation kinetics.[21,22] For "shear thinning" injectable materials, the material's storage modulus (G') is the critical parameter used to quantify self-healing behavior because it describes the elastic character of the material. These tests are performed in the following way. First, the material is deformed in rotation at very high shear rates (~100-1000 s^{-1}) causing the storage modulus to rapidly decrease. Second, by performing oscillatory measurements at constant frequency and small strain amplitude, G' is typically observed to increase over time to match its

original value, which is thought to indicate full strength recovery or “healing” of the material.[17, 23]

In our previous work, fracture-healing behavior was investigated by rotational constant shear rate experiments to probe fracture and shear banding of physically associating gels.[24] The shear stress response of the network was measured as a function of strain, and simultaneous flow visualization was performed to directly correlate the measured overshoots in the shear stress response with shear-induced strain localization taking place within the gels in the form of macroscale fracture planes and shear bands.

In more recent work, this rotational testing technique was adapted to quantify the ability and speed of the fractured gels to heal by halting the applied shear rate and allowing the gels to rest unperturbed for a set time before undergoing a second regime of applied shear.[25] This “shear-rest-shear” measurement protocol is different from the oscillatory techniques used by others[13,17–20], in which the gel was always exposed to some small amount of deformation during the period of recovery. The applied shear rate (1 s^{-1}) is also much lower than those used to shear thin materials discussed previously for the oscillation time sweeps.

In this article, we report the effects of damage accumulation on the fracture-healing kinetics of model acrylic triblock thermoreversible gels. A brief review and discussion of previous work will be presented. The remainder of the paper will investigate the effects of total strain duration on the gels. By investigating gels at near-fracture strains, the recovery timescales are hypothesized to decrease due to reduced damage accumulation.

3.2 Materials and Methods

3.2.1 Materials

The model triblock gel from Kuraray Co. (Japan) consisted of poly(methyl methacrylate) (PMMA) end blocks of molecular weight of 8.9 kg/mol connected with a poly(n-butyl acrylate) (PnBA) midblock of 53 kg/mol. The polymer was dissolved in a midblock selective solvent, 2-ethyl hexanol (Sigma Aldrich, used as received), to form gels at concentrations of 5.0, 5.5, and 6.0 vol. %. Concentrations were selected to be above the critical micelle concentration of the solution and below the maximum torque limit of the rheometer.[26] Samples were prepared in scintillation vials and mixed at 80°C for 4 hours to form polymer solutions. Vials were then cooled to below a critical temperature of 34°C to form gels. For temperatures below 34°C, the network self assembles into PMMA endblock junctions connected by PnBA bridges.[26, 27] The temperature-dependent nature of these gels is reflected in their characteristic relaxation times (τ_c) and small-strain (elastic) shear modulus values (G(0)) that are reported in Table 3-1.[25] as temperature is increased, the gels become mechanically weaker and more easily deformed (i.e., G decreases) and τ_c decreases significantly, indicating a shift to more viscous, liquid-like behavior in which any applied external stress would be quickly relaxed by the system.

Table 3-1 Summary of the characteristic relaxation times (τ_c), and the small-strain shear modulus (G(0)) for 5-6 vol. % gels[25]

Concentration (vol. %)	**Characteristic Relaxation Time (sec)**				**Small-Strain Shear modulus (G(0))**			
	28°C (sec)	**25°C (sec)**	**23°C (sec)**	**20°C (sec)**	**28°C (sec)**	**25°C (sec)**	**23°C (sec)**	**20°C (sec)**
5	2.4	10	50	120	90	140	180	250
5.5	2.5	15	40	130	180	260	310	400
6.0	3	20	30	120	300	410	470	540

3.2.2 Rheometery

Rotational shear rheometry experiments were conducted with an Anton Paar MCR 702 with a concentric cylinder fixture (CC27 cup-and-bob; gap=1 mm). The vial containing the sample (i.e., a gel at some set polymer concentration) was heated and the sample was poured into the fixture cup and cooled at a rate of 2°C/min to desired testing temperature (ranging from 28-20°C). The sample was allowed to equilibrate for 30 minutes. Figure 1 presents a visual representation of the "shear-rest-shear" measurement protocol, including some representative data. The protocol began by initiating a shear start-up test with constant shear rate ($\dot{\gamma}$) of 1 s^{-1} to the sample. The shear stress response was measured as a function of strain, and the observed stress overshoot was referred to as the sample's "primary fracture." Next, the sample was allowed to rest unperturbed in the rheometer for a set "resting time" (t). Then, the same shear rate was re-applied and a new stress overshoot was observed, referred to as the sample's "recovery fracture." The amount of strength recovered during the prescribed resting time was quantified by a ratio of stress maxima

from the primary and recovery fracture responses (see Figure 3-1). Multiple tests were performed on each sample as the thermoreversible gel's mechanical history could be reset upon heating and cooling.

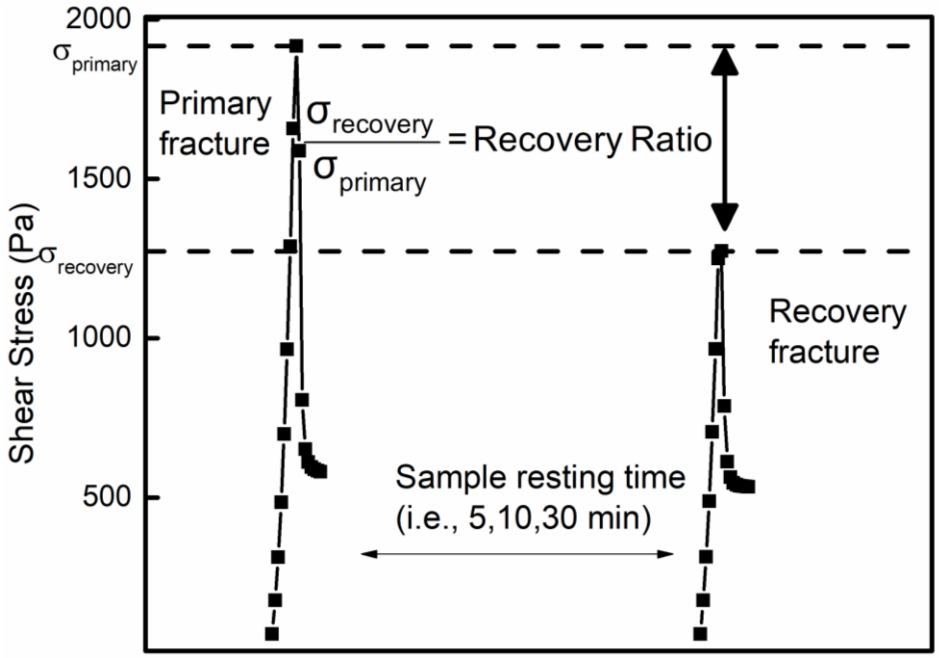

Figure 3-1 The "shear-rest-shear" measurement protocol, including representative shear stress versus time data for a 5.5 vol. % gel deformed at 23°C with a set resting time of 10 minutes

3.2.3 Particle Image Velocimetry

Following from our previous work, rheophysical measurements were used to directly correlate the shear-induced overshoots observed in a sample's stress response with the onset of cohesive (i.e., mid-gap) fracture taking place in the sample. To achieve this, rheometry measurements coupled with simultaneous particle image velocimetry[24,25,28] were performed with a custom-built assembly employing an Anton Paar MCR 302 shear rheometer with a transparent concentric cylinder fixture (Anton Paar CC32; gap = 1.5 mm). Temperature was controlled by a water bath and equilibrated for 30 minutes prior to testing. Details on the rheophysical instrumentation have been described previously[25,29] and are

briefly summarized here. For particle tracking, samples are loaded with a 200 ppm concentration of 10-20 μm diameter silver-coated hollow glass microspheres. To illuminate the microspheres, a 405 nm wavelength laser (OBIS 405LX, Coherent) was guided into a laser sheet by concave and convex lenses and directed across the 1.5 mm gap of the transparent rheometer fixture (containing the sample). A CCD camera (dicam pro, pcoTech) with spatial resolution of 1280 x 1024 pixels and temporal resolution of 8 frames per second (fps) was appropriately positioned below the rheometer fixture to capture images of the plane of illuminated microspheres. For increased magnification, a Zoom 70XL lens (Qioptik) with basic bottom function module and 1.0X TV Tube was attached to the camera. A function generator and an oscilloscope were required to connect the rheometer and camera to take pictures at the required rate when experiments were started. Captured images were analyzed using PTVlab.[30] Previous work has shown no evidence of wall slip during testing of these gels.[24,25]

3.3 Results and Discussion

3.3.1 Relationship between Gel healing kinetics and characteristic relaxation behaviors

In previous work[25], the fracture-healing behavior of the thermoreversible gels was studied using constant shear rate experiments over a total strain duration of 40 absolute units (4000% or γ_{40}) during the primary and recovery fracture tests separated by a set resting time that ranged from 5 minutes to several hours. By comparing the values of the stress overshoot maxima (recall Figure 3-1), the ratio of recovered strength was calculated; this ratio is reported as a percentage in Figure 3-2A for all gel concentrations and temperatures. Larger percentages indicated that during a given resting time, the gel was able to more completely heal and recover its mechanical strength, and longer resting times

equated to greater percentages. This behavior is explained by the underlying fracture-healing mechanisms: the sharp stress relaxation indicated by the stress overshoot is due to the breakdown of the gel's self-assembled network structure by shear-induced removal of elastically active chains from their respective network junctions; and while the fractured gel is at rest, strength recovery or "healing" occurs when those dangling chains are able to re-associate into new network junctions and become elastically active again. The data also indicates that at each resting time, a wide range of stress recovery values were possible depending on the temperature of the system. For example, for relatively short resting times of 5 min, the stress recovered values ranged from 23% at 20°C to 99% at 28°C. Thus, increased temperature led to faster healing kinetics for all gel concentrations investigated here.

From Figure 3-2A, it is clear that the healing kinetics can be expressed as power law-type relationships for each temperature. In past work, time-temperature Arrhenius activation energy relationships were used to describe the healing kinetics. However, a more useful comparison to make is with the sample's characteristic relaxation time (τ_c). Figure 3-2 reports the same data as Figure 3-2A but now the resting times are normalized by the appropriate τ_c values from Table 3-1. The characteristic relaxation time values were determined from fitting a stretched exponential equation to relaxation modulus data obtained from step-strain experiments at different temperatures with a relatively small value of applied strain (5%, within the linear viscoelastic regime of the system).[26] For physical gels, including those studied here, τ_c can be thought of as the time required for the removal of elastically active molecules from their network junctions and subsequent relaxation of the stress within the molecule.[27]

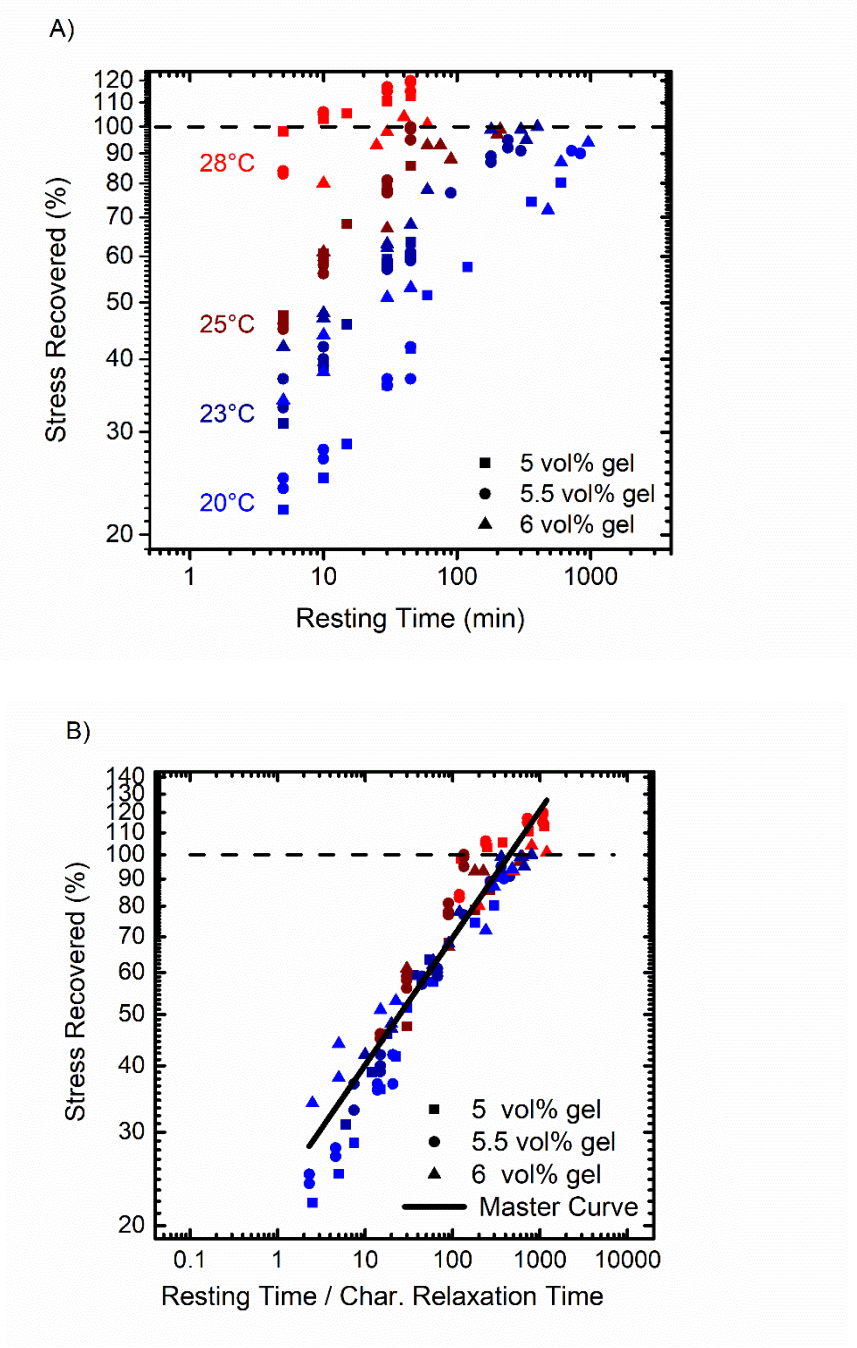

Figure 3-2 (A) Stress recovery as a function of resting time (t) for gels deformed at various concentrations and temperatures with the shear-rest-shear measurements protocol (γ_{40} data) . (B) Data normalized by the characteristic relaxation times (τ_c) of the gel.

As seen in Figure 3-2B, after normalization the data collapsed into an almost uniform trend described by a power law mathematical relationship. Table 3-2 summarizes the power law best fit equations for each gel concentration as well as the master curve, which is displayed in Figure 3-2B. From this analysis, we see that the time required for complete, 100% stress recovery of a fractured gel (referred to hereafter as the t_{100}) was on the order of 100-1000 times respective τ_c of the polymer networks. The t_{100} values for all samples investigated in this study are summarized in Table 3-3. Since healing was found to be dependent on resting time and system temperature, a fractured gel was able to fully heal if given sufficient rest, and healing was accelerated by increasing the temperature of the system.

Table 3-2 Power law best fit parameters for $y=ax^b$ of γ_{40} data, where y=stress recovered as a percentage and $x= t/\tau_c$, with a as the intercept and b as the exponent of healing.

Concentration (vol.%)	Intercept	Exponent of healing
5.0	19.92 $\pm$ 2.47	0.268 $\pm$ 0.025
5.5	21.50 $\pm$ 2.59	0.260 $\pm$ 0.024
6.0	30.03 $\pm$ 0.97	0.184 $\pm$ 0.005
Master Curve	23.09 $\pm$ 2.40	0.240 $\pm$ 0.020

Table 3-3 Values of t_{100} (min) for fully healed networks determined from γ_7 and γ_{40} shear-rest-shear experiments; values from γ_7 experiments are in parenthesis

Concentration (vol. %)	28°C (min)	25°C (min)	23°C (min)	20°C (min)
5.0 γ_{40} (γ_7):	3 (21-43)	40 (142-170)	150 (67-200)	700 (1060)
5.5 γ_{40} (γ_7):	11 (20-56)	50 (92)	350 (151-258)	1100 (934)
6.0 γ_{40} (γ_7):	25 (42-82)	210 (56-97)	400 (85-156)	1600 (556-921)

3.3.2 Reduced Strain Duration on Healing Timescales

To more thoroughly investigate how the magnitude of the total applied strain in shear experiments may potentially influence the observed gel healing behavior, the shear-rest-shear measurement protocol was altered to reduce the total strain applied to samples during the "primary" and "recovery" constant shear rate experiments from 40 units of strain to only 7 units (illustrated in Figure 3-3). These different data sets will be referred to as γ_{40} (already discussed in the last section, see Figure 3-2) and γ_7. The strain duration of 7 (700%) allowed for experiments to be completed near the decrease in shear stress response (i.e., the primary fracture of the gel). Figure 3-3 illustrates the difference in strain magnitude between γ_7 and γ_{40} and the reproducibility of the shear stress maximum.

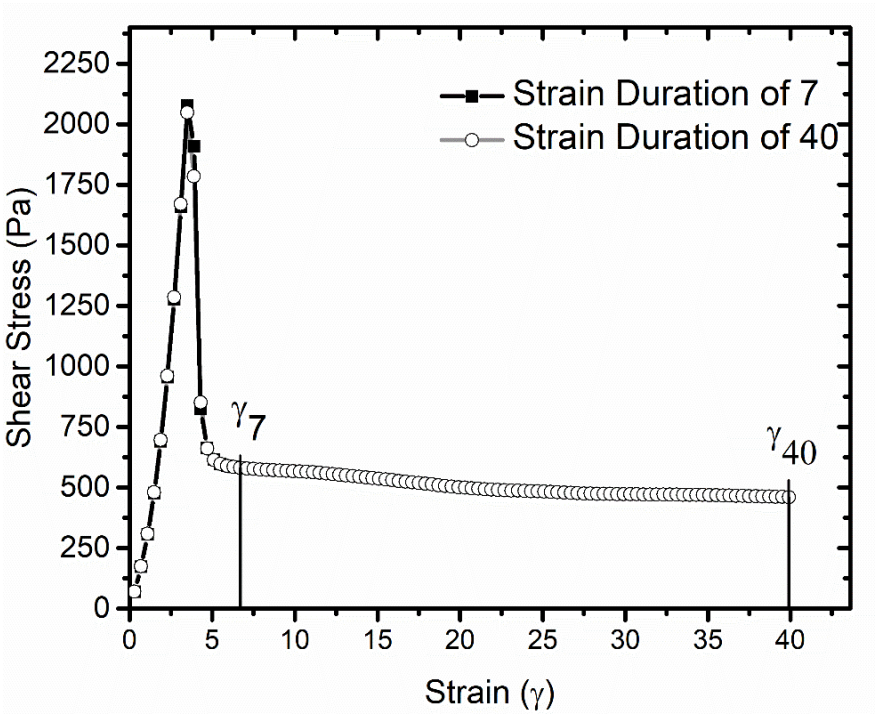

Figure 3-3 Stress responses during constant shear rate experiments for a 23 °C 5.5 vol. % gel, illustrating the difference in total strain duration for the γ_7 and γ_{40} experiments.

The effects of varying resting times on stress recovery can be seen in Figure 3-4 for a 5.5 vol. % gel tested at 23°C. Similar to γ_{40} experiments analyzed in the past[25], the maximum of the stress overshoot (and thus the percentage of stress recovered) increased with resting time in the γ_7 experiments. For 10 min, only 40 % of the gel's initial strength was recovered, but recovery increased to 65 % after 30 min and 80 % after 45 min. Increasing the resting times to hours resulted in 90 % recovery after 1 hour, 95 % after 2 hours and > 99 % after 4 hours

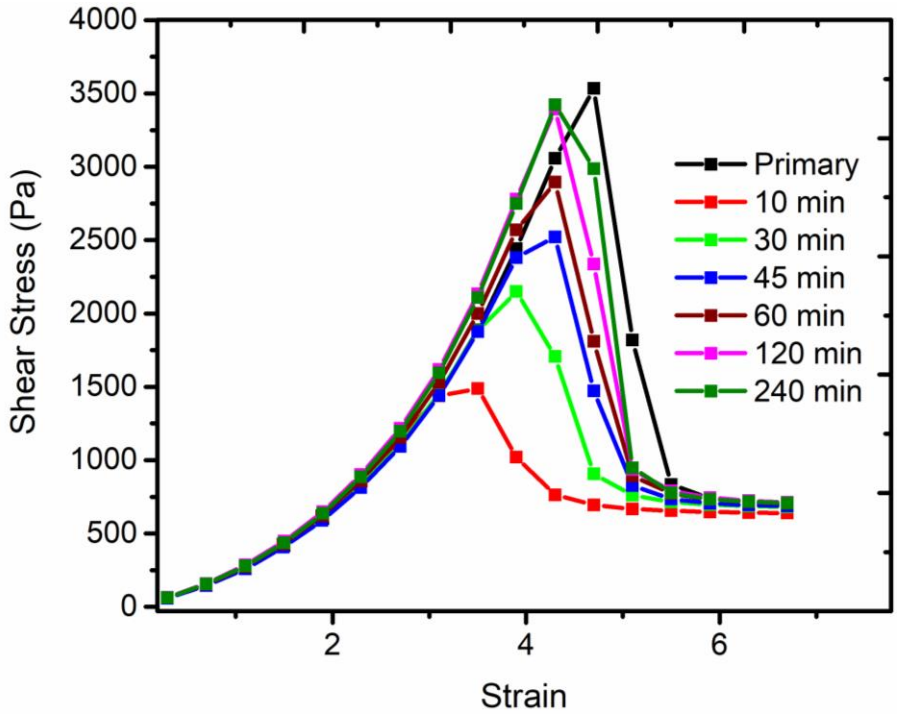

Figure 3-4 Primary and recovery fracture stress responses for γ_7 experiments of a 5.5 vol. % gel tested at 23 °C for various resting times.

Figure 3-5 reports the stress recovery of a 23°C, 5.5 vol. % gel following resting times of 5 to 258 min. At many values of resting time, a "high" and "low" value of stress recovered was observed; for examples, at 45 min, 83% and 71% stress recovery was found from shear-rest-shear experiments on the same sample. To analyze the spread in the data,

power law and expanded power law fits were applied to (1) all data points (red curve in Figure 3-5), (2) the "high" data points (blue curve), and (3) the "low" data points (green curve). This created a range of t_{100} values for each sample when the fits were extrapolated to 100% stress recovered: for all data points, t_{100} was 189 mins; for high data points only, the value was 151 min; and for low data points only, t_{100} was 258 min. Overall, for the 5.5 vol. % gel deformed in γ_7 experiments at 23°C shown in Figure 5, the time required for 100% healing of the fractured network ranged from 151 min to 258 min. It is important to note that this extensive range of t_{100} values was not observed in γ_{40} experiments. This "high-low" data analysis was performed for all γ_7 experiments and t_{100} ranges are summarized in Table 3-3 in comparison with γ_{40} experiments.

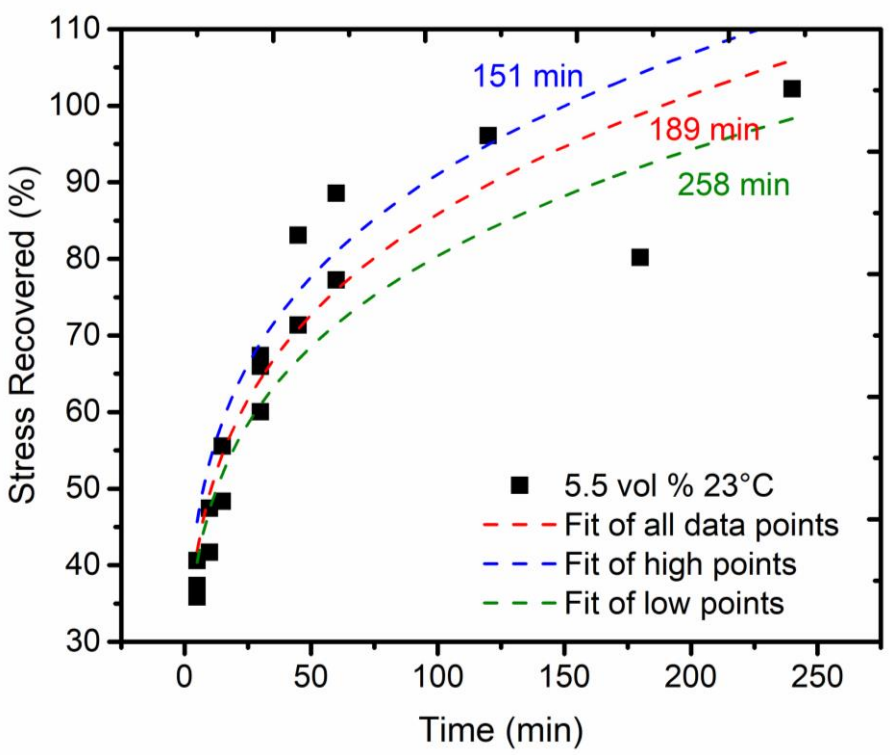

Figure 3-5 Percent of stress recovered versus time data for a 5.5 vol. % gel tested at 23°C with power law fits of high, low and all data points.

In a similar fashion to Figure 3-2A, stress recovery data normalized by τ_c for all γ_7 experiments are presented in Figure 3-6. The best fit lines from Table 3-2 for each gel concentration are added to Figure 3-6 in order to show the qualitative differences in the recovery behavior of γ_7 and γ_{40} experiments. For 5 vol. % gels (Figure 3-6A), the "high-low" spread in the data points encompassed the γ_{40} best fit line, indicating that the γ_7 experiments displayed both faster and slower healing kinetics. For 6 vol. % gels (Figure 3-6C), at most temperatures healing kinetics of the γ_7 experiments were faster than the γ_{40} experiments. The 5.5 vol. % gels displayed intermediate behavior. Similar to the γ_{40} experiments in Figure 3-2A, timescales for complete, 100% stress recovery (i.e., t_{100}) were again found to range from approximately $(10^2\text{-}10^3)$ τ_c.

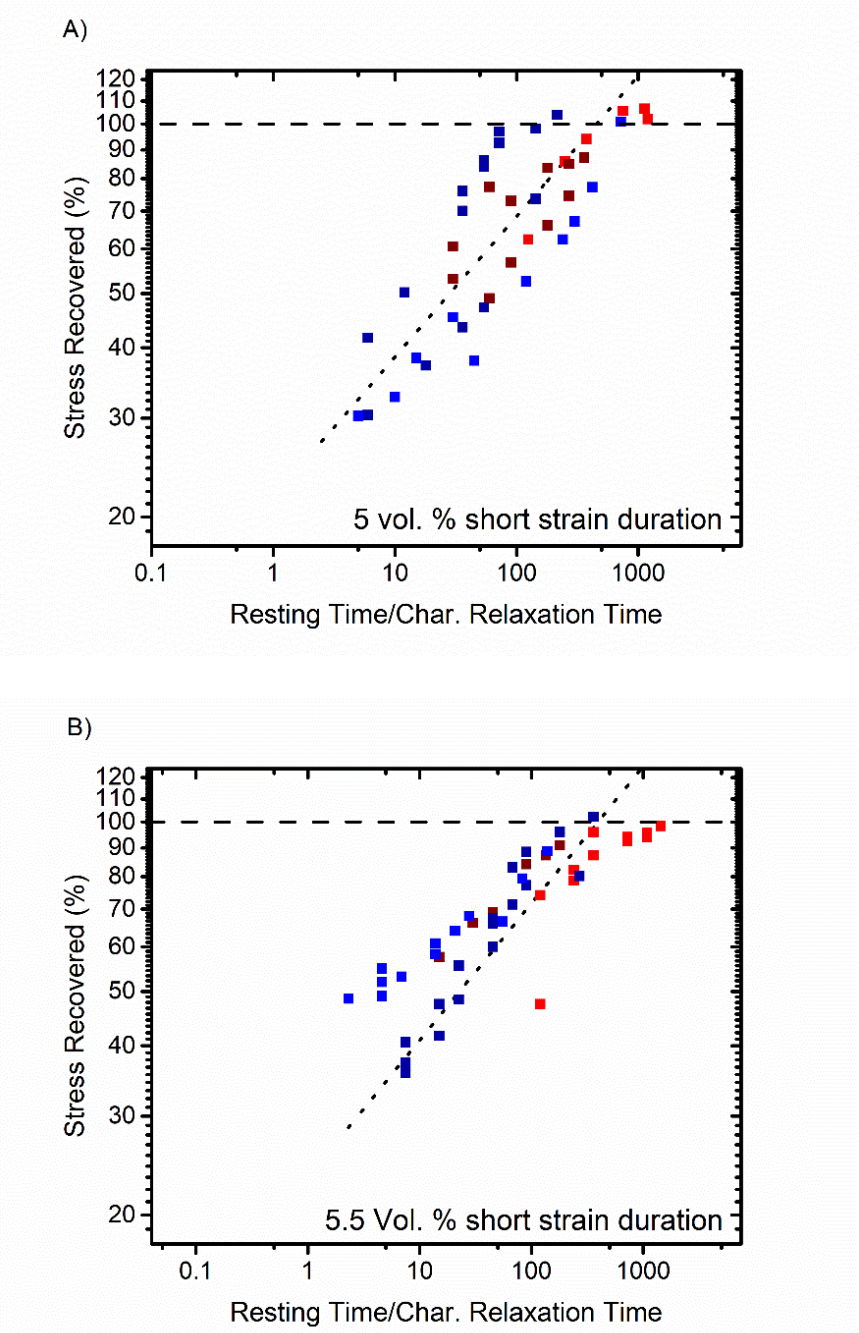

Figure 3-6 Stress recovery data from γ_7 experiments using the same formatting as Figure 3-2A for gel concentrations of (A) 5 vol. %, (B) 5.5 vol. % and (C) 6 vol. %. And temperatures from 20-28°C. Dotted lines are from the best fits reported in Table 3-2 from the γ_{40} data.

Figure 3-6 continued

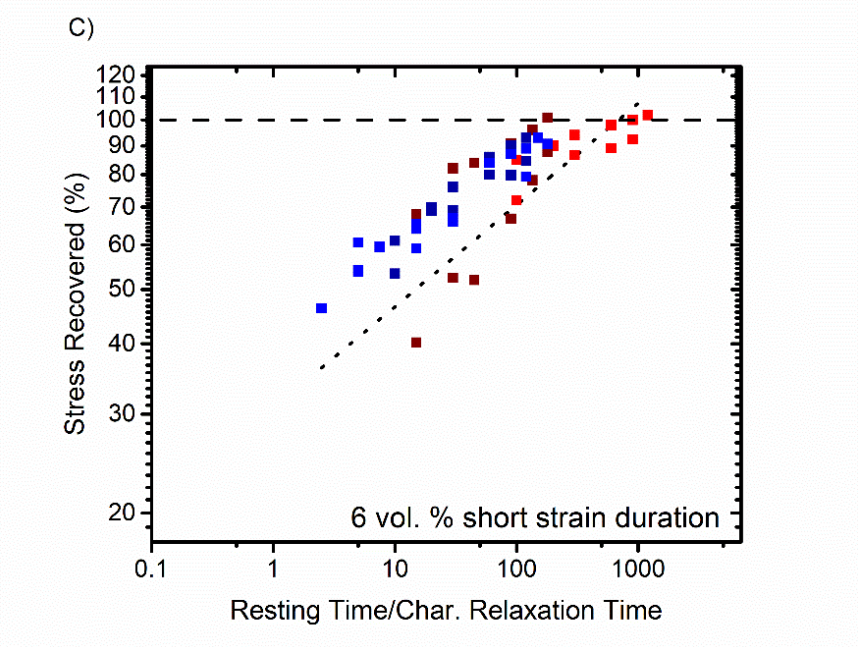

Directly comparing γ_7 to γ_{40} experiments summarized by Table 3-3 and Figure 3-6 indicated that as the gels were sheared to greater strain durations, the healing behavior was affected in a nonmonotonic way. Categorizing the results in terms of temperature and gel concentration, higher-temperature, lower-concentration samples deformed to greater strain (γ_{40}) displayed faster healing responses while lower-temperature, higher-concentration samples displayed faster healing for reduced strain durations (γ_7).

Our starting hypothesis in this study was that by investigating gels at near-fracture strains (i.e., with the γ_7 experiments), healing kinetics would be accelerated due to reduced total damage accumulation within the network as compared to experiments conducted at longer strain durations (i.e., the γ_{40} experiments) where greater total damage may occur, thus requiring more total time for 100% stress recovery. Instead, the data indicated that overall healing kinetics were similar in both cases if characteristic relaxation times were taken into account (i.e., $t_{100} \sim (10^2\text{-}10^3)\ \tau_c$), seemingly independent of the total amount of

damage within the system. However, this simple analysis may be misleading, as the spread in the data from γ_7 experiments was found to be significantly greater than the corresponding γ_{40} experiments, with some samples displaying faster healing behavior and some slower. It may be that the observed "high-low" spread in γ_7 data was due to some samples displaying incomplete or "partial" fracture through the bulk (compared to total fracture through the gel). Intuitively, partial fracture may be more likely to occur for reduced strain duration experiments, where shearing was stopped immediately following the observed stress overshoot (recall Figure 3-3), potentially before the fracture plane was able to fully propagate through the bulk (note: the rheometer is expected to be sensitive to even the onset of fracture in a gel, as explained in more detail in the next section). And such partial fracture may also heal more quickly, resulting in the rapid-recovery "high" data points that were frequently observed in γ_7 experiments.

3.3.3 Investigation of Fracture with Rheophysical Experiments

Before further discussion of the likelihood of partial fracture in the γ_7 experiments, it is instructive to consider the rheophysical results. Velocity profiles from particle image velocimetry measurements of sheared gels have been measured previously and it was found that cohesive fracture occurred when these were deformed above a critical rate.[25] A linear velocity profile indicated deformation in a uniform manner- displaying simple shear with a single velocity gradient (i.e., one shear rate) existing between the moving wall to the stationary wall. When flow instabilities were present (such as fracture or shear banding), the velocity profiles became inhomogeneous and regions of different shear rates were formed. Evidence of midgap (cohesive) fracture events was observed when the velocity profiles were discontinuous, with regions of near-zero (or negative) velocity and regions

of positive velocity of magnitude similar to the velocity of the moving wall. Following most fracture events, a region of negative local velocity was observed due to the elastic recoil of the gel moving in the opposite direction of the applied shear driven by the entropic elasticity of the polymer network.[31]

One of the main limitations of these and other similar rheophysical experiments[28] is that when only one laser-camera system is used, the velocity profile of only a relatively small area of the sheared sample can be investigated. Thus imaging of a flow instability in a system relies on the instability coming into the view of the camera (i.e., the small area of investigation). To verify the occurrence of fracture in our sheared gels (and correlate it with the occurrence of a stress overshoot in the rheometry data), experiments were typically extended to larger values of applied strain in order to ensure the complete propagation of fracture through the bulk system and into the view of our laser-camera assembly. This was always achieved for the y_{40} experiments with the gels; however, for y_7 experiments, these relatively "short" experiments successfully captured the stress overshoot (i.e., the onset of fracture in the gel), but discontinuous velocity profiles were not always directly observed due to potentially incomplete fracture propagation through the bulk of the gel.

Figure 3-7 illustrates the rheological data and velocity profiles of a 5.5 vol. % gel tested at 25°C. The stress overshoot shown in Figure 3-7A occurred at ~ 4 s (strain of 4 units). Using the laser-camera system to collect images of the illuminated tracer particles in the shear gel (every 0.2 s), Images 8-9 (strain of 2) have near-linear velocity, as expected for uniform simple shear behavior. For images 20-21 (strain of 4), where fracture was expected considering the occurrence of the stress overshoot in Figure 3-7A, instead linear velocity profiles were observed. The evidence of fracture did not appear until images 25-

26 at 5.2 s (strain of 5). For these images, characteristic discontinuous velocity profiles were observed including negative values. This pronounced recoil was believed to impact the measured stress response of the gel shown in Figure 3-7A, a post-overshoot decrease and recovery in the data compared with the data in Figure 3-3. As the recoil response was a short-lived phenomenon, the stress response reaches its characteristic steady-state plateau after a few seconds. This delayed observation of fracture (i.e., expected in images 20-21 but not observed until images 25-26) most likely indicated the occurrence of incomplete fracture propagation through the gel; enough elastically active chains were pulled out of their respective junctions to impact the shear stress response, but fracture has not fully propagated through the entire polymer network and into the view of the laser-camera assembly.

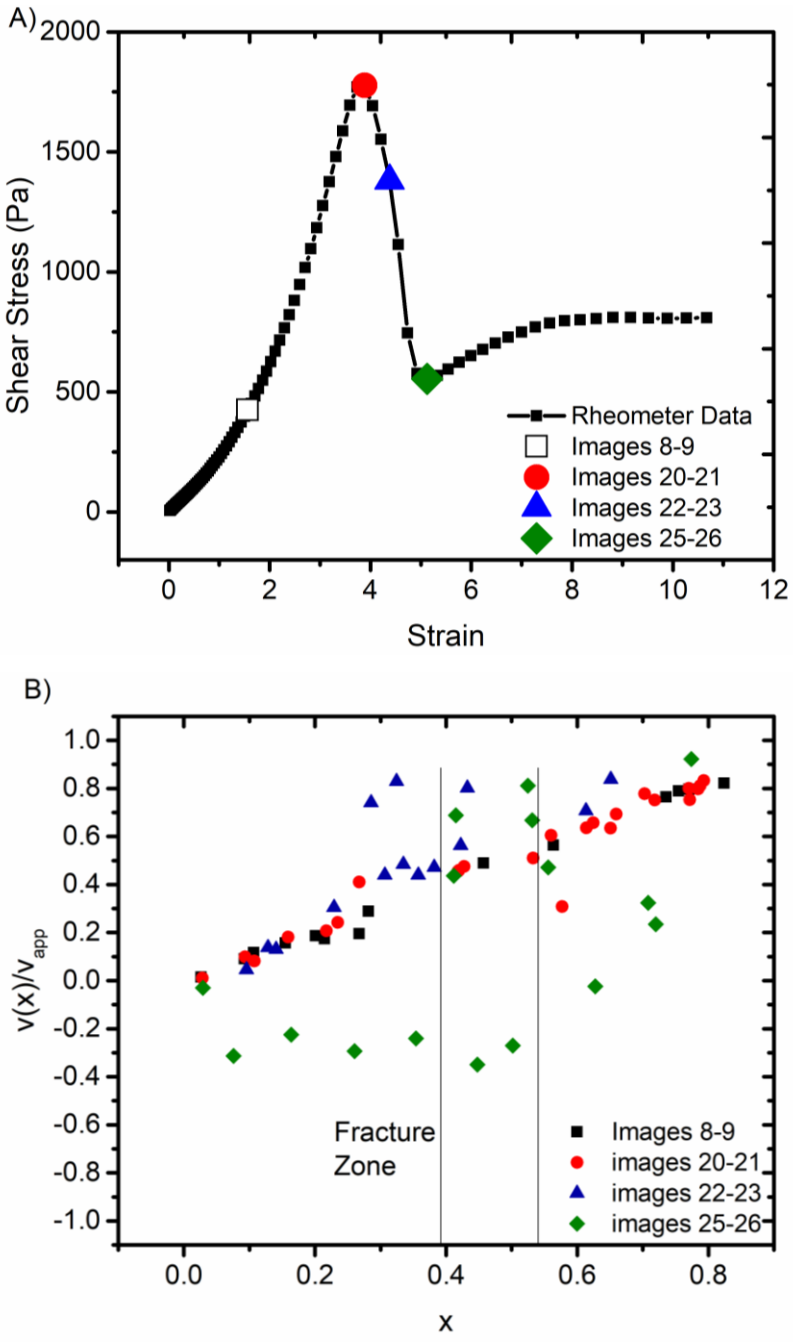

Figure 3-7 (A) Shear rheology data of a 25 °C, 5.5 vol. % gel during a constant shear rate test. (B) Calculated velocity profiles as function of relative distance across experimental gap for various images collected during rheophysical experiments. Vertical y-axis refers to the local velocity (v(x)) normalized with respect to the applied velocity, v_{app} (1.41 mm/s), and the horizontal x-axis (x) is the relative gap location within the experimental gap (1.5 mm), where x=0 is the location of the stationary wall of the cup and x=1 is the location of the moving wall of the rheometer fixture.

3.3.4 Effect of Network Structure and Properties on Healing Behavior

The 28°C data for the different experimental parameters indicated a change in the healing times of the gel. For the γ_{40} experiments, gels quickly healed and were able, in some cases, to exceed the maximum strength of the primary fracture response. As the strain duration was decreased in γ_7 experiments, the time for gels to heal at 28°C increased. The accelerated kinetics of the γ_{40} experiments were believed to be due to local viscous heating within the sheared gel in the vicinity of the fracture zone.[32] With its critical temperature of 34°C, the gel was a relatively weak and highly transient network at 28°C. By having the rheometer fixture at the fixed gap of 1 mm rotating at the constant applied shear rate to a total strain of 40 units, the friction[24] within the fracture zone could lead to local increases in temperature by 1 or 2 °C. Once the experiment is halted, the thermal energy could disperse evenly through the sample to eliminate any temperature gradients. This localized heating could cause the network to become very dynamic and act more similar to a polymer solution. Testing the gels at shorter times and lower total strain duration, as with the y_7 experiments, would effectively minimize the effects of friction-induced heating.

Aggregation number and junction size could also influence the healing mechanism and timescales. Previously reported small-angle x-ray scattering (SAXS) data on gel concentrations above 10 vol. %[27] showed that aggregation number increased from 60 to 80 chains per junction for increasing concentrations from 10 to 30 vol. %. SAXS results for lower concentration gels were unobtainable due to weak scattering though based on the experimental trends, it is likely that the aggregation number was 40-50 chains per junction in the static (unsheared) state for the gel concentrations investigated here of 5-6 vol. %. It is unclear from experiments exactly how the “dangling”, unassociated polymer chains

reform into elastically active network strands during the resting period following shear-induced fracture; healing could occur by either dangling chains re-inserting into their original junction or perhaps forming new junctions of different size.

Simulations of telechelic polymers[33–35] that exhibit shear banding flow instabilities have shown that aggregation number can change during deformation. This could be due to the creation of dangling chains that are unable to reinsert into endgroup junctions. During high shear rates, more junctions are formed containing endblocks from the same polymer, forming loops and causing a range of junction sizes to be observed. From simulated oscillatory measurements, restructured networks with increased number of junctions were found to be stronger than the initial network. Small frequency oscillations of the system caused dangling chains to re-enter into existing junctions. Applying these conclusions to our work, a range of junction sizes could accelerate healing kinetics following shear-induced fracture and regain its strength by allowing dangling chains from fractured junctions to reinsert themselves into an existing junction.

Strength of the gel was dependent on temperature as described in Figure 3-8. As temperature decreased, the gel became more elastic and strain stiffen.[26] For the highest temperature of this study, 28°C, the gel was near the critical temperature and the network was more viscous and dynamic. As the temperature was decreased, the network becomes more rigid and the endblock junctions were more tightly packed as the increasingly poor solvent was expelled from the PMMA endblocks.[36] The stiffer network structure exhibited higher shear stress maxima.

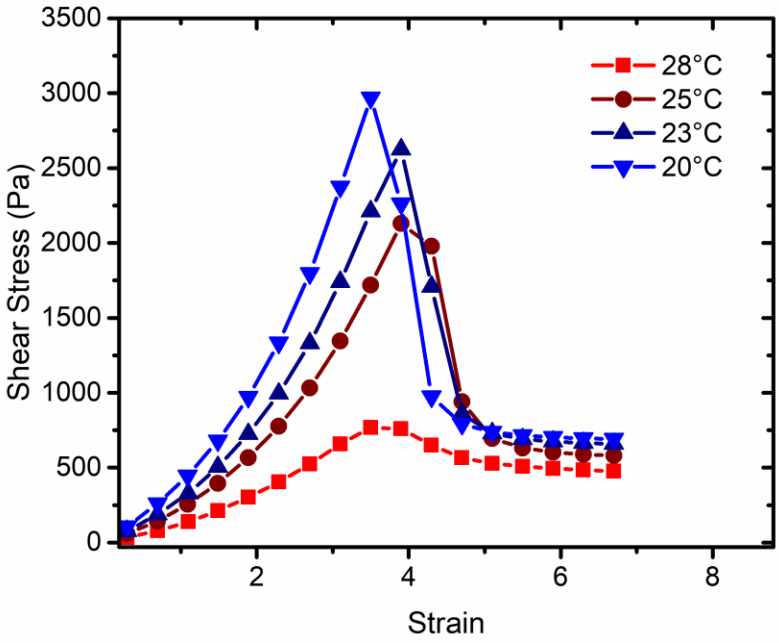

Figure 3-8 Stress-strain curves of 5.5 vol. % gels at various temperatures ranging from 28-20°C

The temperature dependence of network strength can also be seen from the G(0) values in Table 3-1. Gel strength increased with increasing concentration and decreasing temperature, and there exists a general correlation between t_{100} and G(0) values. For gels with G(0) < ~300 Pa (i.e., 5 vol. % gels at all temperatures and high temperature tests of 5.5 vol. % gels), t_{100} values from the γ_{40} experiments were found to be smaller than t_{100} values from the γ_7 experiments due to possible viscous heating of the system. As illustrated and described earlier in Figure 3-6, stress recovery data displayed a "high-low" spread of healing behaviors for γ_7 experiments, believed to be due to some systems only partially fracturing when exposed to these relatively shorter applied strain durations and able to then display accelerated healing. Interestingly, reduced t_{100} values of γ_7 experiments were observed when G(0) > 300 Pa (i.e., gels at lower temperatures of 5.5 vol. % and 6 vol. %).

This may indicate that partial fracture of the stiffer gels may lead to faster healing of the gels.

3.4 Conclusions

We have investigated the effect of deformation magnitude on the fracture-healing kinetics of model acrylic triblock copolymer gels at various concentrations (5-6 vol. %) and temperatures (20-28°C) using shear rheophysical experiments. By changing the total strain applied to the system (700 vs. 4000% applied strain) and varying the post-fracture resting times, variations in the strength recovery of the gels were measured.

- A gel can fully heal given sufficient post-fracture resting time, and healing kinetics can be accelerated by increasing the temperature of the system.
- Complete, post-fracture strength recovery occurred within timescales that were 2-3 orders of magnitude greater than the characteristic relaxation times of the gels.
- For 5 vol. % gels tested at all temperatures and 5.5 and 6 vol. % gels tested at high temperatures, healing kinetics were believed to be accelerated by local viscous heating within the system during the 4000% applied strain experiments.
- For the 700% applied strain experiments, 5.5 vol. % gels tested at lower temperatures and 6 vol. % tested at all temperatures required relatively shorter resting times to obtain a completely healed network due to the probable occurrence of partial or incomplete fracture propagation.
- Rheophysical experiments indicated a delay in visual observation of complete fracture following the measured stress overshoot, and this delay was more likely for 700% applied strain experiments, providing further evidence of partial fracture.

3.5 References

(1) Naderi, H.; Matin, M. M.; Bahrami, A. R. *J. Biomater. Appl.* **2011**, *26* (4), 383–417.

(2) Gujrati, V.; Kim, S.; Kim, S. H.; Min, J. J.; Choy, H. E.; Kim, S. C.; Jon, S. *ACS Nano* **2014**, *8* (2), 1525–1537.

(3) Van Hove, A. H.; G. Beltejar, M.-J.; Benoit, D. S. W. *Biomaterials* **2014**, *35* (36), 9719–9730.

(4) Aguado, B. A.; Mulyasasmita, W.; Su, J.; Lampe, K. J.; Heilshorn, S. C. *Tissue Eng. Part A* **2012**, *18* (7–8), 806–815.

(5) Brochu, A. B. W.; Chyan, W. J.; Reichert, W. M. *J. Biomed. Mater. Res. Part B Appl. Biomater.* **2012**, *100B* (7), 1764–1772.

(6) Wertzberger, B. E.; Steere, J. T.; Pfeifer, R. M.; Nensel, M. A.; Latta, M. A.; Gross, S. M. *J. Appl. Polym. Sci.* **2010**, *118* (1), 428–434.

(7) Scheltjens, G.; Diaz, M. M.; Brancart, J.; Van Assche, G.; Van Mele, B. *React. Funct. Polym.* **2013**, *73* (2), 413–420.

(8) Hart, K. R.; Sottos, N. R.; White, S. R. *Polymer* **2015**, *67*, 174–184.

(9) Ahn, S.; Kasi, R. M.; Kim, S.-C.; Sharma, N.; Zhou, Y. *Soft Matter* **2008**, *4* (6), 1151.

(10) Patenaude, M.; Smeets, N. M. B.; Hoare, T. *Macromol. Rapid Commun.* **2014**, *35* (6), 598–617.

(11) Lee, Y.; Chung, H. J.; Yeo, S.; Ahn, C.-H.; Lee, H.; Messersmith, P. B.; Park, T. G. *Soft Matter* **2010**, *6* (5), 977.

(12) Chiu, Y.-L.; Chen, S.-C.; Su, C.-J.; Hsiao, C.-W.; Chen, Y.-M.; Chen, H.-L.; Sung, H.-W. *Biomaterials* **2009**, *30* (28), 4877–4888.

(13) Appel, E. A.; Tibbitt, M. W.; Webber, M. J.; Mattix, B. A.; Veiseh, O.; Langer, R. *Nat. Commun.* **2015**, *6*, 6295.

(14) Long, R.; Mayumi, K.; Creton, C.; Narita, T.; Hui, C. *Macromolecules* **2014**, *47*, 7243–7250.

(15) Sun, T. L.; Kurokawa, T.; Kuroda, S.; Ihsan, A. Bin; Akasaki, T.; Sato, K.; Haque, M. A.; Nakajima, T.; Gong, J. P. *Nat. Mater.* **2013**, *12* (10), 932–937.

(16) Gong, J. P.; Katsuyama, Y.; Kurokawa, T.; Osada, Y. *Adv. Mater.* **2003**, *15* (14), 1155–1158.

(17) Sathaye, S.; Mbi, A.; Sonmez, C.; Chen, Y.; Blair, D. L.; Schneider, J. P.; Pochan, D. J. *Wiley Interdiscip. Rev. Nanomedicine Nanobiotechnology* **2015**, *7* (1), 34–68.

(18) Rossow, T.; Habicht, A.; Seiffert, S. *Macromolecules* **2014**, *47* (18), 6473–6482.

(19) Skrzeszewska, P. J.; Sprakel, J.; de Wolf, F. A.; Fokkink, R.; Cohen Stuart, M. A.; van der Gucht, J. *Macromolecules* **2010**, *43* (7), 3542–3548.

(20) Gerth, M.; Bohdan, M.; Fokkink, R.; Voets, I.; van der Gucht, J.; Sprakel, J. *Macromol. Rapid Commun.* **2014**, *35* (24), 2065–2070.

(21) Normand, V.; Muller, S.; Ravey, J. C.; Parker, A. *Macromolecules* **2000**, *33* (3), 1063–1071.

(22) Sarvestani, A. S.; He, X.; Jabbari, E. *Biomacromolecules* **2007**, *8* (2), 406–415.

(23) Yan, C.; Altunbas, A.; Yucel, T.; Nagarkar, R. P.; Schneider, J. P.; Pochan, D. J. *Soft Matter* **2010**, *6* (20), 5143–5156.

(24) Erk, K. A.; Martin, J. D.; Hu, Y. T.; Shull, K. R. *Langmuir* **2012**, *28* (9), 4472–4478.

(25) Thornell, T. L.; Helfrecht, B. A.; Mullen, S. A.; Bawiskar, A.; Erk, K. A. *ACS Macro Lett.* **2014**, *3* (10), 1069–1073.

(26) Erk, K. A.; Shull, K. R. *Macromolecules* **2011**, *44* (4), 932–939.

(27) Seitz, M. E.; Burghardt, W. R.; Faber, K. T.; Shull, K. R. *Macromolecules* **2007**, *40* (4), 1218–1226.

(28) Hu, Y. T.; Lips, A. *J. Rheol.* **2005**, *49* (5), 1001.

(29) Bawiskar, A. Shear Rheological Characterization of Gel Healing Response and Construction of Rheo-PIV System, Purdue University, 2014, Vol. 1.

(30) Brevis, W.; Niño, Y.; Jirka, G. H. *Exp. Fluids* **2011**, *50* (1), 135–147.

(31) Rubinstein, M.; Colby, R. H. *Polymer physics*; Oxford University Press, 2003.

(32) White, J. M.; Muller, S. J. *J. Rheol.* **2003**, *47* (6), 1467.

(33) Billen, J.; Wilson, M.; Baljon, A. R. C. *Chem. Phys.* **2015**, *446*, 7–12.

(34) Wilson, M.; Rabinovitch, A.; Baljon, A. R. C. *Macromolecules* **2015**, *48* (17), 6313–6320.

(35) Li, S.; Chen, J.; Xu, D.; Shi, T. *J. Chem. Phys.* **2015**, *143* (24), 244902.

(36) Drzal, P. L.; Shull, K. R. *Macromolecules* **2003**, *36* (6), 2000–2008.

CHAPTER 4. SYNTHESIS OF SPHERICAL COMPOSITE HYDROGELS FOR USE IN HIGH PERFORMANCE CONCRETE

4.1 Introduction

In order to create complex structural forms, researchers are developing materials based off of high performance concrete (HPC). HPC aims to decrease the amount of water in batch mixing by changing the water-to-cement ratio (w/c). Conventional concrete mixes use a w/c of 0.42 for a completely hydrated concrete, but for HPC the w/c is reduced to 0.3-0.35 to create a denser microstructure.[1,2] The final products of HPC designs exhibit better mechanical properties and durability from conventional concrete due to the increase in solids content, such as Portland cement creating a denser microstructure with less porosity.

However, the decrease in water available during mixing creates several problems. With less water available for curing, incomplete hydration and curing of Portland cement can occur. The incomplete curing of HPC materials displays large amounts of volumetric (autogenous) shrinkage and self-desiccation that result in high porosity and cracking, leading to reduction in strength and durability.[3,4]

To overcome those disadvantages, internal curing agents and supplementary materials have been added to HPC mixes. The internal curing agents provide a source of water to help drive curing in the bulk of the material. Water-saturated lightweight aggregates[5,6] and fly ash[7] have been used to help deliver water to the bulk of the concrete, but require some type of presoaking. Supplementary material such as silica fume have been introduced to provide more components to create more essential hydrated concrete

products.[8,9] The supplementary materials are usually pozzolans that have high silica content that can react with calcium hydroxide ($Ca(OH)_2$) to form calcium silicate hydrate, a phase that gives concrete its high compressive strength.[10]

Superabsorbent polymer hydrogels are an ideal material to use as internal curing agents since they do not need to be presoaked, can be added dry during mixing, and only a small amount needs to be added to see benefits (0.2-0.5 wt. % by cement).[11] These hydrogels are three dimensional networks that have high swelling capacities that arise from osmotic pressure differences inside the gel and outside. The swollen gels composed of hydrophilic polymers and polyelectrolytes are able to release the water that is trapped in the network and drive the curing to proceed. Currently, researchers rely on commercially available poly(acrylic acid)-based hydrogels where little is known about the chemical and physical structure.[12]

In previous research from Erk and coworkers,[13–15] polymer composition relationships were studied for irregularly shaped gels. Polymer hydrogels composition of acrylic acid (AA) and acrylamide (AM) were varied to form random copolymers from free radical polymerization that contained 83% AA to 100 % AM. It was shown that higher AA content with high amount of ionic side chains had the highest swelling capacity in pure water, but swelling decreased rapidly when in the presence of ions (monovalent (Na^+) and multivalent (Ca^{2+}, Al^{+3})). The multivalent ions such as Ca^{2+} and Al^{3+} are able to bind with the carboxylic side chains of AA and restrict the network. As the amount of AA was decreased and AM increased, the swelling behavior was less affected by ionic interactions and had overall lower swelling capacities.

The effects of these hydrogels in concrete did have positive impacts.[13-15] For autogenous shrinkage of mortar samples, the degree of linear shrinkage was greatly reduced for each composition against the control sample containing no hydrogel. Concrete microstructural analysis uncovered that polymer gel did deswell and leave voids, but with the release of water within the hydrogel, hydrated products, such as $Ca(OH)_2$, did grow into and fill that void space to some degree.

The effects of varying geometry from irregular shapes to spherical particles have also been studied.[16,17] Particle size and composition were varied to determine swelling performance and mechanical properties. Particle size was shown to decrease as mixing speed was increased from 400 to 1200 rpm. The swelling behavior of the gels was studied by gravimetric swelling tests, optical microscopy, and laser diffraction. Spherical particles had even better results in limiting autogenous shrinkage as compared to irregular shaped hydrogels. Compressive mechanical tests on concrete mortar showed no appreciable decrease in strength for hydrogel samples even though microscale voids were present in the samples.

The morphological differences between angular and spherical hydrogels are directly related to the synthesis procedure. For irregularly shaped particles, the synthesis is a free radical solution polymerization that proceeds quickly and the chemical gel takes the form of the reaction vessel. The hydrogel is then processed in several steps from large gel pieces (several mm's) and ground into a fine powder (tens of μm's).

For spherical particles, inverse suspension polymerization is a facile way to attain particles with that desired morphology. Traditional suspension polymerization uses a dispersed oil (organic) phase and a continuous aqueous phase with added surfactant to

create droplets.[18] Within the droplets or micelles, oil soluble monomer, initiator, and crosslinker can polymerize into gels. For inverse suspension polymerization, the phases are reversed where the aqueous phase is now dispersed within a continuous oil phase. For polymer hydrogels, the monomers are water-soluble, so this polymerization method can be utilized to create polymers based on AA and AM.[19,20] The particle size can be controlled by stirring speed and concentration of surfactant.

Building upon the previous work of polymer composition and particle shape, this work will investigate the synthesis of spherical polymer hydrogel particles with incorporation of pozzolanic silica nanoparticles to create spherical composite hydrogels. It has been proven that both hydrogels as internal curing agents and the use of silica-based materials have an impact on HPC. By combining both of these strategies into one material, a new novel chemical admixture for HPC mixes can be developed and studied.

Polymer hydrogels containing silica nanoparticles have previously been studied for a variety of different applications. Zhang and coworkers developed polyacrylamide and silica hydrogels from inverse Pickering emulsions for removing heavy metal ions from wastewater.[21] The Pickering emulsion approach did not require a use of any surfactant as the high loading of SiO_2 nanoparticles were able to self-assemble at the oil-water interface to create monomer droplets. Any excess SiO_2 particles after reaching a saturation limit remained in the continuous organic phase. Yoon and coworkers synthesized composite hydrogels with cationic polyacrylamide for use in papermaking processes.[22] They were able to achieve composite hydrogels by using a mixture of two surfactants to create a stable suspension with SiO_2 dispersed throughout the gel network.

This work investigated the synthesis routes of polyacrylamide (PAM) and poly (acrylic acid) (PAA) composite hydrogels. The incorporation of SiO_2 was performed using bare nanoparticles and functionalized nanoparticles. The functionalization of the silica with an acrylic-based silane was studied using infrared spectroscopy and thermogravimetric analysis (TGA). From this data, grafting yield was calculated to determine coverage of silane on the surface of SiO_2 nanoparticles. The hydrogels synthesized from inverse suspension polymerization were characterized using optical microscopy, scanning electron microscopy, TGA, and gravimetric swelling. Microstructure analysis of composite hydrogels in cement paste were performed to determine differences between hydrogel cement pastes with and without SiO_2.

4.2 Materials and Methods

4.2.1 Materials

Silica nanoparticles (SiO_2) (Organosilicasol MT-ST 30 wt % colloidal silica in methanol, Nissan Chemical Co) with average diameter of 15 nm were used and dried powder was obtained after precipitating into toluene and centrifuging. Cyclohexane, acrylamide (AM), N,N'-methylenebisacrylamide (MBAM), sodium persulfate ($Na_2S_2O_8$), N,N,N',N'-tetramethylethylenediamine (TMED), Span-80, Ludox HS-40 colloidal silica, and 3-(Trimethoxysilyl)propyl methacrylate (all from Sigma-Aldrich) were used as received. Acrylic acid (AA) (Sigma-Aldrich) was purified using an inhibitor-removing column drop-wise and purified AA was stored refrigerated. Sodium hydroxide (NaOH) (Macron) solutions of 9.8 M (15.72 g in 40 mL water) were used to neutralize AA. Type I Portland cement (Buzzi Unicem USA) was used as received with previously reported

chemical composition.[14] Glenium 3030 NS water reducing admixture (WRA) from BASF was used as received

4.2.2 Silica Functionalization

Functionalized SiO_2 were synthesized from dried particles from Nissan Chemical to create covalent bonds to react into the hydrogel network. SiO_2 particles (1 g) were add to a 5 vol. % solution of hydrochloric acid and water and mixed for at least 1 hour to create hydroxyl (-OH) bonds on the surface of SiO_2. The particles were centrifuged at 4000 RPM for 30 min three times in water. Dried particles were vacuum dried at room temperature.

The dried particles (0.5 g) were then dispersed in 20 mL of anhydrous toluene. Ultrasonication was used to disperse the SiO_2 with 2 cycles of 35% and 40% amplitudes each for 2 minutes per cycle. The dispersed solution was transferred to a 50 mL round-bottom flask. Anhydrous toluene (5 mL) was added to collect any residual particles left in the scintillation vial. The round-bottom flask was heated to 40°C in an oil bath. After 30 minutes, 0.2 mL silane agent (3-(Trimethoxysilyl)propyl methacrylate shown in Figure 4-1) was added and the reaction was allowed to proceed overnight (18 hours). The methoxysilyl groups allowed for attachment to the SiO_2 particles and polymerization occurring through the methacrylate C=C double bond The mixture was centrifuged at 4000 RPM for 30 min for 3 cycles each of toluene and then 3 cycles of water. Obtained particles were dried under vacuum at room temperature.

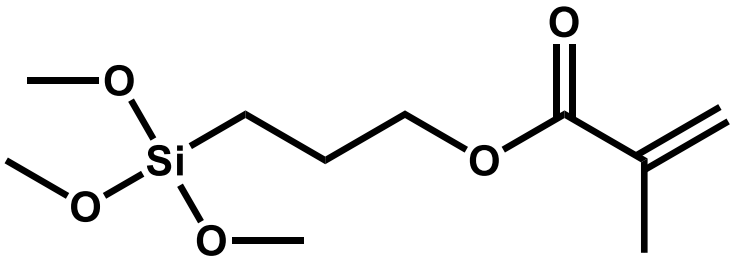

Figure 4-1 Structure of 3-(Trimethoxysilyl)propyl methacrylate

4.2.3 Composite Hydrogel Synthesis

A general procedure of synthesizing composite hydrogels from inverse suspension polymerization is as follows. Crosslinking was set at 2 wt % by monomer and SiO_2 loadings were varied at 1 and 5 wt % by monomer. The organic phase was composed of 225 mL of cyclohexane and 0.75 g of Span-80 surfactant first mixed in a 250 mL Erlenmeyer flask and then transferred to a 250 mL flat bottom extraction flask with an overhead stirrer set to 500 RPM. The flask and stirrer were secured to a hot plate and a nitrogen purge line was attached.

Table 4-1 Weights and volumes of aqueous phase reactants

Sample	%SiO_2	AM (g)	AA (mL)	SiO_2 (g)	MBAM (g)	Water (mL)	NaOH (mL)	TMED (mL)
PAM	0	2.4	0	0	0.05	12	0	1.3
	1	2.4	0	0.024	0.05	12	0	1.3
	5	2.4	0	0.12	0.05	12	0	1.3
83% PAA	0	0.4	2	0	0.05	8.8	3.2	1.3
	1	0.4	2	0.024	0.05	8.8	3.2	1.3
	5	0.4	2	0.12	0.05	8.8	3.2	1.3

The aqueous solution was prepared in a scintillation vial. Table 4-1 summarizes the weights and volumes for the aqueous phase of each sample synthesized. Water was added and then SiO_2 particles were added slowly while stirring. Ultrasonication was used to disperse the particles using 2 cycles each at 30% and 40 % amplitudes at 30 sec intervals. AA monomer was added dropwise and then followed by NaOH solution while stirring. The solution was allowed to cool for 10 min. AM monomer and MBAM crosslinker were added slowly and the vial was allowed to stir for 10 min. Sodium persulfate solution (1 mL) prepared from 2.65 g of $Na_2S_2O_8$ in 10 mL of deionized water. The vial was then transferred to the reaction flask. The reaction mixture was allowed to stir at room temperature for 2 hours. TMED (1.3 mL) was then added and the flask was heated to 65°C. The reaction was allowed to proceed for 4 hours before stirring was halted.

Gel particles were recovered by vacuum filtration and rinsing with ethanol and acetone. The powders were allowed to dry at ambient conditions overnight. The powders were then placed in 700 mL of deionized (DI) water while stirring to remove any residual monomer, initiator, or surfactant. The swollen gel particles would settle to the bottom of the beaker and wash water would be decanted. Fresh DI water was then added back and

the gel would be stirred again. This process was repeated three times. The swollen gels were collected and dried at ambient conditions.

4.2.4 Gravimetric Swelling

Swelling behavior was characterized using gravimetric tea bag method. For each gel sample, 0.1 grams of dried gel particles were loaded into pre-wetted nylon filter bags and submerged in 250 mL of reverse osmosis water. Bags were weighed at set time intervals of 1, 5, 10, 15, 30, 45, 60, 120, and 180 minutes and performed in triplicate. Equation 4.1 was used to determine the swelling ratio (Q) over time for each gel sample

$$Q=\frac{m_{wet}-m_{dry}-m_{bag}}{m_{dry}}, \tag{4.1}$$

where m_{wet} is the mass of the wet bag and hydrated polymer, m_{dry} is the dry polymer mass, and m_{bag} is the mass of the empty bag when wet.

4.2.5 FTIR

The functionalization of SiO_2 particles was studied using a Spectrum 100 Fourier Transfer-Infrared (FTIR) spectrometer (Perkin Elmer) in attenuated total reflectance (ATR) mode. Spectra of bare and functionalized SiO_2 were collected at 5 scans from 4000- 600 cm^{-1} at resolutions of 4 cm^{-1}.

4.2.6 Optical Microscopy

Dry particle images were obtained using an Olympus BX51 system microscope with PAXcam imaging software. Images were collected at 50x and 100x magnifications. Particle size measurements were conducted using ImageJ and approximately 40 particle sizes were measured.

4.2.7 Cement Paste Preparation

Hydrogel-cement mixtures were created to determine composite hydrogel effects on cement microstructures. Paste samples with w/c of 0.35 were composed of Portland cement, WRA, tap water, and composite hydrogels. Portland cement (50 g) and gel (0.1 g (0.2 wt. % by cement)) were mixed dry and then 17.35 g of tap water and 0.35 mL of WRA were added. Components were mixed by hand for two periods of 60 sec. with a rest for 30 sec. and then added to the cylindrical molds. Samples were allowed to cure for 4 days in sealed conditions. Cured samples were then placed into methanol baths to prevent further curing of the cement. Samples were then dried, and cut into pieces for microstructure evaluation.

4.2.8 Scanning Electron Microscopy

Gel particle morphology and hydrogel-cement microstructures were obtained using a Phenom ProX Desktop scanning electron microscope (NanoScience Instruments). Dried composite hydrogels were mounted on carbon tape and imaged without sputtering. Cement paste micrographs were obtained from samples mounted in epoxy discs.

4.3 Results and Discussion

4.3.1 Addition of Bare Silica

The first attempts at composite hydrogel synthesis were performed by addition of bare Nissan Chemical SiO_2 dispersed in the aqueous phase. When the aqueous phase was combined with the stirring continuous cyclohexane phase, the water-in-oil (W/O) suspension became opaque and large phase separation could be observed. Once the accelerator, TMED, was added, the polymerization happened rapidly within 25 sec., and

the gel particles were formed. The polymerized gels, swollen in the aqueous phase, then settled to the bottom of the flask. The reactions were allowed to proceed for 4 hours before being filtered. For all loadings of SiO_2 in PAM and 83% PAA, large “rock”-like particles of fused SAPs were obtained. Samples without SiO_2 were able to produce fine dried powders.

The gel morphology of 5 wt. % bare SiO_2 in PAM hydrogel are shown in Figure 4-2. There was evidence of spherical character but the particles were fused together into large clusters. Aggregation of SiO_2 nanoparticles was also observed on the surface of these particles. These hydrogels could be crushed and processed similar to the angular particles studied by Krafcik, *et. al*,[14] but the ideal goal of this project was to achieve spherical particles with SiO_2 incorporated into the network.

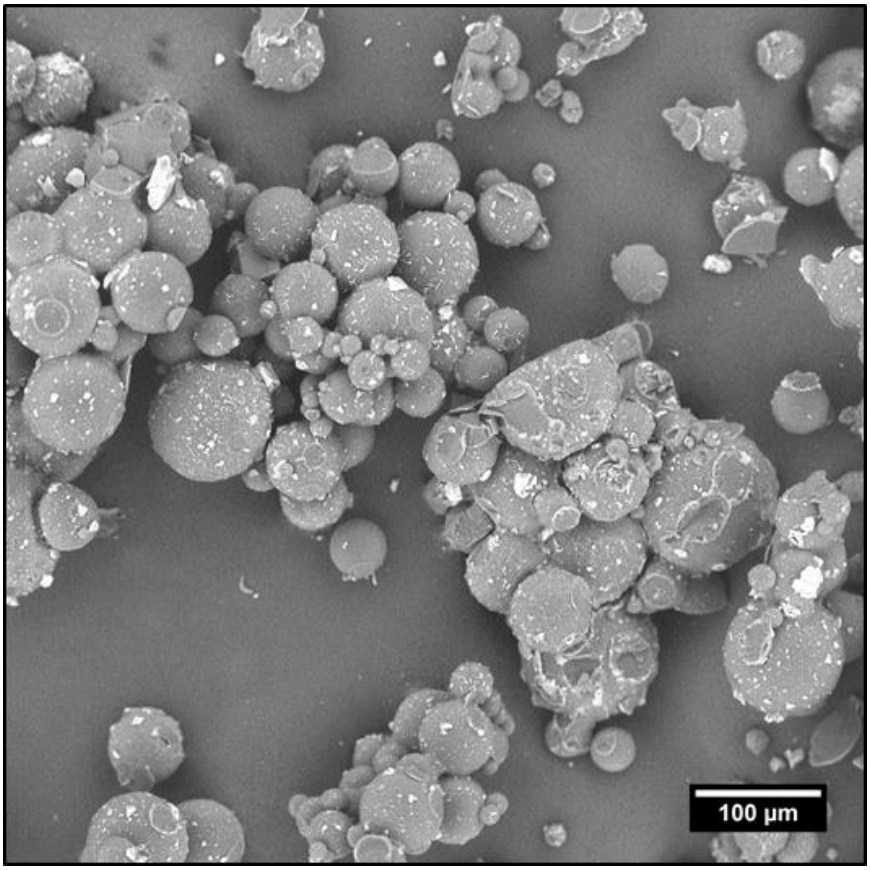

Figure 4-2 SEM micrograph of 5 wt. % bare SiO_2 in PAM hydrogel

To study the effects of aggregation and dispersion, composite hydrogels were attempted using Ludox solutions. These solutions were supplied as 40 wt. % SiO_2 dispersed in water with similar particle size as Nissan Chemical SiO_2. The colloidal suspensions were diluted to the targeted SiO_2 loading of 5 wt. % and mixed into the aqueous phase. Similar to the addition of dry bare SiO_2, the reaction happened rapidly and the gel particles agglomerated at the bottom of the flask during stirring. Figure 4-3 illustrates the 5 wt. % SiO_2 in 83% PAA hydrogels. The reaction proceeded without any control and resulted in spherical particles fused together by an irregular shaped polymer matrix. This dispersed Ludox solution and neither was approaches using dried particles from Nissan Chemical were not able to create spherical particle in this approach.

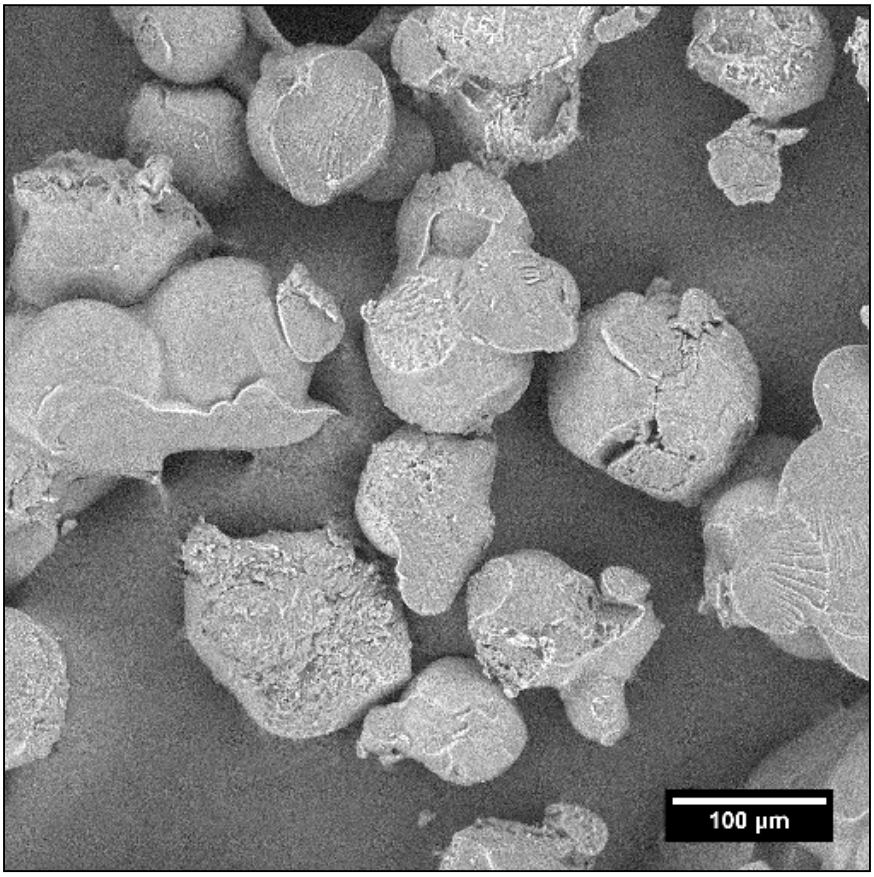

Figure 4-3 SEM micrograph of 5 wt. % SiO_2 from Ludox solutions in 83% PAA hydrogels

The addition of bare SiO_2 nanoparticles to the SAP synthesis method did not produce the ideal spherical composite hydrogel. Stabilization of the aqueous phase and resulting polymer spheres was not attained as those achieved from Pickering emulsions. Pickering emulsions refer to emulsions that are stabilized from solid particles as opposed to those from surfactants.[23] For this system, a competition between the surfactant (Span-80) and SiO_2 existed between which species could adsorb to the oil-water interface. Span-80 has a low hydrophilic-lipophilic balance (HLB) value of 4.3 which makes it a good surfactant for W/O emulsions and suspensions.[24] Bare SiO_2 is hydrophilic and is suitable for Pickering oil-in-water (O/W) emulsions.[25] These competing characteristics caused the

uncontrolled polymerization and irregular particle formation. The surfactant was mixed in the oil phase while the SiO_2 was present in the aqueous phase. When the aqueous phase was added to the continuous oil phase, Span-80 and SiO_2 move toward the oil-water interface. Since the continuous phase of cyclohexane was 95% of the total volume and Span-80 was in greater excess to SiO_2, the suspension did not experience phase inversion, but was not stable. The resulting polymerized gel particles coalesced and settled out of the oil phase.

4.3.2 Functionalization of Silica

To create stable inverse suspension polymerizations, functionalization of the SiO_2 was attempted to make the nanoparticles more hydrophobic and be able to react into the network. The functionalized SiO_2 particles are created from the addition of 3-(trimethoxysilyl)propyl methacrylate with reactive methoxysilane groups that attach to the surface of the SiO_2 nanoparticles. The siliane molecule is an acrylate-based molecule that can participate as a monomer in the polymerization and act as a further crosslinking site.

The collected ATR-FTIR spectrum of bare and functionalized silica are shown in Figure 4-4. Samples were kept under vacuum before testing. The large peak near 1074 cm^{-1} and 795 cm^{-1} indicated to be Si-O-Si bonding[21] for both SiO_2 samples. For the SiO_2 samples functionalized with the vinyl silane compound, the peaks at 1707 cm^{-1} and 1630 cm^{-1} were attributed to C=O and C=C, respectively. [26] The slight peaks indicated a low surface coverage of the silane during functionalization.

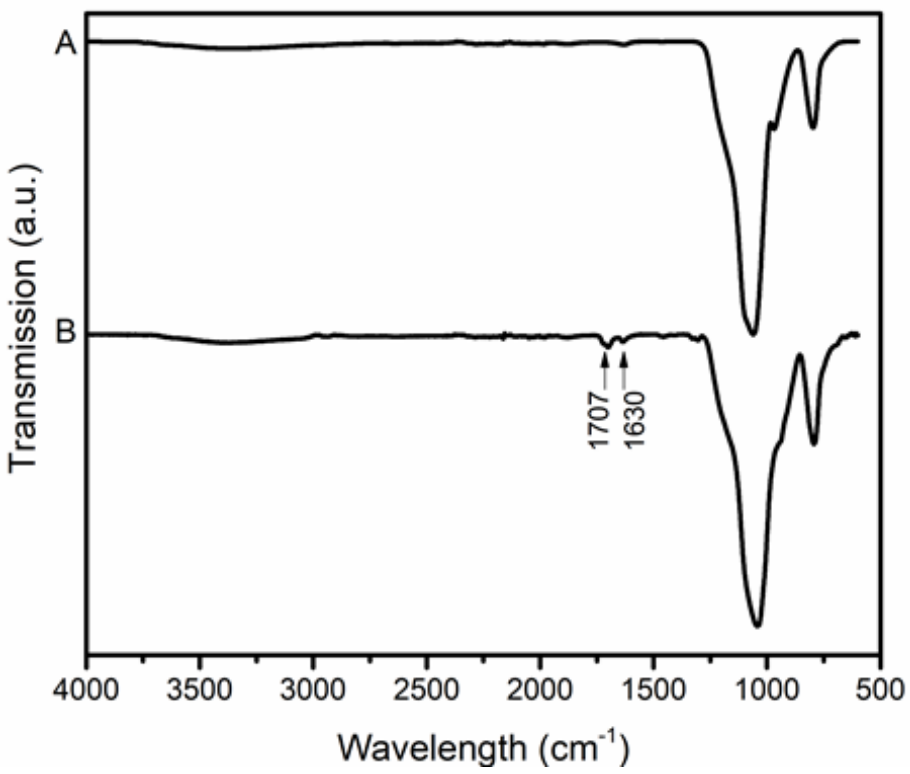

Figure 4-4 FTIR spectra of A) bare SiO_2 and B) silane-functionalized SiO_2

TGA curves for bare SiO_2 and silane-functionalized SiO_2 in inert nitrogen atmosphere are shown in Figure 4-5. The bare SiO_2 sample displayed a 2.64 % weight loss. For the silane-functionalized SiO_2, a 9.5 wt.% loss was observed as the 3-(Trimethoxysilyl)propyl methacrylate was degraded on the nanoparticle surface.

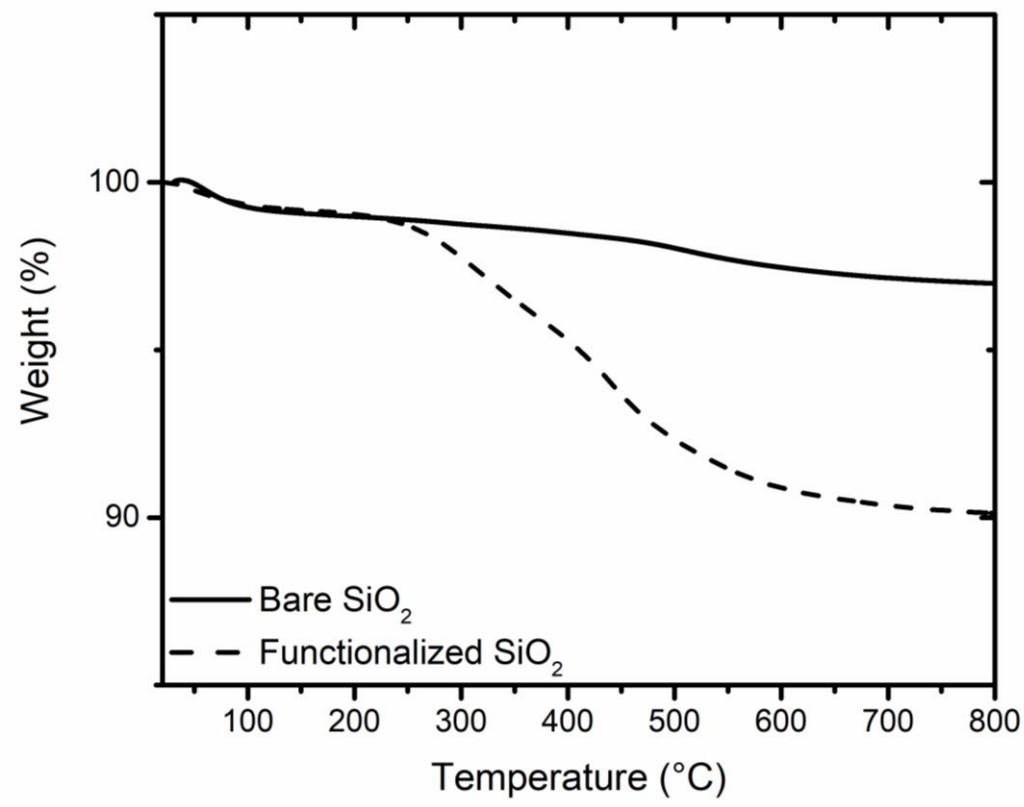

Figure 4-5 TGA data of bare and silane functionalized SiO_2 in nitrogen atmosphere

The grafting yield and grafting density of the silane onto the SiO_2 nanoparticles was calculated using previous methods described in literature.[27,28] The grafting yield of the functionalization or the amount of silane attached to the SiO_2 surface was determined through the use of Equation 4.2:

$$\text{Grafting Yield (\%)} = \frac{\text{Grafting Density}}{\text{[inital silane conc.]}} \text{ x } 100 \quad (4.2)$$

The initial silane concentration was determined from Equation 4.3:

$$\text{[inital silane conc]} = \frac{m_{silane}}{m_{SiO_2} \bullet SSA_{SiO_2} \bullet MW_{silane}}, \quad (4.3)$$

where m_{silane} is the mass of silane added in the reaction, m_{SiO2} is the mass of SiO_2 nanoparticles functionalized, SSA_{SiO2} is the specific surface area of SiO_2 (m^2/g), and MW_{silane} is the molecular weight of 3-(trimethoxysilyl)propyl methacrylate (248.35 g/mol). The specific surface area was approximated using the relationship for uniform spheres in Equation 4.4,[29]

$$SSA_{SiO_2} = \frac{6}{d \bullet \rho}, \tag{4.4}$$

where d is the particle diameter (15 nm) and ρ is the density of SiO_2 particles (2.2 g/mL). The SSA of SiO_2 was calculated to be 181.82 m^2/g. From these relationships the initial silane concentration used during functionalization was 9.25 $\mu mol/m^2$.

The grafting density ($\mu mol/m^2$) of silane attached to the surface of SiO_2 was calculated directly from the weight loss found during TGA,

$$\text{Grafting Density} = \frac{(\frac{W_{silane}}{100 - W_{silane}}) \bullet 100 - W_{SiO_2}}{MW_{silane,attached} \bullet SSA_{SiO_2}} \bullet 10^4, \tag{4.5}$$

where W_{silane} is the weight loss of silane from 60- 730°C, W_{SiO2} is the weight of loss of bare silica, and $MW_{silane,attached}$ is the molecular weight of the attached silane where on average 2 of the 3 methoxy silanes (bidental attachment) have covalently attached (186 g/mol). The grafting density was found to be 0.02 $\mu mol/m^2$. Based on the initial silane concentration and the grafting density, the grafting yield of the functionalized particles was 0.215 %, low due to the amount of surface area of the 15 nm SiO_2 nanoparticles. The grafting yield indicated successful attachment, but not enough to reduce the reactivity of the surface of SiO_2 when placed in cement.

4.3.3 Composite Hydrogel Characterization

The addition of functionalized SiO_2 did not disrupt the reaction as observed with the use of bare SiO_2. No large gel sedimentation was observed over the reaction and the particles were kept suspended over the 6-hour synthesis. Upon filtering, PAM samples were collected as fine powders and could be easily handled. For PAA samples, the filtered gel particles formed very hard dried aggregates. The PAA gels were composed of many irregular shape and were similar to ones previously discussed.

An example micrograph of a spherical 5 wt. % functionalized SiO_2 in PAM hydrogel particles from optical microscopy is shown in Figure 4-6. Table 4-2 summarizes the average diameters for the hydrogels with 0 (PAM), 1 (PAM-1SiO_2), and 5 (PAM-5SiO_2) wt. % by monomer of SiO_2. For PAM with no SiO_2 particles, the average diameter was 74.54 μm which is similar to previously reported PAM hydrogels.[17] For samples with SiO_2 incorporated, the size trended to large sizes for both 1 and 5 wt. % to 84 μm for average size, but within deviations, the size does not appreciably change for the different hydrogels.

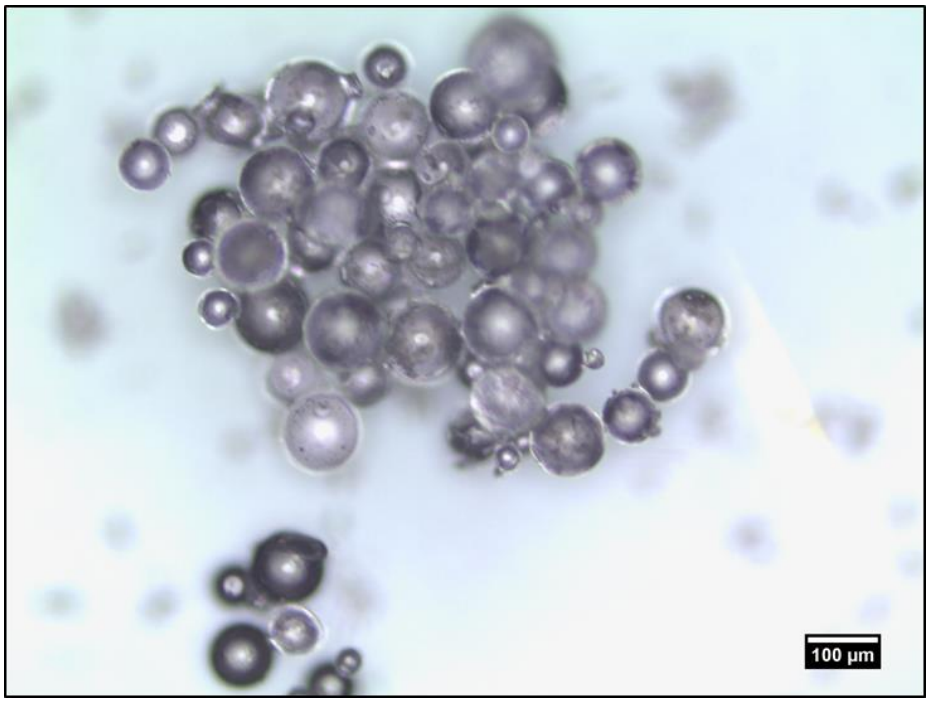

Figure 4-6 Optical micrograph of PAM-5SiO_2 composite hydrogel

Table 4-2 Particle diameters calculated from optical images for PAM composite hydrogels

Sample	**Size (µm)**
PAM	74.54 ± 34.27
PAM- 1SiO_2	83.97 ± 32.14
PAM- 5SiO_2	83.90 ± 27.09

Scanning electron microscopy was used to determine morphological differences in gel particles that cannot be detected with optical microscopy. In optical microscopy, the SiO_2 nanoparticles were not observed clearly. For SEM, large aggregates of SiO_2 are found to reside on the surface and dispersed throughout the particles. In Figure 4-7A, PAM hydrogel with no SiO_2 displays very nice spherical shape. There were signs of places where particles that were fused together had broken apart from one another. The PAM-1SiO_2 image, as shown in Figure 4-7B, indicated that large SiO_2 aggregates are found on the hydrogel

particles. In Figure 4-7C, PAM-5SiO_2 gel showed a better decoration of large aggregates on the surface. These aggregates are much larger than the primary particle size of 15 nm. The high level of aggregation made sizing of the SiO_2 particles very difficult when attempted with dynamic light scattering.

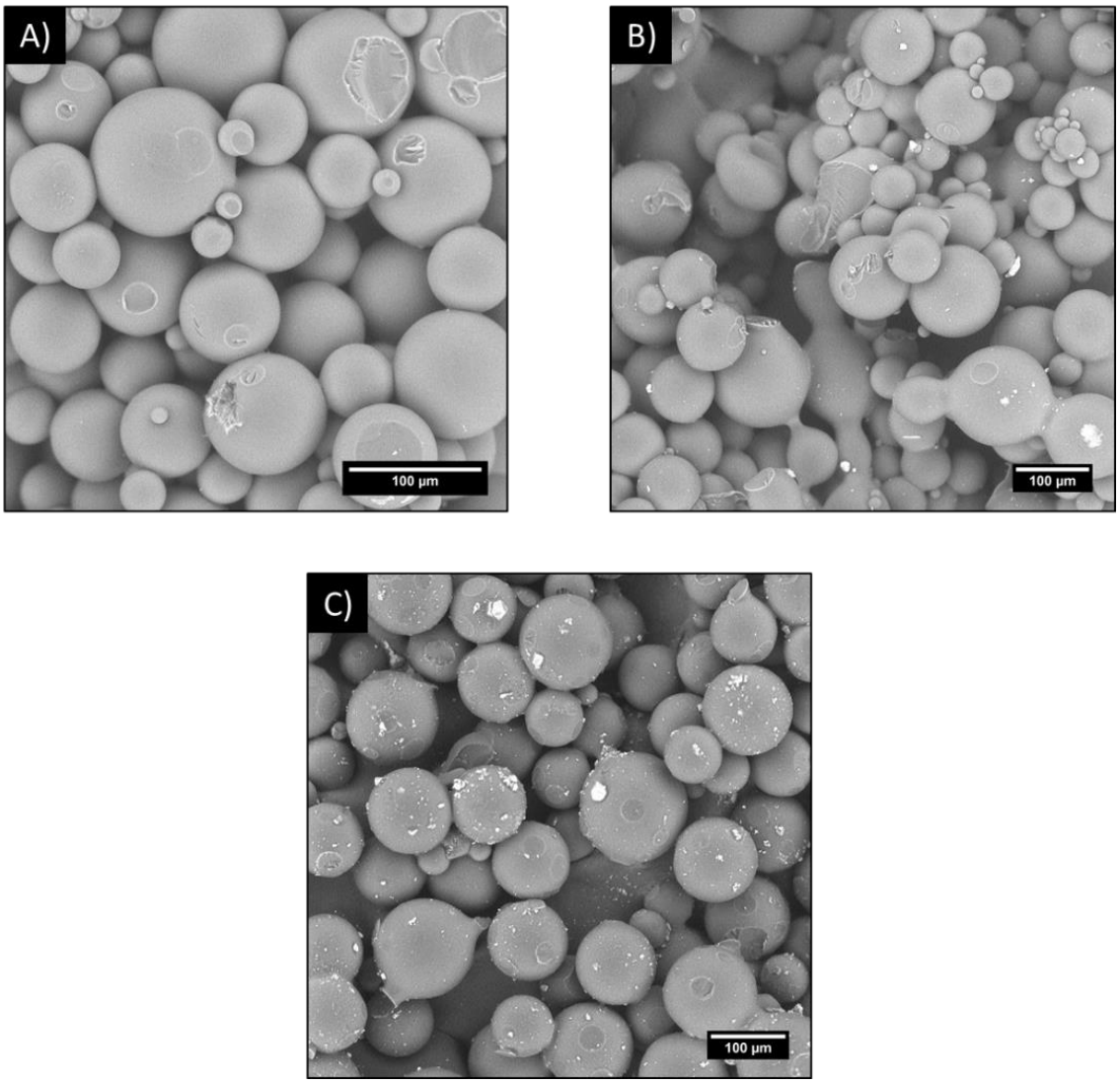

Figure 4-7 SEM micrographs for PAM composite hydrogels of A) PAM, B) PAM-1SiO_2, and C) PAM-5SiO_2

Elemental analysis via energy dispersive spectroscopy (EDS) was performed during SEM to confirm that SiO_2 was present at the surface as shown in Figure 4-8. For

both samples, the large aggregates were confirmed to be SiO_2. The composition collected atomic percentages that are close to that expected of SiO_2. The analysis also detected C and N which are the main constituents of PAM.

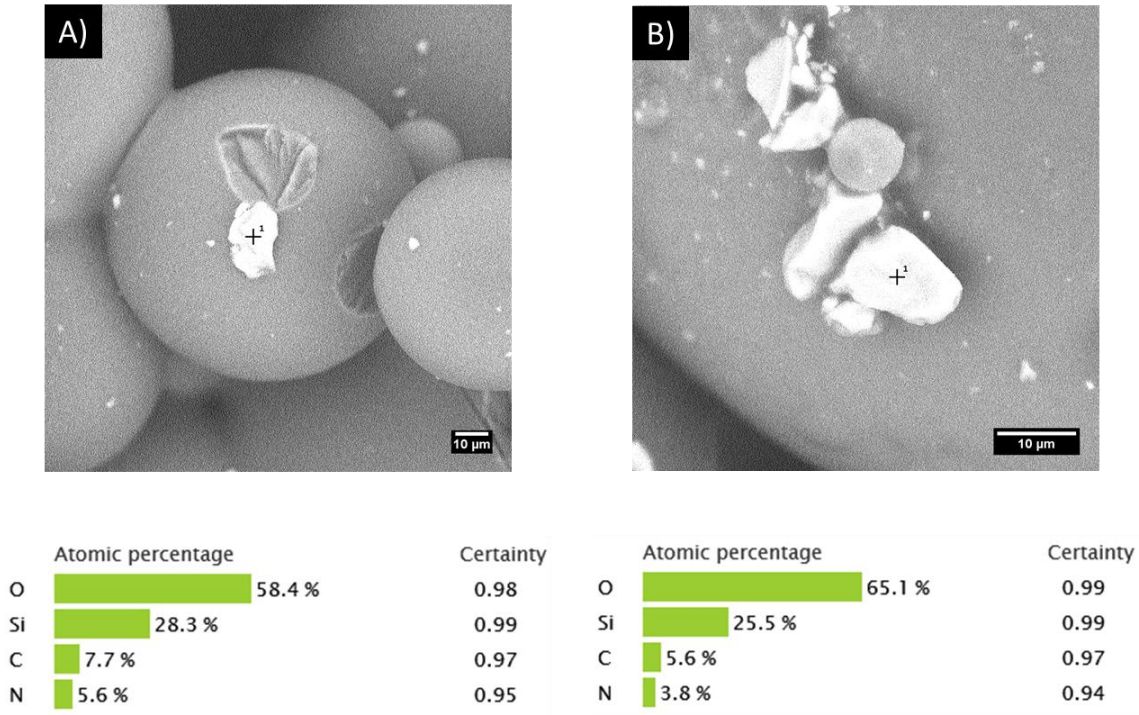

Figure 4-8 Elemental analysis of A) PAM-1SiO_2 and B) PAM-5SiO_2

The swelling performance of the composite hydrogels were tested in reverse osmosis water. The results of gravimetric swelling tests are present in Figure 4-9A for PAM, PAM-1SiO_2, and PAM-5SiO_2. For all tests, the swelling ratio reached equilibrium swelling with 5 mins. The PAM-1SiO_2 gel exhibited the highest swelling, but all samples were very close to each other at swelling ratios of 10-14 g/g. Gels were recollected after the initial swelling experiments and swollen again in RO water. Only a limited amount of the gels was recovered so only one test was conducted for each sample. Overall, the swelling behavior decreased and ranged from 8- 10 g/g as observed in Figure 4-9B.

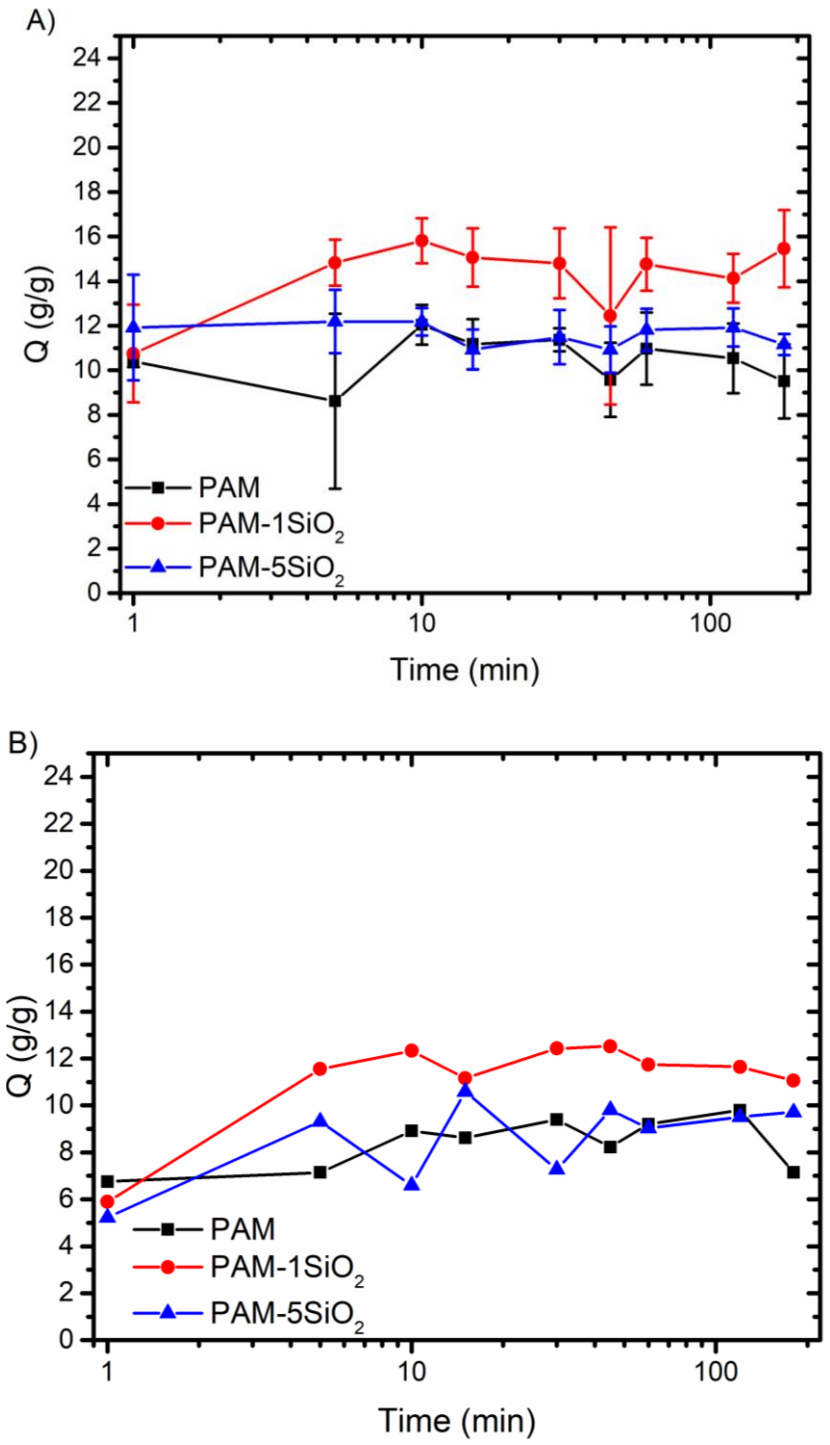

Figure 4-9 Swelling behavior of composite hydrogels in RO water for A) initial swelling and B) re-swelling experiments.

TGA curves of PAM, PAM-1SiO_2, and PAM-5SiO_2 in inert nitrogen atmosphere are shown in Figure 4-10. The behavior of all 3 samples were similar and exhibited three regions of weight loss and degradation.[30,31] The first region was for temperatures <220°C where water was evaporated. Samples were kept under vacuum to keep from absorbing large amounts of free water into the network, but water did adsorb strongly into the gel. The second region of 220-340°C was the decomposition of the amide group to form ammonia (NH_3). Main chain scission of PAM was observed in the third region of 340-430°C. The residual weight loss at the end of the experiment was not able to determine SiO_2 due to the large amount of char left over in the alumina pans.

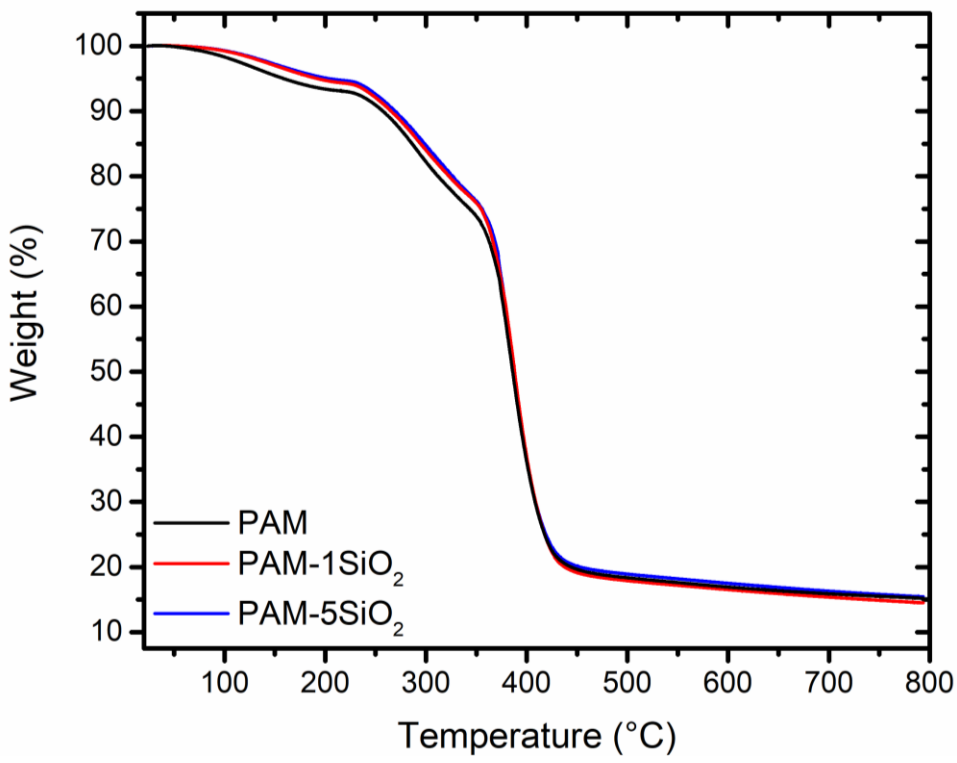

Figure 4-10 TGA data of composite hydrogels in nitrogen atmosphere

The results of TGA experiments ran in compressed air are presented in Figure 4-11. Degradation of hydrogels followed the same regions as previously observed in nitrogen,

but now the complete weight loss of all residual organic and char were removed as CO_2. For PAM and PAM-1SiO_2, the remaining weight for both samples was negligible. The weight remaining for PAM-5SiO_2 was 1.62 %. The low residual weights determined during tests can be explained by the amount of SiO_2 loaded into the system. The loadings were 1 and 5 wt.% by monomer and converting that to solids loadings based on reactants participating in polymerization they are 0.89 and 4.3 wt. %, respectively. For PAM-1SiO_2, the residual SiO_2 may not be detected since it is close to the precision of the instrument ($\pm$0.01%). With the large aggregation observed from SEM images, the SiO_2 particles were heterogeneously dispersed on the hydrogel particles surfaces and TGA was only able to give bulk data. For PAM-5SiO_2, residual contents were analyzed using FTIR and matched the bare SiO_2 spectra indicating that all organics were removed and only SiO_2 remained.

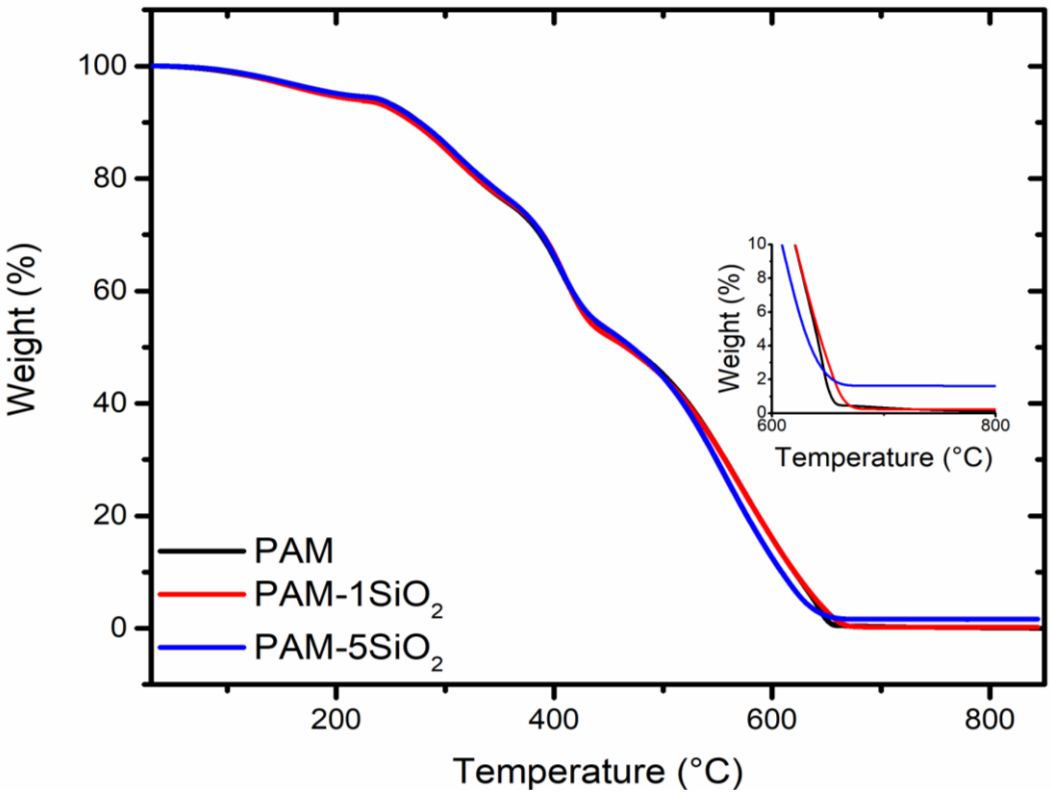

Figure 4-11 TGA data of composite hydrogels in compressed air

4.3.4 Cement Paste Microstructure

Microstructures from SEM of PAM and PAM-5SiO_2 containing cement pastes are shown in Figure 4-12. In these images, gray phases indicated hydrated cement, while the unhydrated cement can be seen as the light gray or white phases. Both samples were hand mixed, and therefore exhibited porosity. For the control PAM sample, the original spherical void from the PAM particle can be observed and hydrated products of $Ca(OH)_2$ can be seen refilling the void.

For the PAM-5SiO_2 sample, calcium-rich phase has almost completely filled in the particle void. The growth developed a connected network, whereas the control sample did not have this crystal and phase consolidation. Elemental analysis of hydrogel void and cement matrix are shown in Figure 4-13. For Spot 1 located in the crystal growth within the perimeter of the hydrogel, $Ca(OH)_2$ appears to be the likely hydrated product. Calcium carbonate ($Ca(CO_3)$ could form as a result of $Ca(OH)_2$ that was converted when in contact with air during the several steps that the paste had to undergo before being mounted in epoxy. Silicon was also detected in the scan, but it was not evident if that was a result of SiO_2 within the composite hydrogels or already present in the original chemical composition of the Portland cement as shown in the results of Spot 2.

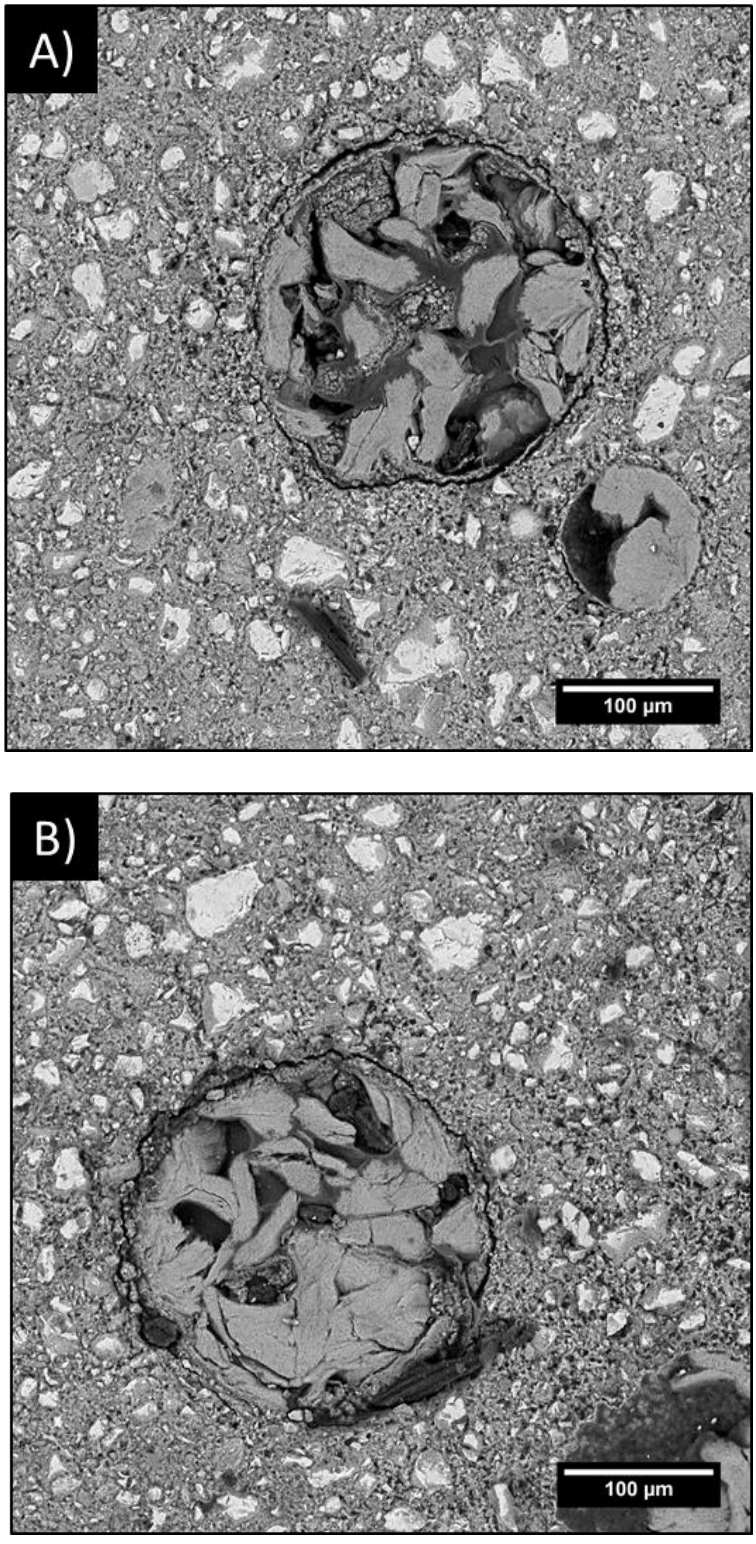

Figure 4-12 SEM micrographs of cement paste microstructures of A) PAM and B) PAM-5SiO_2

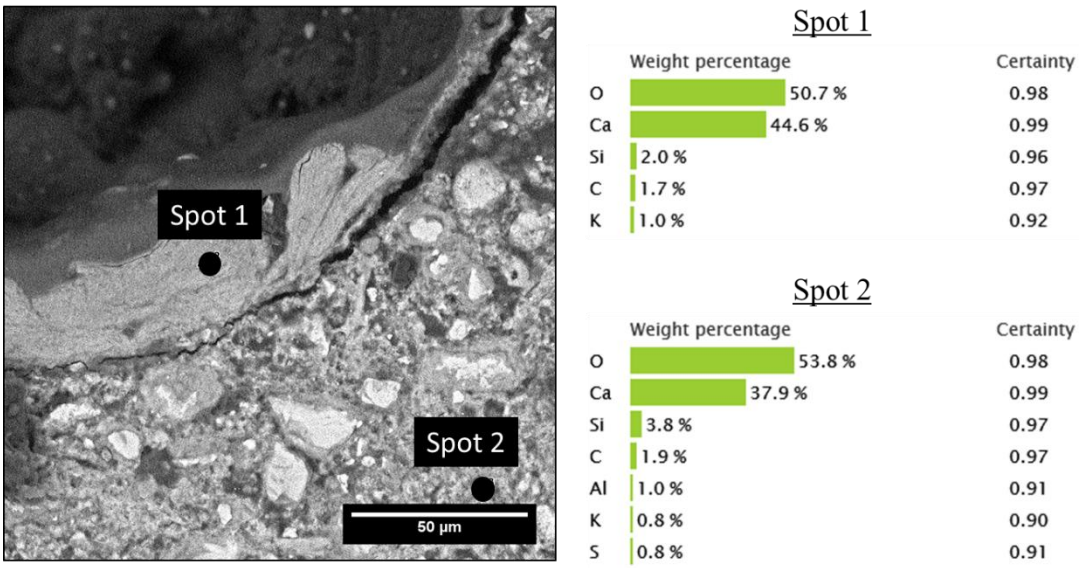

Figure 4-13 Elemental analysis of PAM-5SiO_2 hydrogel in cement paste

4.4 Conclusions

Synthesis routes of composite hydrogels for use in high performance concrete were investigated. First attempts of using hydrophilic bare SiO_2 were unsuccessful due to competition with surfactant that caused an uncontrolled rapid reaction and gelation to form fused spherical SAPs. Functionalization of SiO_2 with an acrylate silane changed the surface properties to be more hydrophobic, so that spherical hydrogel particles could be attained. The relatively low grafting yield was not an issue as bare silica surface was needed for pozzolanic reactivity when mixed with Portland cement.

Characterization of the composite hydrogels indicated that SiO_2 loading did not alter swelling behavior or thermal stability. The loadings of SiO_2 may not have been completely incorporated into the gels and were heterogeneously dispersed. Cement paste microstructures of PAM and PAM-5SiO_2 indicated that hydrated product grew into the void of the spherical particle voids. Future work will aim to incorporate higher amounts of SiO_2 and determine the mechanical properties of composite hydrogels in concrete.

4.5 Suggestions for Future Work

Future work will need to investigate how the SiO_2 is dispersed in the network. The low residual weight of the hydrogels from TGA does not give a definitive answer on how the SiO_2 is dispersed or how it stays in the gel. The gels are washed intensively with large amounts of water that causes the network to swell over time. Residual initiator and monomer are washed off in the process and the gels are then allowed to dry in the fume hood.

Some of the SiO_2 could be washed off during filtering after the polymerization. With the large agglomeration of SiO_2 particles suspended in the aqueous phase, the SiO_2 may not be able to covalently attach during the hydrogel polymerization and only be physically bound to the interface. During the filtering of the gel particles with organic solvents, the SiO_2 could be washed off resulting in low incorporation of the nanoparticles within the gels. SEM images of reswollen gels did not exhibit noticeable removal of SiO_2 particles on the surface of the composite hydrogels.

The use of larger SiO_2 of size ranges of 100 nm or greater could help with dispersion leading to better incorporation of SiO_2 within the hydrogels. The larger sizes might not have the aggregation issues associated with the smaller SiO_2 used in this study. TGA is still the most appropriate method to quantify SiO_2 loading and can be coupled with SEM to do a stereology analysis.

For poly(acrylic acid) gel compositions, hydrogels were difficult to collect and filter. These gels did not polymerize to form a fine powder as the polyacrylamide composite hydrogels. These gels had a more fused but spherical shape. To create a better spherical hydrogel, the amount of surfactant will need to be investigated as well as neutralization of the AA monomer. The nonionic character of the surfactant may interact with the non-

neutralized AA monomer segments during polymerization to cause the irregularly shaped particles.

For the hydrogel-cement mixture pastes, a more in-depth void analysis will need to be done to understand the inorganic phase formation. The analysis presented here was building upon the knowledge of voids being filled in partially using polyacrylamide hydrogels. Currently, it is not understood if the incorporated SiO_2 within the gels has a large effect of the hydrated products of $Ca(OH)_2$ and calcium silicate hydrate formation. The void analysis using SEM and EDS would indicate the amount of the different inorganic phases growing into the void.

4.6 References

(1) Bonavetti, V.; Donza, H.; Menéndez, G.; Cabrera, O.; Irassar, E. F. *Cem. Concr. Res.* **2003**, *33* (6), 865–871.

(2) Jozwiak-Niedzwiedzka, D. *Cem. Concr. Compos.* **2005**, *27* (6), 709–715.

(3) Zhutovsky, S.; Kovler, K. *Cem. Concr. Res.* **2012**, *42* (1), 20–26.

(4) Zhutovsky, S.; Kovler, K. *Constr. Build. Mater.* **2017**, *144*, 311–316.

(5) Castro, J.; Keiser, L.; Golias, M.; Weiss, J. *Cem. Concr. Compos.* **2011**, *33* (10), 1001–1008.

(6) Cusson, D.; Hoogeveen, T. *Cem. Concr. Res.* **2008**, *38* (6), 757–765.

(7) De La Varga, I.; Castro, J.; Bentz, D.; Weiss, J. *Cem. Concr. Compos.* **2012**, *34* (9), 1001–1008.

(8) Mazloom, M.; Ramezanianpour, A. A.; Brooks, J. J. *Cem. Concr. Compos.* **2004**, *26* (4), 347–357.

(9) Behnood, A.; Ziari, H. *Cem. Concr. Compos.* **2008**, *30* (2), 106–112.

(10) Walker, R.; Pavía, S. *Mater. Struct. Constr.* **2011**, *44* (6), 1139–1150.

(11) Justs, J.; Wyrzykowski, M.; Bajare, D.; Lura, P. *Cem. Concr. Res.* **2015**, *76*, 82–90.

(12) Schröfl, C.; Mechtcherine, V.; Gorges, M. *Cem. Concr. Res.* **2012**, *42* (6), 865–873.

(13) Zhu, Q.; Barney, C. W.; Erk, K. A. *Mater. Struct.* **2015**, *48* (7), 2261–2276.

(14) Krafcik, M. J.; Erk, K. A. *Mater. Struct. Constr.* **2016**, *49* (11), 4765–4778.

(15) Krafcik, M. J.; Macke, N. D.; Erk, K. A. *Gels* **2017**, *3* (4), 46.

(16) Kelly, S. L. Inverse Suspension Polymerization of Superabsorbent Polymer (SAP) Hydrogels for Internally Cured Concrete, Purdue University, 2017.

(17) Davis, C. R.; Kelly, S. L.; Erk, K. A. *J. Appl. Polym. Sci.* **2018**, *135* (14), 1–10.

(18) Odian, G. *Principles of Polymerization*; John Wiley & Sons, Inc.: Hoboken, NJ, USA, 2004.

(19) Kiatkamjornwong, S.; Phunchareon, P. *J. Appl. Polym. Sci.* **1999**, *72* (10), 1349–1366.

(20) Mayoux, C.; Dandurand, J.; Ricard, A.; Lacabanne, C. *J. Appl. Polym. Sci.* **2000**, *77* (12), 2621–2630.

(21) Zhang, K.; Wang, Q.; Meng, H.; Wang, M.; Wu, W.; Chen, J. *Particuology* **2014**, *14*, 12–18.

(22) Yoon, D. H.; Jang, J. W.; Cheong, I. W. *Colloids Surfaces A Physicochem. Eng. Asp.* **2012**, *411*, 18–23.

(23) Chevalier, Y.; Bolzinger, M.-A. *Colloids Surfaces A Physicochem. Eng. Asp.* **2013**, *439*, 23–34.

(24) Opawale, F. O.; Burgess, D. J. *J. Colloid Interface Sci.* **1998**, *197* (1), 142–150.

(25) Binks, B. P.; Lumsdon, S. O. *Langmuir* **2000**, *16* (23), 8622–8631.

(26) Zhang, K.; Chen, H.; Chen, X.; Chen, Z.; Cui, Z.; Yang, B. *Macromol. Mater. Eng.* **2003**, *288* (4), 380–385.

(27) Pardal, F.; Lapinte, V.; Robin, J.-J. *J. Polym. Sci. Part A Polym. Chem.* **2009**, *47* (18), 4617–4628.

(28) Bartholome, C.; Beyou, E.; Bourgeat-Lami, E.; Chaumont, P.; Lefebvre, F.; Zydowicz, N. *Macromolecules* **2005**, *38* (4), 1099–1106.

(29) Paul C. Hiemenz, R. R. *Principles of Colloid and Surface Chemistry, Third Edition, Revised and Expanded*; CRC Press: Boca Raton, Fl, 1997.

(30) Silva, M. E. S. R. .; Dutra, E. R.; Mano, V.; Machado, J. C. *Polym. Degrad. Stab.* **2000**, *67* (3), 491–495.

(31) Zhou, C.; Wu, Q. *Colloids Surfaces B Biointerfaces* **2011**, *84* (1), 155–162.

CHAPTER 5. CONCLUSIONS

5.1 Summary of Projects

The characterization and synthesis of acrylic-based polymer gels were studied using various approaches. In the first two projects, rheology was the main method to study a model gel system for self-healing materials. In the final project, polymer gels were synthesized and characterized as novel internal curing admixtures for cementitious applications.

The initial material system investigated was a physically associating thermoreversible triblock copolymer gel composed of poly(methyl methacrylate)-poly(n-butyl acrylate)-poly(methyl methacrylate). This gel with a well-defined network was used as a model system to study fracture-healing behavior and timescales. By using an applied shear rate methodology, the gel was fractured and then allowed to heal undisturbed in the rheometer for set times. The gel was then fractured again at the same shear rate. The healing response was characterized by the ratio of the maximum shear stress responses of the two fracture events. For each concentration and temperature studied, full recovery of the gel network could be achieved given enough time to recover. For warmer temperatures of 28 and 25°C, the time required for a network to fully heal was on the order of minutes to a few hours. The timescales for the colder temperatures of 23 and 20°C were extended to several hours. The activation energy barriers for healing and relaxation were determined through Arrhenius relationships.

A custom-built rheo-physical flow visualization set up was used to confirm fracture during shear rheometry. It was determined that fracture occurred in the middle of the experimental gap and that fully healed gels fractured in a different location. This indicated

that full network healing occurred and that there was no residual defect or incomplete healing to propagate fracture.

The second project was a follow-up study in the fracture-healing behavior of the model triblock gel. A relationship between the stress recovery and normalized timescales of post-fracture resting time and the gel's characteristic relaxation time was developed to understand the effects on strength recovery. This relationship was developed into a master curve, which indicated that the time needed to achieve a fully healed network was 100-1000 times the relaxation time of the gel.

The deformation strain magnitudes were varied from 700 (near stress overshoot) to 4000% to understand amount of fracture on the timescales of complete healing. The healing kinetics differences were observed between the two strain magnitudes. For gels at concentration of 5 vol. % at all temperatures tested and gels at 5.5 vol. % for warm temperatures of 28 and 25 °C, the large strain experiments had shorter resting times for fully healed networks. This was explained by viscous heating for the fixture from frictional healing. For the shorter strain magnitude experiments, lower temperatures of 23 and 20 °C of 5.5 vol. % and all temperatures of 6 vol. % had faster healing kinetics due in part to possible partial or incomplete fracture propagation. Rheophysical experiments were used to determine that the stress overshoot could be captured using rheology data before fracture fully propagated across the gel.

For the final project, routes for synthesizing spherical composite hydrogels for use as internal curing admixtures in high performance concrete were explored. The addition of bare SiO_2 did not yield spherical particles appropriate for the application, but by functionalizing SiO_2 nanoparticles, polyacrylamide composite hydrogels were achieved.

Functionalization of the SiO_2 was accomplished by using an acrylate-based silane molecule to covalently attach to SiO_2 nanoparticle surface. Grafting yield was found to be low at 0.215 %, but enough silane was attached to change the surface character. Loadings of functionalized SiO_2 were varied from 1 to 5 wt. % by monomer and inverse suspension polymerization was used to create composite hydrogels.

Characterization of composite hydrogels indicated little effect on swelling behavior and thermal degradation. From optical microscopy, particle size did not appreciable change, but from SEM images, SiO_2 particles were observed on the surface of polymer gel spheres.

5.2 Future Work and Outlook

For the composite hydrogel work, many synthesis routes were attempted as shown in Chapter 4 and Appendix A. With the successful synthesis of polyacrylamide hydrogels with incorporated SiO_2, future work can aim on optimizing parameters and performance in concrete. The SiO_2 used in these studies were 15 nm and exhibited high levels of aggregation to particles with sizes in the 100 nm's to μm's range. The type of SiO_2 can be changed that have larger diameters, such as 60-100nm, or using industrial silica fume. The functionalization can be optimized to try to have more silane coverage and better covalent bonding into the gel network.

The spherical composite hydrogel research is happening in conjunction with ongoing work of irregular shaped composite hydrogels. By having these two types of hydrogels, the effects of shape can be studied for their effects on concrete microstructure and mechanical properties. Understanding of mechanical properties will be key in determining the effectiveness of composite hydrogels in concrete. The voids that are filled in by hydrated product are observed for control hydrogels and composite hydrogels.

With the addition of pozzolanic SiO_2, the hydrated product with more desirable silicate content should have high compressive strength and performance.

In conclusion, polymer gels can have a variety of properties that allow them to be used in many different applications based upon the nature of the crosslinking. Gel mechanical properties are difficult to study using traditional methods, but chemical and physical gels can be characterized using other methods to capture the healing response and swelling behaviors. This work was able to explore new methods and synthesis routes for physical and chemical acrylic-based gels in a variety of applications.

APPENDIX A. HAIRY NANOPARTICLE SYNTHESIS ROUTES

Hydrogel networks composed of poly(acrylic acid) (PAA) and poly(acrylamide) (PAM) grafted onto silica (SiO_2) nanoparticles with uniform crosslinking were attempted through various methods. The gels with controlled molecular weights and well-defined networks would have been ideal materials to study structure-property relationships.

The main application for these composite hydrogels is to be a model system for a new type of internal curing agents for high performance concrete. Previous group research has shown that super absorbent polymer (SAP) hydrogels with varying ratios of PAA:PAM are beneficial to concrete curing as discussed in Chapter 4. By incorporating SiO_2 within the network, the curing reaction can proceed in creating essential silicate phase that indicate a strong binding compound within the concrete. The ability to control polymer composition, molecular weight, crosslink density for the polymer network, and the grafting density of the polymer onto SiO_2 particles would allow for fundamental structure-property relationships to be studied and their effects on concrete.

The polymer-grafted nanoparticles or hairy nanoparticles (HNPs) before being incorporated into gel networks can be used to study fundamental structure and dynamics. The ability to graft polymers with precisely controlled molecular weights allows for the use of neutron and x-ray scattering to probe different length scales of these materials (particle-particle spacing and polymer graft length).[1–5] The rheology of similar hairy nanoparticle systems have been studied throughout literature.[6,7] By synthesizing and characterizing PAA/PAM polymer hairy nanoparticles independently, a more complete and in-depth understanding of HNP dynamics and further study into composite hydrogels could be gained.

The main strategies for polymer-grafted nanoparticles (hairy nanoparticles) are divided into areas based on linking polymer to the nanoparticle: “grafting-to” and “grafting-from.” The “grafting-to” approach allows polymers to be synthesized and then subsequently attached to the surface of particles. The amount of polymer coverage on the surface can be relatively low due to the steric hindrance as polymers are attaching to different sites. To achieve greater grafting density, the “grafting-from” approach uses an anchored or attached molecule to the surface that facilitates polymerization and chain growth. The chemistries and steps can be complex.

Reversible addition fragmentation chain transfer (RAFT) polymerization was used to synthesize polymers. The RAFT process allows for low polydispersity and targeted molecular weights to be obtained at mild conditions. RAFT polymerizations have been successfully used to polymerize acrylamide[8,9] and acrylic acid[10,11]. A main feature of RAFT is the use of a chain transfer agent (CTA) that allows propagating radicals to chain transfer without terminating any growing chains and keeps chains growing at the same rate. The versatility of CTA chemistries makes it ideal and achievable to create hairy nanoparticles by both “grafting-to” and “grafting-from” strategies. Equation A-1 can be used to predict molecular weights of polymers at full conversion

$$M_{n,\mathrm{Theoretical}} = \frac{[M]_o MW_{monomer}}{[RAFT]_o} + MW_{CTA} \qquad (A.1)$$

where $[M]_o$ is the concentration of monomer, $MW_{monomer}$ is the molecular weight of the monomer, [RAFT]o is the concentration of RAFT CTA, and MW_{CTA} is the molecular weight of the CTA.

Routes:

The first approach was a "grafting-from" strategy based upon details from Gao, et. al[11] by using a commercial CTA (cyanomethyl [3-(trimethoxysilyl)propyl] trithiocarbonate, Sigma-Aldrich). The CTA with a silane functional group can be used to attach to the SiO_2 surface while simultaneously participating in the RAFT polymerization. Work was not continued with this commercial CTA due to long delays in procurement.

Based on upon Qu and co-workers,[12] CTA was attempted to be synthesized to be more compatible with PAA/PAM. The reaction conditions called for 3-day reflux with condenser and use of somewhat dangerous reagents coupled with low yields made this not a viable solution for beginning hairy nanoparticle research.

Grafting-To

The "grafting-to" approach was then attempted to synthesize PAA and PAM HNPs. This work was based upon a series of studies from Ranjan and Brittain to create HNP from RAFT and click chemistry.[13–15] This approach was used to make samples for neutron scattering experiments in May 2015 on small angle neutron scattering.

A commercial CTA was used (2-(Dodecylthiocarbonothioylthio)propionic acid (DoPAT) from Sigma-Aldrich) and then modified with an alkyne (C≡C) group. Particles were functionalized in three steps to afford an azide($-N_3$) group. Polymers were synthesized with the modified CTA and then reacted with the azide-functionalized particles to form hairy nanoparticles.

The typical CTA modification steps are described below. The studies of Ranjan and Brittain[13–15] were followed but a different silane molecule was used (4-(chloromethyl)phenyl trimethoxy silane from Alfa Aesar). 0.5 g of DoPAT was dissolved in 5 mL of dichloromethane in a scintillation vial to form a yellow liquid. 0.4 g of N-(3-(dimethylamino)propyl)-N'-ethylcarbodiimide hydrochloride (EDC) was then added and the solution turned orange or red. 0.25g of 4-(N,N-dimethylamino) pyridine (DMAP) was then to the vial and the contents were transferred to a 50 mL round bottom flask. The flask was kept under N_2 atmosphere and 25°C in an oil bath. After 30 min, 0.25 mL of propargyl alcohol was added and the reaction was allowed to go 18 hours. The reaction was quench by placing the flask in ice water. The contents were transferred to a separatory funnel and washed with 10% HCl, water, and brine solution three times each. Figure A-1 illustrates an example of the separation of the organic and aqueous layers during CTA modification. The bottom layer (organic) was retrieved after washing and was dried under vacuum.

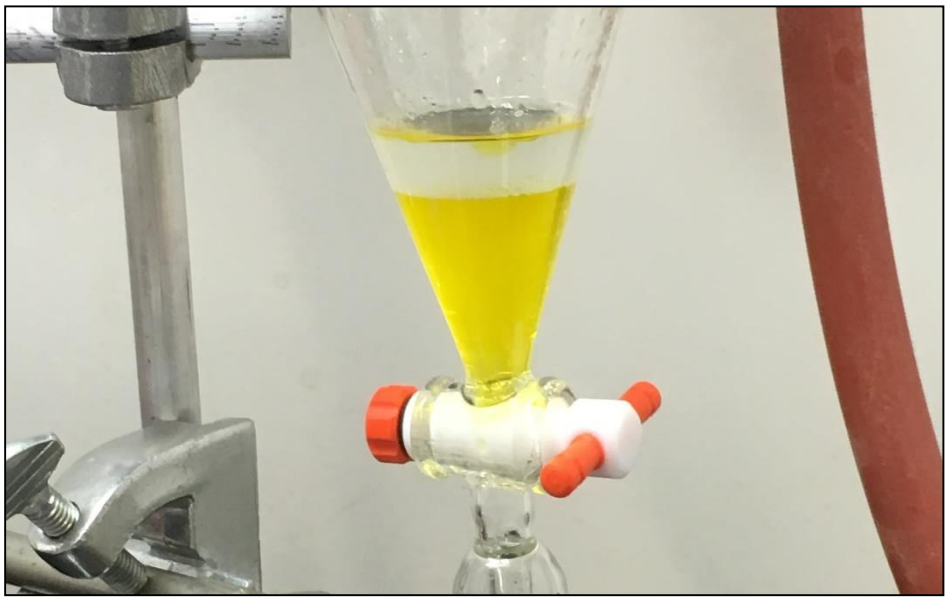

Figure A-1 Example of separatory funnel of top aqeous layer and bottom organic layer

The functionalization of SiO_2 particles was carried out in the following steps as examples. 6 g of SiO2 particles (US nanocomposites, reported diameter=60 nm) were dispersed in 100 mL of anhydrous toluene in a 250 mL round bottom flask. A sonication bath was used to disperse the particles. The flask was then heated under N_2 atmosphere at 80°C in an oil bath. 5.5 mL of 4-(chloromethyl)phenyl trimethoxy silane in 15 mL of toluene was added via syringe and the reaction was continued for 18 hrs. Particles were recovered by centrifuge at 3000 rpm for 30 mins and redispersed in toluene. This was repeated 3 times and Cl-functionalized particles (SiO_2-Cl) were dried in vacuum.

The next functionalization step is to substitute the chlorine-functionalized SiO_2 surface into an azide group. 3 g of SiO_2-Cl were dispersed in 100 mL of dimethylformamide (DMF) in a 250 mL round bottom flask. The flask was heated to 80°C under N_2 atmosphere. 1.8 g of sodium azide was added to the flask and the reaction was stirred overnight for 18 hours. Particles were recovered by centrifuge at 3000 RPM for 30 mins. The recovered particles were then dispersed in water and centrifuged for 3 cycles. Particles were then dried under vacuum to complete functionalization step of the SiO_2-azide.

RAFT polymerization with the alkyne-terminated CTA was performed for PAA samples in methanol, ethanol, and DMSO. Typical reaction conditions were 100 mL round bottom flasks in N_2 atmosphere at 70°C with solvent, monomer, CTA, and initiator all dissolved and ran for 4 hours. The use of ethanol as the solvent was preferred. Methanol was used at early stages, but 70°C was above the boiling point (65°C). DMSO was very difficult to remove from PAA polymerizations, but was used for PAM reactions. By using Equation A-1, theoretical molecular weights could be targeted since appropriate

characterization was not available at the time (gel permeation chromatography). High and low molecular weight samples for each polymer type were synthesized and purified.

This grafting-to approach called for the use of click-chemistry to graft the alkyne-terminated RAFT polymers to the azide-functionalized SiO_2 particles. The click-reaction was done by dissolving the polymer and particles in DMSO or water and then copper sulfate ($CuSO_4$) and sodium ascorbate were added to the vials at 55°C.

Results and Discussion

Synthesis and characterization of HNPs from the various methods were difficult due to instruments not being available or accessible and the ability of setting up a new platform for a research project and collaboration. The majority of results collected were for use as a guide while synthesizing samples for neutron scattering using the "grafting-to" approach.

Thermogravimetric analysis (TGA) was performed on samples under N_2 atmosphere to determine degradation of HNPs. Figure A- 2 illustrates the degradation of the pristine SiO_2 particles, functionalized particles (SiO_2-Cl and SiO_2-azide), and polyacrylamide grafted-to SiO_2 HNP samples. For the pristine SiO_2, the low temperature weight loss is attributed to water adsorbed to the particle surfaces. For the functionalized SiO_2 samples, the respective degradations correspond to the nature of the silane molecule anchors used. The HNP sample indicated that polymer to some degree has attached to the surface and approximately 15% of the original weight has been volatilized off. Due to problems with gel permeation chromatography, molecular weight measurements of samples were unable to be obtained to determine graft density.[16–18]

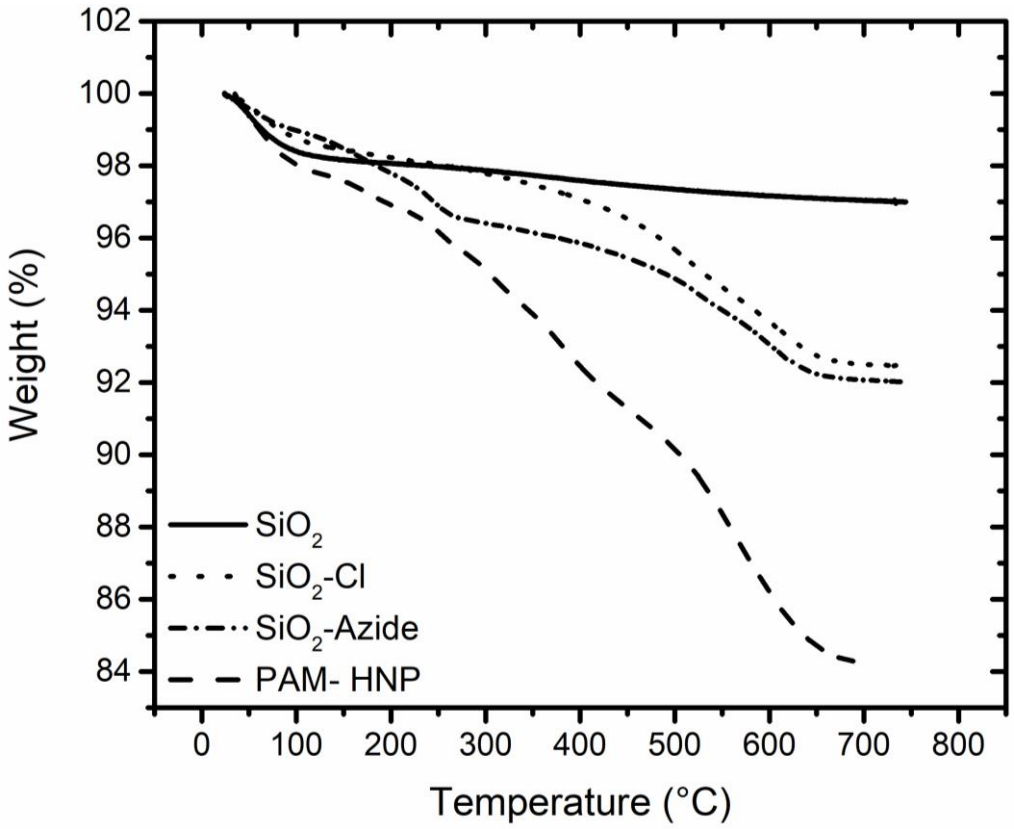

Figure A- 2 TGA data of SiO_2, various functionalization steps, and PAM hairy nanoparticles in nitrogen atmosphere

FTIR spectra shown in Figure A- 3was collected for the various functionalization steps and for HNP prepared with PAA polymer chains. The bare SiO_2 spectrum was similar to the one collected in Figure 4-4. The SiO_2-Cl functionalization step did not show any new notable peaks. For SiO_2-Azide, the peak 2105 cm^{-1} was attributed to the azide group. The PAA-HNP from click coupling spectrum has peaks at 2100 and 1711 cm^{-1} for possible unreacted azide and C=O stretching, respectively.

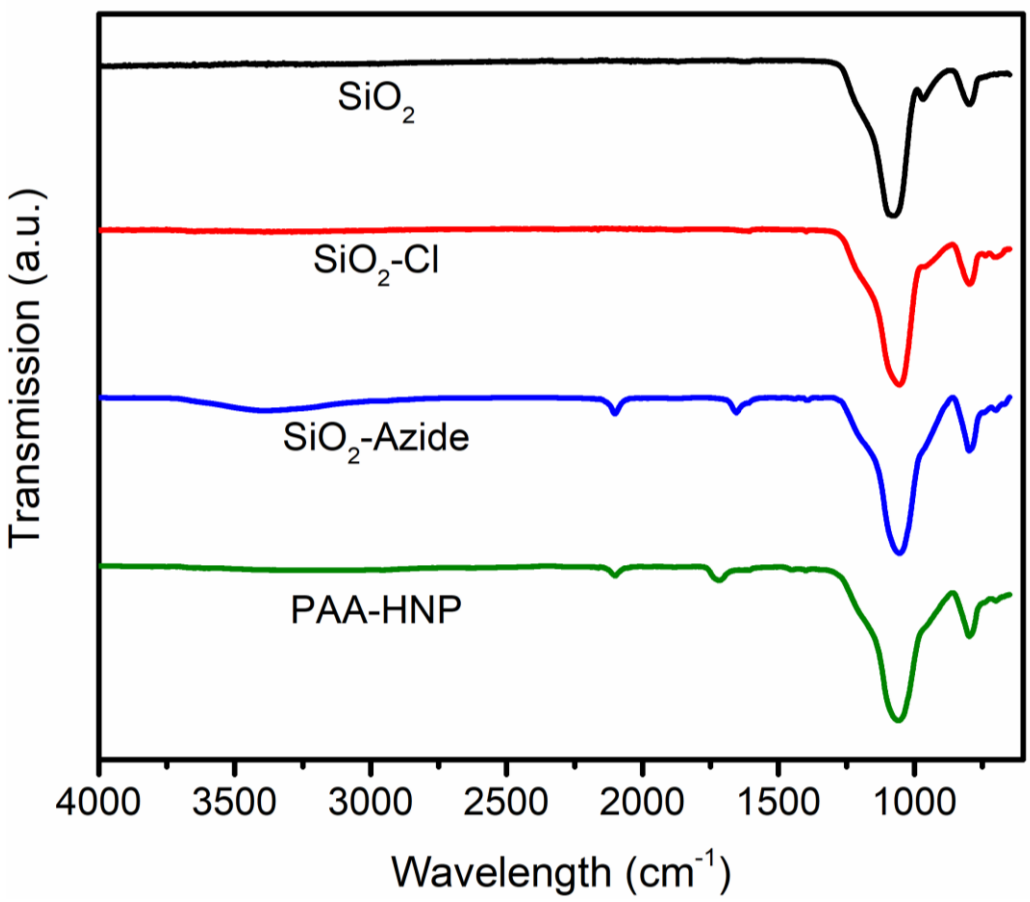

Figure A- 3 FTIR spectra of SiO_2, various functionalization steps, and PAA hairy nanoparticles

High and low molecular weight PAA and PAM HNP samples were studied using small angle neutron scattering (SANS) on the 10m nSOFT beam line instrument at the NIST Center for Neutron Research. Polymer HNPs samples were created with 2 different molecular weights of both PAA and PAM grafted to SiO_2 particles. Preliminary experiments to determine contrast matching were completed to calculate the amount of D_2O to H_2O for solutions to highlight the desired element, the polymer chains. It was found that both polymer could be contrast matched at ~33% D_2O. HNP solutions were made at that solvent composition and were tested, but results indicated that substantial aggregation of SiO_2 was present. Attempts to better disperse SiO_2 to improve data were unsuccessful.

Rheology experiments were done in collaboration with Kai Gao (PhD in Spring 2017). PAA grafted onto 100 nm SiO_2 were dispersed in water at concentrations from 1-5 mg/mL. The low yield obtained during synthesis batches did not allow for more concentrated samples. Oscillatory experiments in Couette cell geometry were not valid due to low torque. Flow curves and shear start-up experiments indicated the viscosity of each samples were near that of water (1 mPa*s). It is hypothesized that increasing the concentration would enhance HNP-HNP interactions causing jamming behaviors.

Suggestions/Future Work

The synthesis of HNPs to produce composite hydrogels were attempted via different methods. Each method had specific advantages, but yielded limited success. Overall, the grafting-to method using an available commercial CTA had the most promise, but issues with SiO_2 dispersion hampered further investigations of those systems. To improve the process, larger SiO_2 should be used (~100 nm diameter). This would be easier to disperse and work with during functionalization and synthesis. Recently, researchers in the Howarter group have had success using the Stöber method of creating monodisperse SiO_2 at that recommended size range.

Once HNP are successful, they can be incorporated into hydrogel systems in several ways. During synthesis of hydrogels, they can be added in and the gelation can proceed around them. With proper utilization of RAFT and handling of HNPs, the end groups are still living and can be further reacted with crosslinking agents.

With the success of using 3-(Trimethoxysilyl)propyl methacrylate from work in Chapter 4, HNP synthesis could also be investigated with that approach. This would be a “grafting-from” methodology and would require hydrofluoric acid (HF) etching to

determine polymer MW since attached polymer and free polymer in solution could be different.

References

(1) Chevigny, C.; Jestin, J.; Gigmes, D.; Schweins, R.; Di-Cola, E.; Dalmas, F.; Bertin, D.; Boué, F. *Macromolecules* **2010**, *43* (11), 4833–4837.

(2) Chevigny, C.; Dalmas, F.; Di Cola, E.; Gigmes, D.; Bertin, D.; Boué, F.; Jestin, J. *Macromolecules* **2011**, *44* (1), 122–133.

(3) Hammouda, B. *NIST Cent. Neutron Res.* **2010**.

(4) Hammouda, B. *Polym. Rev.* **2010**, *50* (1), 14–39.

(5) Rose, S.; Dizeux, A.; Narita, T.; Hourdet, D.; Marcellan, A. *Macromolecules* **2013**, *46* (10), 4095–4104.

(6) Srivastava, S.; Shin, J. H.; Archer, L. A. *Soft Matter* **2012**, *8* (15), 4097.

(7) Zhang, Q.; Archer, L. A. *Langmuir* **2002**, *18* (26), 10435–10442.

(8) Thomas, D. B.; Convertine, A. J.; Myrick, L. J.; Scales, C. W.; Smith, A. E.; Lowe, A. B.; Vasilieva, Y. A; Ayres, N.; McCormick, C. L. *Macromolecules* **2004**, *37*, 8941–8950.

(9) Thomas, D. B.; Sumerlin, B. S.; Lowe, A. B.; McCormick, C. L. *Macromolecules* **2003**, *36* (5), 1436–1439.

(10) Gao, K.; Kearney, L. T.; Wang, R.; Howarter, J. A. *ACS Appl. Mater. Interfaces* **2015**, *7* (44), 24839–24847.

(11) Gao, K.; Kearney, L. T.; Howarter, J. A. *J. Polym. Sci. Part B Polym. Phys.* **2017**, *55* (4), 370–377.

(12) Qu, Z.; Hu, F.; Chen, K.; Duan, Z.; Gu, H.; Xu, H. *J. Colloid Interface Sci.* **2013**, *398*, 82–87.

(13) Ranjan, R.; Brittain, W. J. *Macromol. Rapid Commun.* **2008**, *29* (12–13), 1104–1110.

(14) Ranjan, R.; Brittain, W. J. *Macromolecules* **2007**, *40* (17), 6217–6223.

(15) Ranjan, R.; Brittain, W. J. *Macromol. Rapid Commun.* **2007**, *28* (21), 2084–2089.

(16) Bartholome, C.; Beyou, E.; Bourgeat-Lami, E.; Chaumont, P.; Zydowicz, N. *Macromolecules* **2003**, *36* (21), 7946–7952.

(17) Pyun, J.; Jia, S.; Kowalewski, T.; Patterson, G. D.; Matyjaszewski, K. *Macromolecules* **2003**, *36* (14), 5094–5104.

(18) Zhao, Y.; Perrier, S. *Macromolecules* **2007**, *40* (25), 9116–9124.

APPENDIX B. GPC MANUAL AND INSTRUCTIONS

A. Quick Start Instructions

1. Open OmniSec software on desktop

A screen similar to Figure B- 1 will appear. System operational status will be shown in the black box that indicates idle or flow rate of sample.

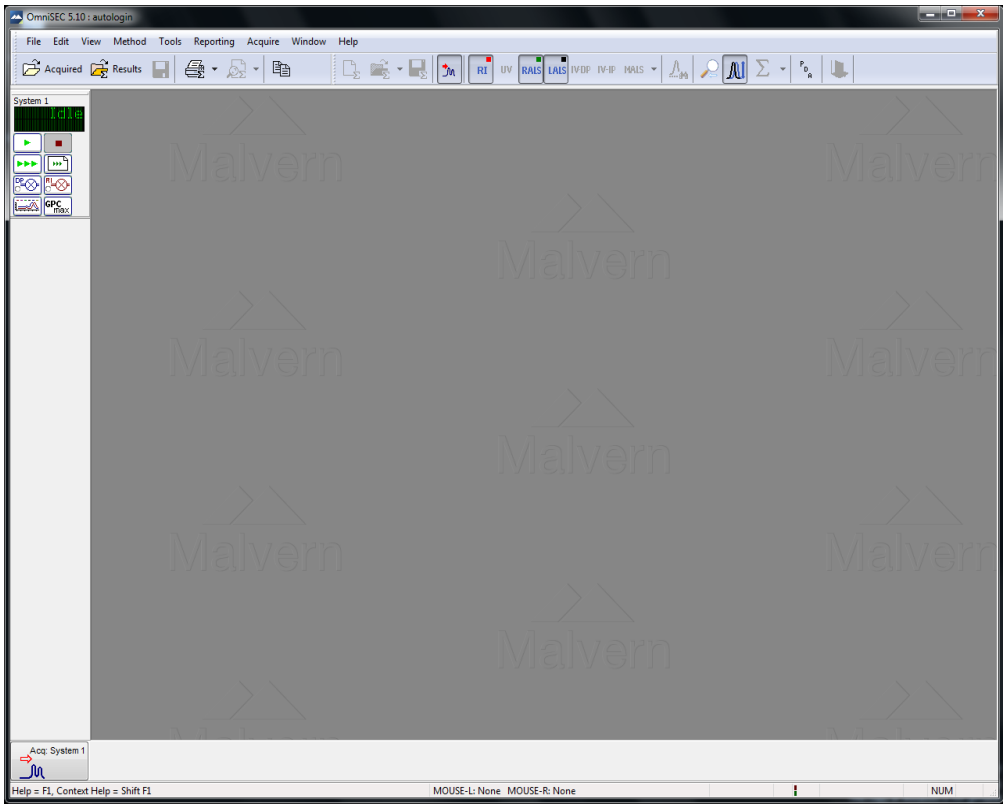

Figure B- 1 OmniSec software start-up

2. Click on the GPCmax button on the left side

This opens up the instruments tool pad. The user can turn the pump on/off, reset the auto sampler, wash the injection needle, and change flow rates.

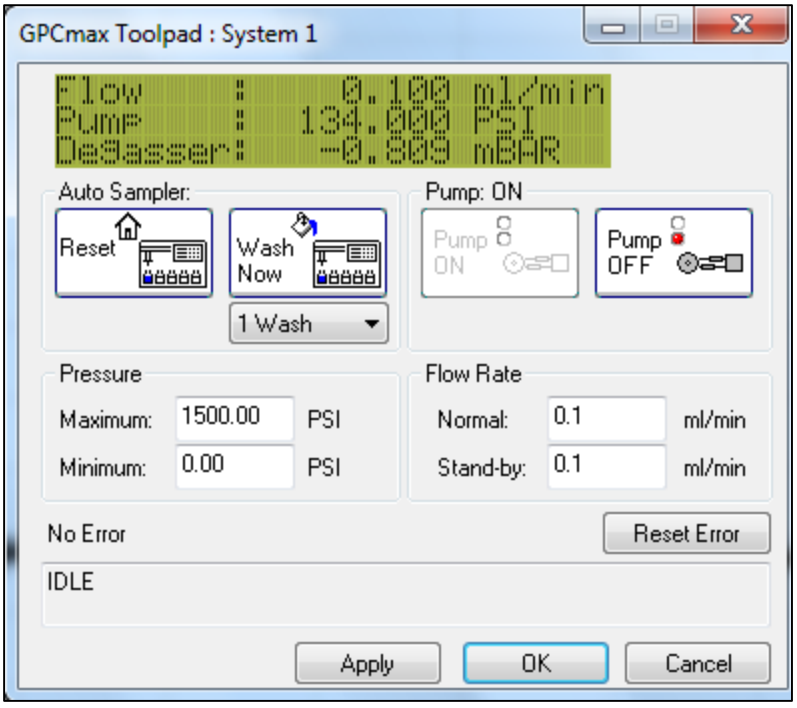

Figure B- 2 GPCmax Menu for pump and flow control

3. Before turning the pump on, set the normal flow rate to be equal to the stand-by flow rate (0.1 mL/min). Hit apply to apply the flow rate when the pump is turned on.

4. Turn the pump on by clicking the Pump ON button. You will see the flow increase to the desired flow rate as well as the pump pressure increase. The normal pressure should be around 60 PSI for the A6000M column alone and 100 PSI when in series with the A2000 column. Deviations of slight amounts (+30-40 PSI) could be from no zero pressure readings at no flow. This is not a big concern, but can be reset in a technician visit. Large deviations (50+ PSI) indicates the light scattering filters are clogged and need to be changed.

5. Increase flow rate. The internal controls have been set to steadily increase to set flow rate, but good practice should be to increase in small (0.2 mL/min) increments. Move the flow rate up in small steps as the pressure evens off at each flow rate. Flow rate should

not be above 1.0 mL/min. For our set up with 2 columns, the flow rate should be set to 0.7 mL/min.

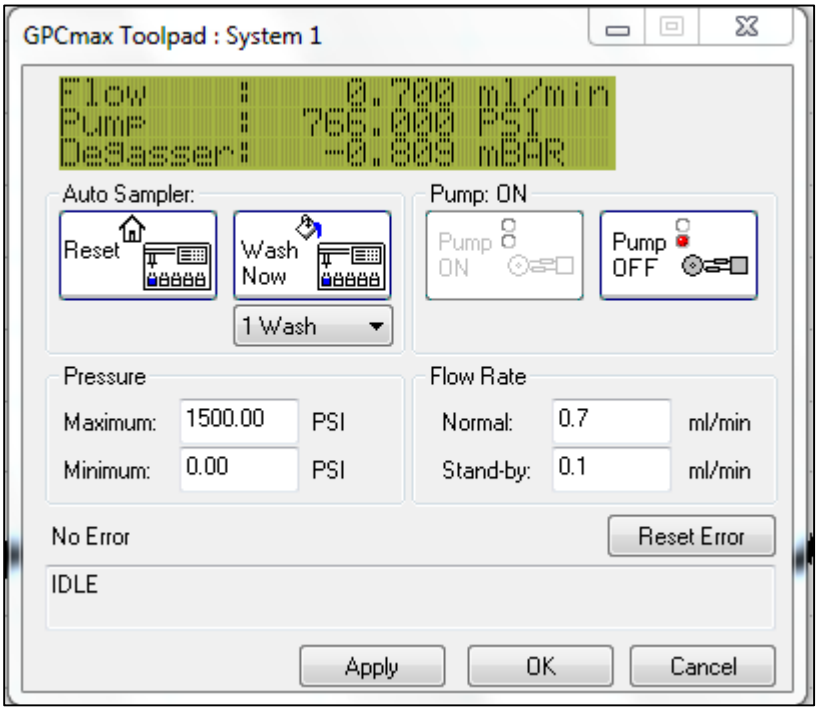

Figure B- 3 GPCmax menu for 0.7 mL/min flow rate

6. Setting up a system purge.

Purging of the detectors allows for stabilizing the baseline readings. Our system only purges the refractive index (RI) detector. Other systems with a viscometer would need to purge that detector as well. On the RI detector, press the purge button. A red light will indicate that purge is on as shown in Figure B- 4.

Figure B- 4 Image of RI detector in purge mode

7. Open the quick run menu.

Referring back to Figure B- 1, select the one play button (little picture) here to bring up the menu for a single sample. Figure B- 5shows the menu options for quick run. It is good practice to purge once a day and before the first sample runs. Saving data is not necessary for typical purging protocols, but can save them to send them to technical support.

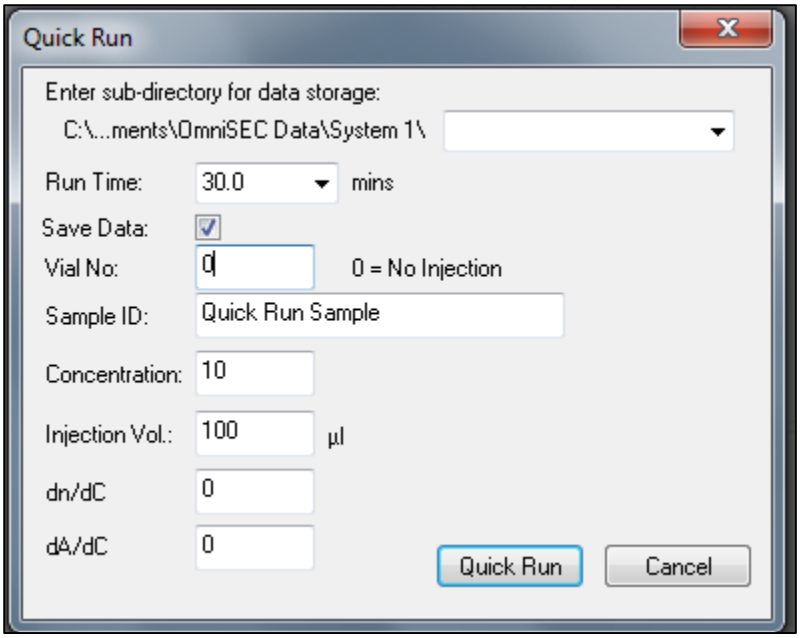

Figure B- 5 Sample quick run menu for single injections and baselines

Figure B- 6 is a typical baseline data collected during purge. This purge time was for 60 minutes. Right angle light scattering (green) and low angle light scattering (black) have very stable baselines. This basically means the light scattering filter is in good working order. The RI (red) line exhibits some noise early on, but evens out over time. This is typical. If purge baselines are very noise, continue the purge for longer and then change filters.

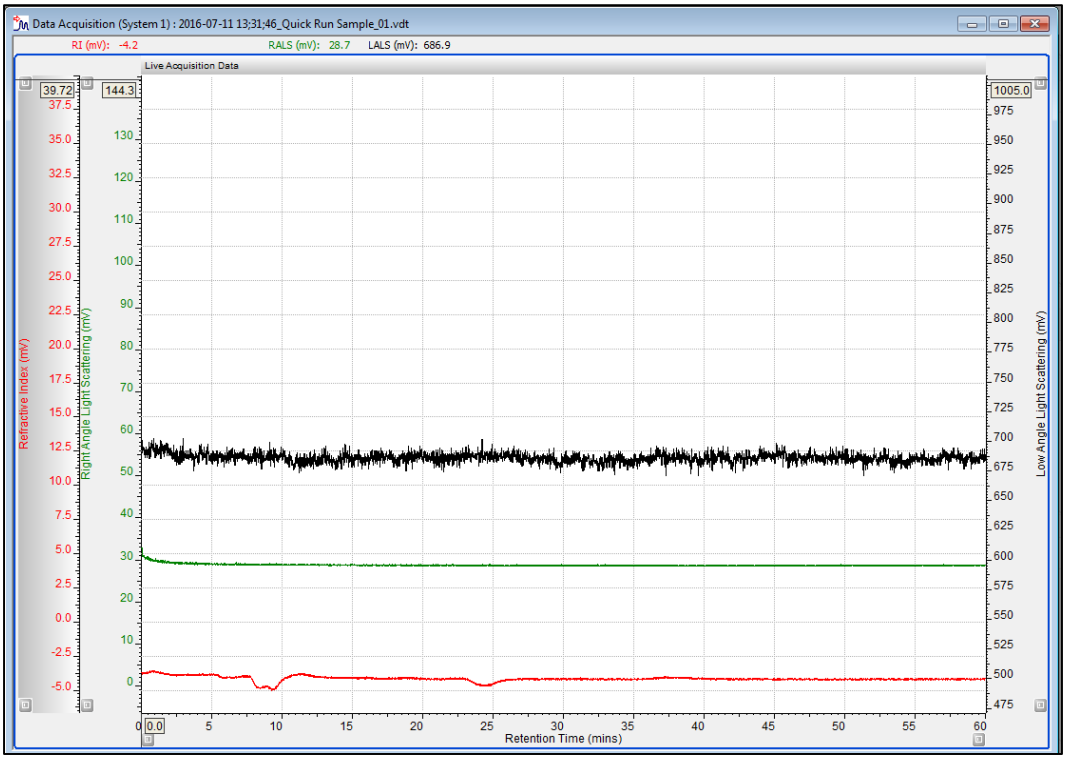

Figure B- 6 Image of typical baselines for all detectors

B. Running a sample

Similar to step 7 in part A, open the quick run menu. This menu allows for a single run to be set up to run. Before completing this step, remember to turn the purge button off on the RI detector. On this menu, you can name the sample and save to specific place. To run a sample, you must have the vial in a numbered place, the concentration (typically 1-5 mg/mL), and the dn/dc (simple search of polymer values). Injection volume should stay at 100 µL. After input values, you can hit 'quick run.' The collection window will appear and real time collection of data will start.

C. Running multiple samples

A sample queue can be created based on the autosampler functionality. This menu can be opened by click on the three arrow menu. Figure B- 7 is the sequence menu that

appears. First, place all vials in consecutive positions in the autosampler. Second, name them in the menu and note all needed values such as concentration, dn/dc. There is no need to change injection volume. Typically, 1 injection is enough to get data on a sample, but multiple injections can help understand if the data is noisy. To set vial numbers, click on pre-injection commands dropdown. In this dropdown, there are options to purge the detectors, etc, but click on vial no. start. Also, click on auto vial at the top of the menu to keep the vial numbers consecutive. The post-run commands dropdown menu has the ability to put in delays between runs or have another term of purging.

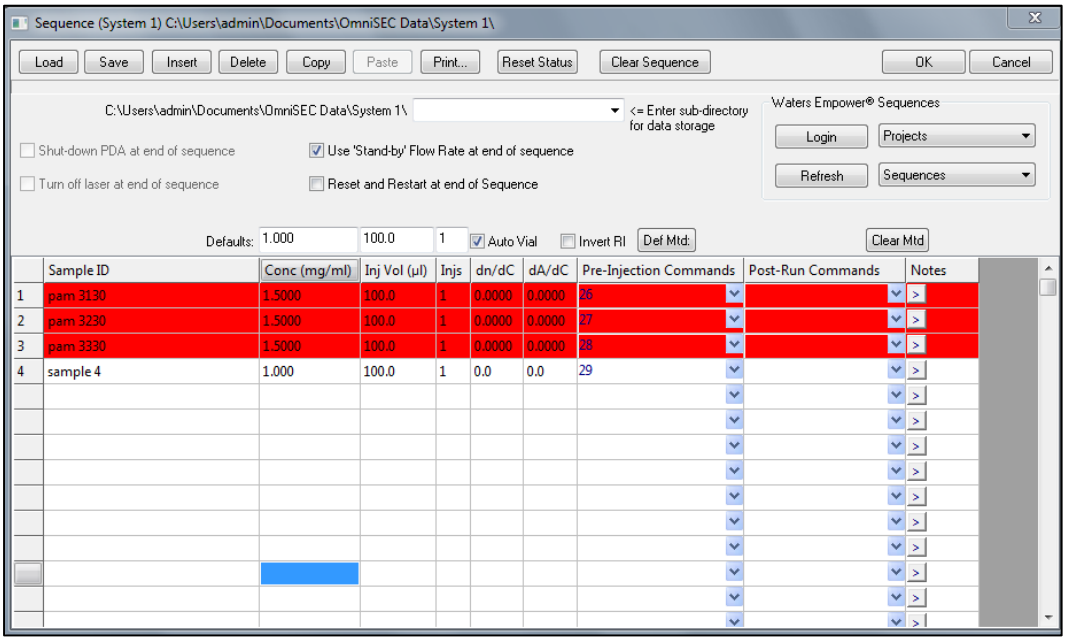

Figure B- 7 Sample sequence menu for multiple samples

C. Sample Preparations

Concentration is important for GPC analysis and must be known. Decide the measured concentration based on the likely size of the polymer. For small polymers, larger concentrations will be needed (5-10 mg/mL), but for large polymers, the solutions need to be dilute (~1mg/ml). Measure polymer into a scintillation vial and then add aqueous mobile

phase from the instrument feed. Typically, measure out 5-10 mL of solution. Stir solution to dissolve all solids. Fill a syringe with the polymer solution and use a filter (0.2 μm) to transfer to GPC sample vials.

D. Extended Period Shutdown

Extra care must be taken when shutting the GPC down before week long breaks. About 3 days before shutdown, use this procedure to start cleaning the system to ensure no biological fouling will occur while the instrument is off. First, make a fresh solution of 0.02 wt. % sodium azide in DI water and flow through the system and columns. The columns can now be removed, capped, and stored away. The sodium azide that is left in the columns works as a bactericide to protect from fouling. Second, connect the flow path with a straight union and start to flow 10 vol. % methanol in DI water solution to clean any precipitate salts. Third, use a 10 vol % acetone in DI water to flow through the system. Finally, the flow can be stopped and the instrument can now be turned off.

When it is time to turn the instrument back on, repeat the above procedure in the opposite order starting with the acetone solution and working toward the sodium azide solution. Between each solution run, the light scattering filter should be changed to avoid buildup of any blockages. The columns can be attached and the sodium azide solution should be flowed through while purging to monitor baselines during the start up. Once the baselines have equilibrated, the solution can be transferred to the normal sodium sulfate solution for normal operation.

VITA

Travis Thornell was born and raised in Vicksburg, MS. He graduated with his bachelors of science degree with highest honors in Polymer Science from the University of Southern Mississippi (USM). While attending USM, he was an undergraduate researcher in Prof. Jeffrey Wiggins' research group assisting in the development of epoxy nanocomposite thermoset networks. In the fall of 2013, he started at the School of Materials Engineering at Purdue University for his PhD studies. With his research interests in polymer physics and rheology, he joined Prof. Kendra Erk's Soft Material Mechanics research group. His research has allowed him to gain experience and expertise in a variety of synthesis and characterization methods.